# EXCEEDING CONVENTIONAL PHOTOVOLTAIC EFFICIENCY LIMITS USING COLLOIDAL QUANTUM DOTS

by

GREGORY F. PACH

A thesis submitted to the
Faculty of the Graduate School of the
University of Colorado in partial fulfillment
of the requirement for the degree of
Master of Science
Department of Electrical, Computer, and Energy Engineering
2017

This thesis entitled:
Exceeding Conventional Photovoltaic Efficiency Limits Using Colloidal Quantum Dots
written by Gregory F. Pach
has been approved for the Department of Electrical, Computer, and Energy Engineering

_____
Sean E. Shaheen Ph.D.

_____
Joseph M. Luther Ph.D.

Date_____

The final copy of this thesis has been examined by the signatories, and we find that both the content and the form meet acceptable presentation standards of scholarly work in the above mentioned discipline.

Pach, Gregory F. (M.S. Electrical Engineering)
Exceeding Conventional Photovoltaic Efficiency Limits Using Colloidal Quantum Dots
Thesis directed by Associate Professor Sean E. Shaheen

Colloidal quantum dots (QDs) are a widely investigated field of research due to their highly tunable nature in which the optical and electronic properties of the nanocrystal can be manipulated by merely changing the nanocrystal's size. Specifically, colloidal quantum dot solar cells (QDSCs) have become a promising candidate for future generation photovoltaic technology. Quantum dots exhibit multiple exciton generation (MEG) in which multiple electron-hole pairs are generated from a single high-energy photon. This process is not observed in bulk-like semiconductors and allows for QDSCs to achieve theoretical efficiency limits above the standard single-junction Shockley-Queisser limit. However, the fast expanding field of QDSC research has lacked standardization of synthetic techniques and device design. Therefore, we sought to detail methodology for synthesizing PbS and PbSe QDs as well as photovoltaic device fabrication techniques as a fast track toward constructing high-performance solar cells. We show that these protocols lead toward consistently achieving efficiencies above 8% for PbS QDSCs.

Using the same methodology for building single-junction photovoltaic devices, we incorporated PbS QDs as a bottom cell into a monolithic tandem architecture along with solution-processed CdTe nanocrystals. Modeling shows that near-peak tandem device efficiencies can be achieved across a wide range of bottom cell band gaps, and therefore the highly tunable band gap of lead-chalcogenide QDs lends well towards a bottom cell in a tandem architecture. A fully functioning monolithic tandem device is realized through the development of a ZnTe/ZnO recombination layer that appropriately combines the two subcells in series.

Multiple recent reports have shown nanocrystalline heterostructures to undergo the MEG process more efficiency than several other nanostrucutres, namely lead-chalcogenide QDs. The final section of my thesis expands upon a recent publication by Zhang *et. al*., which details the synthesis of PbS/CdS heterostructures in which the PbS and CdS domains exist on opposite sides of the nanocrystal and are termed "Janus particles". Transient absorption spectroscopy shows MEG quantum yields above unity very the thermodynamic limit of $2E_g$ for PbS/CdS Janus particles. We further explain a mechanism for enhanced MEG using photoluminescence studies.

ACKNOWLEDGEMENTS

I would like to thank all the advisors I've had at NREL and CU who have helped guide me over the past two years. I've had amazing support since first arriving at NREL as intern, which has made my path through graduate school an incredible experience. First and foremost, thank you to Joey Luther and Matt Beard for always having time to talk about my projects and everything you two have done to help me. Additionally, thank you to Sean Shaheen for your help at CU and to everyone else at CU and NREL who helped in my success.

Thank you to all the post-docs and fellow grad students at NREL that made working in lab so enjoyable. Ryan, thank you for guiding me when I first arrived in the group and for leaving behind so many unfinished projects. Ashley and Dan, thank you for being my chemistry gurus. Erin, I could always count on you as a late night lab partner. Jeff, it's been an honor to share such an admiration for all of Teddy's work. Nick and Lance, thank you for always making sure the lab got the appropriate rest it deserved.

Thank you to my roommates—J-Dawg, K-Bone, Big D, Fernie, and Rizzle. You guys often made studying at home impossible but always provided a release when I was feeling stressed out.

And finally to my family, thank you for all your support through my life. Without you, none of this would have ever been possible.

CONTENTS

LIST OF FIGURES

CHAPTER I

# Introduction

## 1.1 Background

Quantum-confined, semiconducting, quasi-spherical nanocrystals, called "quantum dots", have become a widespread field of research in recent years due to their easily tunable optical and electronic properties, which can be altered by merely changing the size of the nanocrystal. Quantum dots (QDs) have been made from a variety of materials—most commonly II-VI, III-V, and IV-VI semiconductors—and used for diverse applications including biosensors[1], photodetectors[2], LEDs[3], and photovoltaics[4]. This thesis will primarily focus on metal chalcogenide nanocrystals, specifically PbE and CdE (where E = S, Se, or Te), for photovoltaic (PV) applications. Colloidal quantum dot solar cells (QDSCs) offer several advantages over conventional silicon solar panels. Largely due to direct band gaps, QDs have much higher absorption coefficients allowing for thinner active absorber layers. Additionally, the surface chemistry of QDs can be modified to permit colloidal stability in a variety of solvents allowing for solution-processed deposition techniques that can simultaneously increase throughput and lower the production cost of photovoltaic systems. Perhaps most importantly, QDs can exhibit multiple exciton generation (MEG) in which multiple excitons are created from a single high-energy photon, a process not observed in bulk semiconductors. MEG could allow for QDSCs to achieve efficiencies above the standard Shockley-Queisser limit for a single-junction device.[5]

## 1.2 Formation and Carrier Dynamics of Close-Packed Quantum Dot Arrays

QDs are most commonly fabricated using hot injection synthetic techniques in which a variety of properties, including the size of the nanocrystal, can be controlled through the reaction precursors and conditions.[6-10] Because of the high surface-to-volume ratio of QDs, the surface chemistry largely dictates the optical and electronic properties of nanocrystal. In order to have control over these properties, QD syntheses bind ligands to the nanocrystal surface. The ligand coverage of the QD determines the colloidal stability, helps passivate dangling bonds that function as trap states on under-coordinated QD surfaces, and acts as a dopant to control the QD work function and relative band positioning.[11]

Colloidal QD solutions can be cast into close-packed films using techniques such as spincoating, dipcoating, dropcasting, bladecoating, and more. Carrier transport within close-packed QD films occurs through a several different mechanisms including hopping, tunneling, Förster resonance energy transfer (FRET), and more.[12-13] To produce highly conductive films, the coupling between QDs should be maximized. The coupling energy, β, is expressed as $\beta = h\Gamma$, where $h$ is Planck's constant and Γ is the tunneling rate given by

$$\Gamma \sim \exp\left\{-\left(\frac{2m^{*}\Delta E}{\hbar^{2}}\right)^{1/2}\Delta x\right\}$$

where $m^{*}$ is the carrier effective mass, ħ is Planck's constant divided by 2π, and ΔE and $\Delta x$ are the height and width of the tunneling barrier, respectively. The characteristics of the tunneling barrier can be directly controlled by the ligand on the QD surface. Presently, the most refined syntheses of colloidal PbE and CdE (E = S, Se, Te) QDs involve the use of long-chain, organic ligands.[8] Therefore, in order to increase the coupling within close-packed arrays, the native ligands are often replaced with shorter, more conductive ligands (i.e. $CdCl_2$, $PbI_2$, 1,2-

ethanedithiol, tetrabutylammonium iodide, and more) that can facilitate band-like transport by lowering the height and width of the energy barrier (Figure 1.1).[14-16]

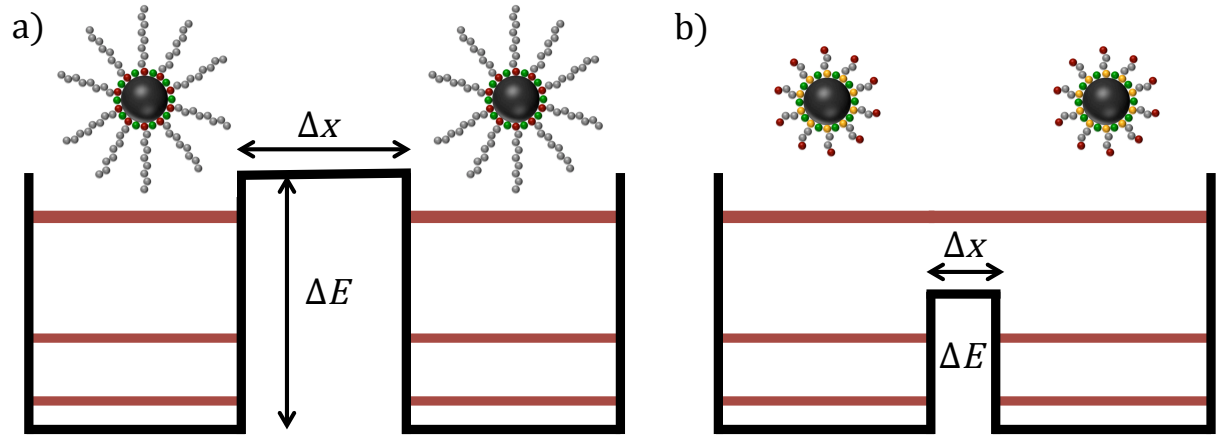


**Figure 1.1.** Schematic representation of energy states (red lines) inside quantum wells corresponding to individual QDs. The height and width of the barrier between wells is determined by the ligand capping on the QD surface. a) Native, aliphatic ligands create a large energy barrier between quantum wells. b) After native ligands are replaced with short, inorganic ligands, the height and width of the barrier decreases.

The ligand exchange process can be completed either while QDs remain in solution, called solution-phase exchange, or after films have been cast, known as solid-state exchange. In the latter case, films are usually formed in a layer-by-layer fashion, with the ligand exchange occurring after each successive layer deposition in order to ensure complete exchange. This has been the most widely used method of constructing QD PV devices[14, 17-18], however, this method results in highly disordered QD arrays due to the space exposed within the film from the removed ligands. For this reason, solution-phase ligand exchange is more favorable for casting uniform and ordered QD arrays. Recently, the field has begun to shift toward developing high-density, pre-exchanged quantum dot inks that can be deposited to form QD films in a single step.[19-22]

### 1.3 Quantum Dot Photovoltaic Device Architecture

Presently the top-performing QDSC architectures are based on the planar heterojunction model.[18, 20] This architecture uses selective contacts to extract opposite charges from separate sides of the PV device.[23] A glass substrate coated with a transparent conducting oxide (TCO), most commonly fluorine-doped or indium-doped tin oxide (FTO and ITO, respectively), is used as the foundation of the device. Highly n-type, wide band gap metal oxide layers such as $TiO_2$, ZnO, and $SnO_2$ are deposited next and used as an electron transport layer (ETL). The active QD layer is then deposited which can be cast in a layer-by-layer fashion or in a single step from pre-exchanged solutions as mentioned above. The junction between a highly n-type electrode and less n-type or p-type QDs will create a depletion region extending into the QD layer promoting drift-like charge extraction. To further enhance drift transport mechanisms, two different ligand treatments are often used in the active layer to produce QDs with different work functions. This creates band bending within the active layer at the interface of the QD treatments and helps block charges from reaching the opposite electrode. QDSCs are still primarily dominated by diffusion-controlled charge transport and therefore active layers are limited by the diffusion length to a couple hundred nanometers in top-performing devices.[24] Finally to complete the device, a reflective, deep work function back electrode is deposited (commonly Au or $MoO_x$/Al) as a hole contact, or hole transport layer (HTL). Figure 1.2 shows a schematic of a conventional planar heterojunction QDSC as well as a band diagram for a similar device. Chapter II of this thesis will cover QD synthetic procedures and QDSC fabrication techniques, specifically using PbS and PbSe QDs.

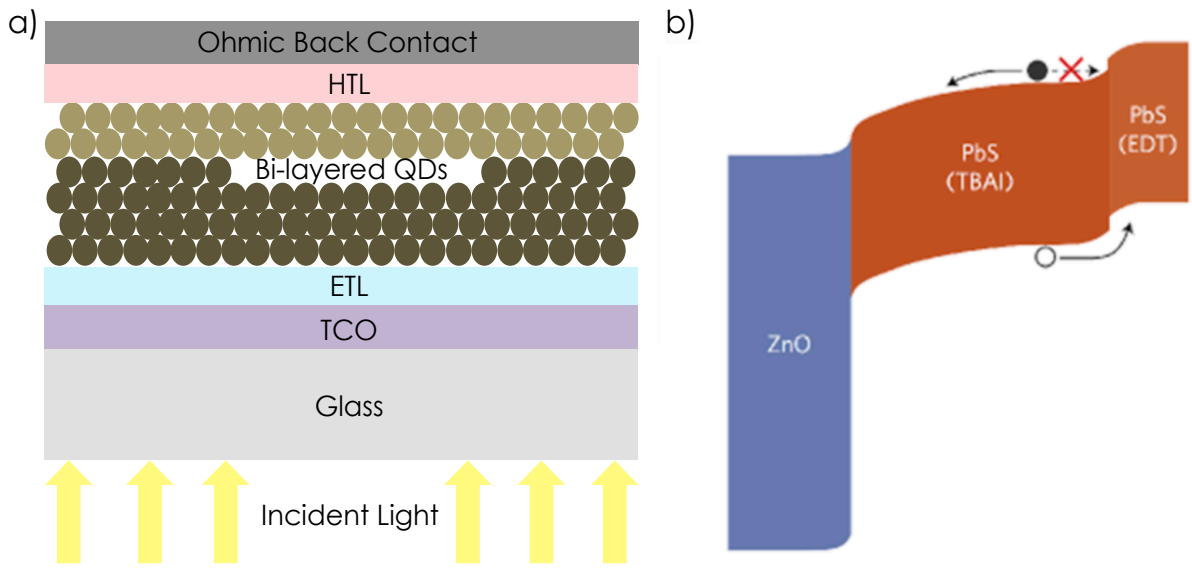


**Figure 1.2.** a) Schematic representation of conventional quantum dot solar cell architecture. b) Band representation of a PV device similar to that shown in (a) (Reprinted with permission from Carey *et. al.*)[23]

### 1.4 Breaking The Shockley-Queisser Single-Junction Limit

Conventional silicon solar cells are beginning to approach the theoretical thermodynamic efficiency limit with recent certified efficiencies of 26.6%[25] and therefore prompting research surrounding future PV technology to focus on methods of breaking the single-junction SQ limit. Perhaps the most investigated method of increasing efficiency limitations has been through development of multi-junction solar cells. The most significant loss mechanism in single-junctions PV devices is through thermalization of excited carriers as they relax the band edge, which multi-junction solar cells attempt to minimize by connecting multiple active layers with different band gaps in series. In multi-junction solar cells light is first incident on the highest band gap material allowing for more efficient collection of high-energy photons. Connecting the subcells in series allows for voltage addition between active layers and a high voltage output. Many studies have begun to explore combining solution-processable materials, such as QDs and perovskite-structured materials, with commercial-ready PV techonology, namely silicon and

CdTe, in multi-junction architectures.[26-28] Chapter III of this thesis will discuss fabrication of solar cells using PbS QDs combined with solution-processed CdTe nanocrystals.

Fabrication of high efficiency monolithic multi-junction solar cells involves the appropriate band alignment of the individual subcells for maximum voltage output. This is done using interstitial layers that combine opposite charge carriers between active layers, which are referred to as recombination or tunnel junction layers.[29] The appropriate recombination layer aligns the electron and hole quasi-Fermi levels between subcells such that the voltages add without loss (Figure 1.3). An ideal two-junction solar cell, often called a tandem solar cell, can theoretically achieve an efficiency of 45% using a band gap pairing of 1.0 and 1.9 eV with infinitely thick layers.[30-31] However, an analysis shown in Chapter III demonstrates that near-peak tandem device efficiencies can be achieved across a range of band gap pairings by modulating the top cell thickness.[26]

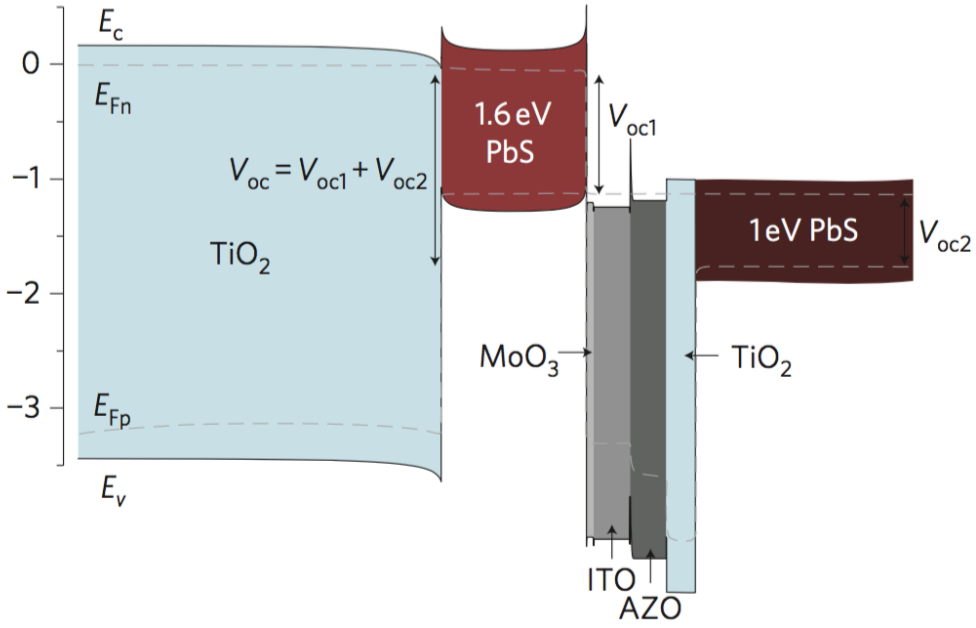


**Figure 1.3.** Schematic representation of a PbS/PbS tandem solar cell at open-circuit voltage. A recombination layer of $MoO_3$, ITO, aluminum zinc oxide (AZO), and $TiO_2$ is used to align the quasi-Fermi levels and facilitate voltage addition. (Reprinted with permission from Wang *et al.*)[29]

In addition to multi-junction solar cells, more exotic techniques have been employed to overcome the SQ limit. As previously mentioned, QDs exhibit MEG, which can lead to higher solar cell efficiencies. The MEG process occurs when a hot exciton relaxes to the band edge and transfers its energy into the generation of another electron-hole pair. MEG studies have been carried out on a variety of materials[32-34] and MEG has also been observed in operating QDSCs.[35] However, the majority of these studies reveal MEG quantum yields (defined as the ratio of the number of excitons produced to the number of incident photons) above unity only at energies above the theoretical MEG threshold of $2E_g$.[34]

Heterostrucuted nanocrystals have recently shown promise for enhanced MEG with MEG quantum yields exceeding unity very near the thermodynamic limit.[36] Core/shell QD architectures have widely been used to produce highly efficient luminescent devices in which the relative band alignment between the core and shell of the nanocrystal can be used to spatially confine photogenerated carriers and increase radiative recombination. Recently however, studies have shown that the relative band positions of the heterostructure can be used to control the hot carrier cooling dynamics and provide a mechanism for enhanced MEG.[36-37] Chapter IV of this thesis expands upon the development of PbS/CdS heterostructures in which the PbS and CdS domains are on separate sides of the nanocrystal—so-called Janus particles.[38] Transient absorption spectroscopy reveals MEG quantum yields above unity very near $2E_g$ in PbS/CdS Janus-like heterostructures and photoluminescence studies help reveal the relative band alignment between the two domains.

## 1.5 References


1. Bruchez, M.; Moronne, M.; Gin, P.; Weiss, S.; Alivisatos, A. P., Semiconductor Nanocrystals as Fluorescent Biological Labels. *Science* **1998,** *281* (5385), 2013.

2. Konstantatos, G.; Howard, I.; Fischer, A.; Hoogland, S.; Clifford, J.; Klem, E.; Levina, L.; Sargent, E. H., Ultrasensitive solution-cast quantum dot photodetectors. *Nature* **2006,** *442* (7099), 180-183.

3. Qian, L.; Zheng, Y.; Xue, J.; Holloway, P. H., Stable and efficient quantum-dot light-emitting diodes based on solution-processed multilayer structures. *Nat Photon* **2011,** *5* (9), 543-548.

4. Nozik, A. J., Quantum dot solar cells. *Physica E: Low-dimensional Systems and Nanostructures* **2002,** *14* (1–2), 115-120.

5. Hanna, M.; Nozik, A., Solar conversion efficiency of photovoltaic and photoelectrolysis cells with carrier multiplication absorbers. *Journal of Applied Physics* **2006,** *100* (7), 074510.

6. Zhang, J.; Gao, J.; Church, C. P.; Miller, E. M.; Luther, J. M.; Klimov, V. I.; Beard, M. C., PbSe Quantum Dot Solar Cells with More than 6% Efficiency Fabricated in Ambient Atmosphere. *Nano Letters* **2014**.

7. Zhang, J.; Gao, J.; Miller, E. M.; Luther, J. M.; Beard, M. C., Diffusion-Controlled Synthesis of PbS and PbSe Quantum Dots with in Situ Halide Passivation for Quantum Dot Solar Cells. *ACS Nano* **2013,** *8* (1), 614-622.

8. Hines, M. A.; Scholes, G. D., Colloidal PbS Nanocrystals with Size-Tunable Near-Infrared Emission: Observation of Post-Synthesis Self-Narrowing of the Particle Size Distribution. *Advanced Materials* **2003,** *15* (21), 1844-1849.

9. Weidman, M. C.; Beck, M. E.; Hoffman, R. S.; Prins, F.; Tisdale, W. A., Monodisperse, Air-Stable PbS Nanocrystals via Precursor Stoichiometry Control. *ACS Nano* **2014,** *8* (6), 6363-6371.

10. Hendricks, M. P.; Campos, M. P.; Cleveland, G. T.; Jen-La Plante, I.; Owen, J. S., A tunable library of substituted thiourea precursors to metal sulfide nanocrystals. *Science* **2015,** *348* (6240), 1226.

11. Anderson, N. C.; Hendricks, M. P.; Choi, J. J.; Owen, J. S., Ligand Exchange and the Stoichiometry of Metal Chalcogenide Nanocrystals: Spectroscopic Observation of Facile Metal-Carboxylate Displacement and Binding. *Journal of the American Chemical Society 135* (49), 18536-18548.

12. Kagan, C. R.; Murray, C. B.; Nirmal, M.; Bawendi, M. G., Electronic Energy Transfer in CdSe Quantum Dot Solids. *Physical Review Letters* **1996,** *76* (9), 1517-1520.

13. Talapin, D. V.; Lee, J.-S.; Kovalenko, M. V.; Shevchenko, E. V., Prospects of Colloidal Nanocrystals for Electronic and Optoelectronic Applications. *Chemical Reviews* **2010,** *110* (1), 389-458.

14. Crisp, R. W.; Kroupa, D. M.; Marshall, A. R.; Miller, E. M.; Zhang, J.; Beard, M. C.; Luther, J. M., Metal Halide Solid-State SurfaceTreatment for High Efficiency PbS and PbSe QD Solar Cells. *Scientific Reports* **2015,** *5*.

15. Marshall, A. R.; Young, M. R.; Nozik, A. J.; Beard, M. C.; Luther, J. M., Exploration of Metal Chloride Uptake for Improved Performance Characteristics of PbSe Quantum Dot Solar Cells. *The Journal of Physical Chemistry Letters* **2015,** *6* (15), 2892-2899.

16. Liu, M.; de Arquer, F. P. G.; Li, Y.; Lan, X.; Kim, G.-H.; Voznyy, O.; Jagadamma, L. K.; Abbas, A. S.; Hoogland, S.; Lu, Z.; Kim, J. Y.; Amassian, A.; Sargent, E. H., Double-Sided Junctions Enable High-Performance Colloidal-Quantum-Dot Photovoltaics. *Advanced Materials* **2016,** *28* (21), 4142-4148.

17. Lan, X.; Voznyy, O.; García de Arquer, F. P.; Liu, M.; Xu, J.; Proppe, A. H.; Walters, G.; Fan, F.; Tan, H.; Liu, M.; Yang, Z.; Hoogland, S.; Sargent, E. H., 10.6% Certified Colloidal Quantum Dot Solar Cells via Solvent-Polarity-Engineered Halide Passivation. *Nano Letters* **2016,** *16* (7), 4630-4634.

18. Swarnkar, A.; Marshall, A. R.; Sanehira, E. M.; Chernomordik, B. D.; Moore, D. T.; Christians, J. A.; Chakrabarti, T.; Luther, J. M., Quantum dot–induced phase stabilization of α-CsPbI3 perovskite for high-efficiency photovoltaics. *Science* **2016,** *354* (6308), 92.

19. Kim, S.; Noh, J.; Choi, H.; Ha, H.; Song, J. H.; Shim, H. C.; Jang, J.; Beard, M. C.; Jeong, S., One-Step Deposition of Photovoltaic Layers Using Iodide Terminated PbS Quantum Dots. *The Journal of Physical Chemistry Letters* **2014,** *5* (22), 4002-4007.

20. Liu, M.; Voznyy, O.; Sabatini, R.; Garcia de Arquer, F. P.; Munir, R.; Balawi, A. H.; Lan, X.; Fan, F.; Walters, G.; Kirmani, A. R.; Hoogland, S.; Laquai, F.; Amassian, A.; Sargent, E. H., Hybrid organic-inorganic inks flatten the energy landscape in colloidal quantum dot solids. *Nat Mater* **2017,** *16* (2), 258-263.

21. Ning, Z.; Dong, H.; Zhang, Q.; Voznyy, O.; Sargent, E. H., Solar Cells Based on Inks of n-Type Colloidal Quantum Dots. *ACS Nano* **2014**.

22. Aqoma, H.; Al Mubarok, M.; Hadmojo, W. T.; Lee, E.-H.; Kim, T.-W.; Ahn, T. K.; Oh, S.-H.; Jang, S.-Y., High-Efficiency Photovoltaic Devices using Trap-Controlled Quantum-Dot Ink prepared via Phase-Transfer Exchange. *Advanced Materials* **2017**, 1605756-n/a.

23. Carey, G. H.; Abdelhady, A. L.; Ning, Z.; Thon, S. M.; Bakr, O. M.; Sargent, E. H., Colloidal Quantum Dot Solar Cells. *Chemical Reviews* **2015,** *115* (23), 12732-12763.

24. Carey, G. H.; Levina, L.; Comin, R.; Voznyy, O.; Sargent, E. H., Record Charge Carrier Diffusion Length in Colloidal Quantum Dot Solids via Mutual Dot-To-Dot Surface Passivation. *Advanced Materials* **2015,** *27* (21), 3325-3330.

25. Yoshikawa, K.; Kawasaki, H.; Yoshida, W.; Irie, T.; Konishi, K.; Nakano, K.; Uto, T.; Adachi, D.; Kanematsu, M.; Uzu, H.; Yamamoto, K., Silicon heterojunction solar cell with interdigitated back contacts for a photoconversion efficiency over 26%. *Nature Energy* **2017,** *2*, 17032.

26. Crisp, R. W.; Pach, G. F.; Kurley, J. M.; France, R. M.; Reese, M. O.; Nanayakkara, S. U.; MacLeod, B. A.; Talapin, D. V.; Beard, M. C.; Luther, J. M., Tandem Solar Cells from Solution-Processed CdTe and PbS Quantum Dots Using a ZnTe–ZnO Tunnel Junction. *Nano Letters* **2017**.

27. Rühle, S., The detailed balance limit of perovskite/silicon and perovskite/CdTe tandem solar cells. *physica status solidi (a)* **2017**, 1600955-n/a.

28. Bush, K. A.; Palmstrom, A. F.; Yu, Z. J.; Boccard, M.; Cheacharoen, R.; Mailoa, J. P.; McMeekin, D. P.; Hoye, R. L. Z.; Bailie, C. D.; Leijtens, T.; Peters, I. M.; Minichetti, M. C.; Rolston, N.; Prasanna, R.; Sofia, S.; Harwood, D.; Ma, W.; Moghadam, F.; Snaith, H. J.; Buonassisi, T.; Holman, Z. C.; Bent, S. F.; McGehee, M. D., 23.6%-efficient monolithic perovskite/silicon tandem solar cells with improved stability. *Nature Energy* **2017,** *2*, 17009.

29. Wang, X.; Koleilat, G. I.; Tang, J.; Liu, H.; Kramer, I. J.; Debnath, R.; Brzozowski, L.; Barkhouse, D. A. R.; Levina, L.; Hoogland, S.; Sargent, E. H., Tandem colloidal quantum dot solar cells employing a graded recombination layer. *Nat Photon* **2011,** *5* (8), 480-484.

30. Vos, A. D., Detailed Balance Limit of the Efficiency of Tandem Solar Cells. *J. Phys. D: Appl. Phys.* **1980,** *13* (5), 839-46.

31. Kurtz, S. R.; Faine, P.; Olson, J., Modeling of two‐junction, series‐connected tandem solar cells using top‐cell thickness as an adjustable parameter. *Journal of Applied Physics* **1990,** *68* (4), 1890-1895.

32. Gabor, N. M.; Zhong, Z.; Bosnick, K.; Park, J.; McEuen, P. L., Extremely Efficient Multiple Electron-Hole Pair Generation in Carbon Nanotube Photodiodes. *Science* **2009,** *325* (5946), 1367.

33. Luther, J. M.; Beard, M. C.; Song, Q.; Law, M.; Ellingson, R. J.; Nozik, A. J., Multiple Exciton Generation in Films of Electronically Coupled PbSe Quantum Dots. *Nano Letters* **2007,** *7* (6), 1779-1784.

34. Midgett, A. G.; Luther, J. M.; Stewart, J. T.; Smith, D. K.; Padilha, L. A.; Klimov, V. I.; Nozik, A. J.; Beard, M. C., Size and Composition Dependent Multiple Exciton Generation Efficiency in PbS, PbSe, and PbSxSe1–x Alloyed Quantum Dots. *Nano Letters* **2013,** *13* (7), 3078-3085.

35. Semonin, O. E.; Luther, J. M.; Choi, S.; Chen, H.-Y.; Gao, J.; Nozik, A. J.; Beard, M. C., Peak External Photocurrent Quantum Efficiency Exceeding 100% via MEG in a Quantum Dot Solar Cell. *Science* **2011,** *334* (6062), 1530-1533.

36. Cirloganu, C. M.; Padilha, L. A.; Lin, Q.; Makarov, N. S.; Velizhanin, K. A.; Luo, H.; Robel, I.; Pietryga, J. M.; Klimov, V. I., Enhanced carrier multiplication in engineered quasi-type-II quantum dots. *Nature Communications* **2014,** *5*, 4148.

37. Eshet, H.; Baer, R.; Neuhauser, D.; Rabani, E., Theory of highly efficient multiexciton generation in type-II nanorods. *Nature Communications* **2016,** *7*, 13178.

38. Zhang, J.; Chernomordik, B. D.; Crisp, R. W.; Kroupa, D. M.; Luther, J. M.; Miller, E. M.; Gao, J.; Beard, M. C., Preparation of Cd/Pb Chalcogenide Heterostructured Janus Particles via Controllable Cation Exchange. *ACS Nano* **2015,** *9* (7), 7151-63.

CHAPTER II

# Quantum Dot Solar Cell Fabrication Protocols

Adapted from:

Boris D. Chernomordik, Ashley R. Marshal, Gregory F. Pach, Joseph M. Luther, and Matthew C. Beard., Quantum Dot Solar Cell Fabrication Protocols. *Chemistry of Materials* **29** (1), 189-198 (2017).

## 2.1 Abstract

Colloidally synthesized quantum-confined semiconducting spherical nanocrystals, often referred to as quantum dots (QDs), offer a high degree of chemical, optical, and electronic tunability. As a result, there is an increasing interest in employing colloidal QDs for electronic and optical applications that is reflected in a growing number of publications. In this protocol we provide detailed procedures for the fabrication of QD solar cells specifically employing PbSe and PbS QDs. We include details that are learned through experience, beyond those in typical methodology sections, and include example pictures to aid in fabricating QD solar cells. Although successful solar cell fabrication is ultimately learned through experience, this protocol is intended to accelerate that process. The protocol developed here is intended to be a general starting point for developing PbS and PbSe QD test bed solar cells. We include steps for forming conductive QD films via dip coating as well as spin coating. Finally, we provide protocols that detail the synthesis of PbS and PbSe QDs through a unique cation exchange reaction and discuss how different QD synthetic routes could impact the resulting solar cell performance.

## 2.2 Introduction

Colloidal semiconductor quantum dots (QDs) provide a unique platform for designing a wide array of optoelectronic applications due to quantum confinement and enhanced surface-to-volume ratios. These unique size-dependent properties allow for emergent electrical and optical phenomenon derived from QD-QD, and QD-ligand electronic coupling. Benefits and advantages of QDs include: strong optical transitions (light absorption and emission), a large range of tunable band gap onset energies, control over band edge energies[1] and workfunction[2], facile synthesis, facile incorporation into matrices[3] or deposition as thin films, and desirable excited state properties such as enhanced multiple exciton generation (MEG)[4], long carrier lifetimes[5,6], and charge and energy transfer phenomenon with surface adsorbates[7]. Thus, QDs are being explored and commercialized as active components in displays (computer monitors, televisions, etc.)[8], optical detector applications[9], bioimaging[10], and green energy applications such as photovoltaics[11], thermoelectrics[12], and solid-state lighting[13,14].

Solar cells fabricated from QDs have the potential to exhibit higher power conversion efficiencies through enhanced MEG[15–18], but have not yet reached their full potential. While MEG is enhanced in typical quasi-spherical QDs over bulk and conventional thin film semiconductors, the threshold and efficiency of the MEG process can be improved through shape control[19], internal QD heterojunction interfaces[6], and further material exploration[20]. Research towards increasing the MEG efficiency is an ongoing effort. However, in order to take advantage of these unique properties, researchers must also develop prototype energy conversion architectures that can serve as a test bed for advanced nanoscale phenomena. In solar cells, the active layer typically employs electronically coupled QD arrays[11], however, QD sensitized architectures have shown promise as well[21]. The final solar cell performance will depend upon a

myriad of correlated factors: the QD synthesis, degree of QD-QD and QD-ligand electronic coupling, QD film morphology, QD surface passivation and other defect related carrier recombination centers, and appropriate contact layers. In this protocol, we provide detailed procedures for the fabrication of standard QD solar cells using PbS or PbSe QDs which can achieve 8-9% power conversion efficiency in our laboratory. We also provide a protocol for the synthesis of PbS and PbSe QDs using a cation exchange route from CdS and CdSe QDs[22,23].

### 2.3 Quantum Dot Solar Cell Protocol

#### Reagents

3-mercaptopropionic acid (MPA, >99%), N,N-dimetholformamide (DMF, anhydrous, 99.8%), methanol (reagent grade), 1,2-ethanedithiol (EDT, ≥98%), acetonitrile (99.8%), titanium(IV) ethoxide (≥ 97%), Molybdenum trioxide ($MoO_3$, 99.99%), and hydrochloric acid (ACS reagent, 37%) are purchased from Sigma Aldrich-USA and used as received. Lead(II) iodide ($PbI_2$, 99.9985%) is purchased from Alfa Aesar.

#### Substrates

Polished float glass substrates (25 mm x 25 mm x 1.1 mm) with pre-patterned FTO or ITO on one side are purchased from Thin Film Devices (Figure 2.1b). The FTO (product #650) is nominally 200 ± 20 nm in thickness, although we have measured it to be ~400 nm, with a 20 ± 5 Ω/□ sheet resistance. The ITO (product #550) is nominally 150 ± 10 nm thick with a 20 ± 5 Ω/□ sheet resistance.

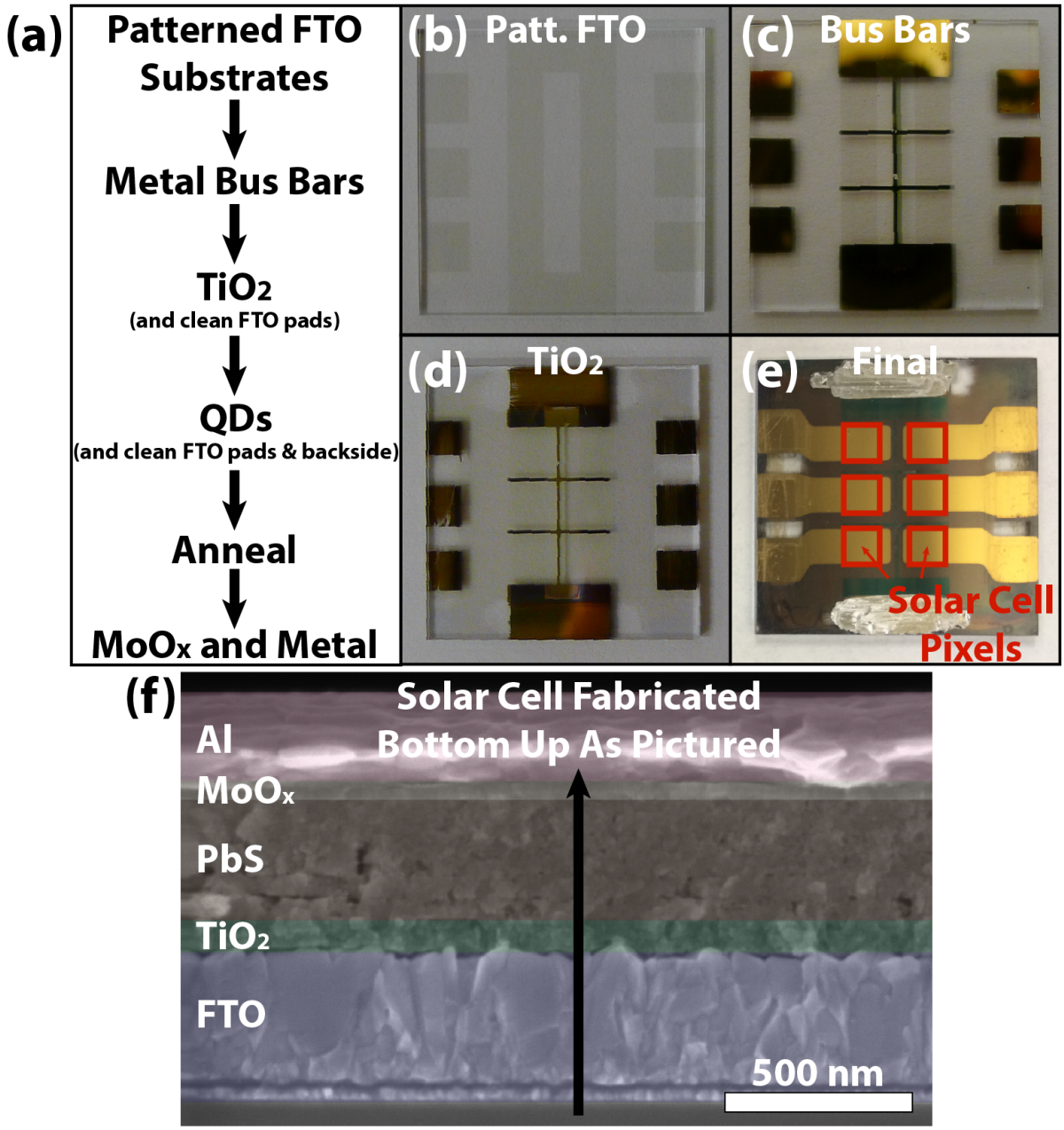


**Figure 2.1.** (a) Procedural flow diagram summarizing the steps involved in making a QD solar cell. (b) Glass substrate with FTO patterned as a rectangle in the middle, which we call the "racetrack," and six pads on two sides. (c) Substrate after metal (Au in photograph) bus bar deposition. (d) Substrate after TiO2 deposition. The lighter areas at the upper and lower pad areas, as oriented in the image, show where the TiO2 was removed using the cotton swab and ethanol. (e) Completed solar cell with Au "finger" contacts. Each of the six red boxes show an active area for an individual solar cell pixel, which is defined by the overlap of the top metal and bottom FTO contacts. The QD active layer has also been removed from the large FTO/metal pads in the upper and lower portions of the substrates as oriented in the photograph. Lastly, indium solder was added to the upper and lower FTO/metal pad regions to reduce contact resistance. (f) False color SEM image showing the cross-section of a completed solar cell.

**Preparation of Ligand Exchange Solutions**

The ligand-exchange solutions used in fabricating the QD absorber layer include: 10 mM $PbI_2$ in DMF, 10 vol.% MPA in methanol, and 1 mM EDT in acetonitrile. The stock $PbI_2$ powder is kept in a glove box and only the needed quantity removed. The $PbI_2$ is mixed with DMF in air to form the ligand-exchange solution, but the dissolution may be done inside the glove box as well. The mixture is sonicated for 10-30 minutes to completely dissolve the solid. We have found variability in the $PbI_2$ among different vendors and lots where certain batches of $PbI_2$ do not readily dissolve in the DMF. Therefore, we advise the usage of high purity $PbI_2$, such as that listed above. For the 1 mM EDT solution, a 1 M EDT in acetonitrile solution is prepared inside the glove box and then removed to air to be diluted as needed to 1 mM solutions. The >99% MPA stock solution is kept in ambient and the diluted 10 vol.% in-methanol solution is prepared in air.

**Summary of Solar Cell Fabrication**

The entire process (summarized in Figure 2.1a) starts with a glass substrate that is pre-patterned with FTO or ITO (Figure 2.1b: slightly gray regions are FTO). Our pattern is composed of a rectangular line, which we call the "racetrack," in the middle and six pads on the sides; other patterns can be employed using the general protocol developed here. To minimize the resistivity for current extraction in the non-active FTO regions we use metal bus bars deposited on top of the FTO and in between the six middle areas that will become six individual solar cell pixels, as shown in Figure 2.1c. Inclusion of metal bus bars leads to an increased fill factor, by reducing the series resistance of the substrate. After bus bar evaporation, the $TiO_2$ is deposited (Figure 2.1d), followed by QD layer deposition. (Although ZnO may be used instead of TiO2 as the n-type window and electron transport layer, we have observed significant

irreproducibility of performance when making solar cells with ZnO and have embraced TiO2 for this reason. Because of the high annealing temperature of TiO2 (450 °C), we predominantly use FTO for its favorable temperature stability compared to ITO. The resistivity of ITO increases with annealing at temperatures >200 °C,24 which would increase the series resistance in the solar cell.) Deposited $TiO_2$ and QDs are cleaned off the upper and lower pad regions of the FTO racetrack to serve as the bottom electrical contacts (soldered regions in upper and lower portion of the substrate in Figure 2.1e). Lastly, $MoO_x$ and metal (Au or Al) are deposited by thermal evaporation through a mask to form six contact lines, which we call "fingers," (Figure 2.1e) thereby forming six individual 0.101 $cm^2$ solar cell pixels. Electrical contact to the top of each of the six solar cell pixels is made by contacting the corresponding FTO/metal pad on the left or right side of the substrate, as oriented and shown in Figure 2.1e.

**Substrate Preparation and $TiO_2$ Layer Deposition**

1. The substrates are cleaned vigorously with an ethanol soaked scientific tissues, sprayed with ethanol from a squirt bottle, and then dried immediately with pressurized stream of air or $N_2$.
2. Silver bus bars, 75-100 nm thick, are deposited by thermal evaporation using a shadow mask. (The rate of evaporation is not critical; we deposit at 0.5-2 Å/second. Bus bars should be less than 100 nm to limit their impact on the $TiO_2$ film morphology.)
3. $TiO_2$ sol-gel precursor is prepared by mixing 5 mL ethanol, 2 drops hydrochloric acid and 125 µL deionized water in a beaker and stir. Then 375 µL of stock titanium(IV) ethoxide are added drop-wise. (Stock titanium(IV) ethoxide solution is stored in a glove box and only the necessary amount is removed to air.) The result is a clear liquid, free of any particulates. The solution is then capped and stirred for a minimum of one hour before

storing in the freezer. The sol-gel is removed from the freezer 10 min before use and stirred while it equilibrates to room temperature[25]. (The sol-gel mixture should be discarded if particulates are visible or if the solution is obviously cloudy or yellow.)

4. The $TiO_2$ layer is fabricated by spin coating 70 μL of the sol-gel at 1400 RPM for 30 sec. The $TiO_2$ sol-gel layer is removed from the upper and lower FTO/metal contact pads regions, and the smaller three left and three right FTO/metal pads, as oriented in Figure 2.1d, using a cotton swab moistened with ethanol immediately after the spin cycle is complete. The FTO/metal pad cleaning must be done immediately before the sol-gel solution dries. (Removing the $TiO_2$ sol-gel layer is more important over the large upper and lower FTO/metal pad areas. The other six, smaller, FTO/metal pads on the sides will be coated with the metal top contacts, and therefore having clean FTO pads helps in case the contact probes poking through the evaporated metal layer.) After wiping the FTO/metal pads, each substrate is kept on a hotplate at 115 $^{o}$C, to remove water, while the next substrate is prepared. After the last substrate is finished, the substrates are kept on the hotplate for an additional 20 minutes.
5. Finally, the substrates are placed in a preheated furnace at 450°C for 30 min, regardless of whether the substrate is FTO or ITO coated glass. The films are then stored in air, in the dark, prior to QD film deposition.

**QD Layer Deposition**

The QD layer is commonly deposited using multiple spin coating or dip coating cycles. The number of spin or dip cycles along with the QD concentration determines the QD film thickness. Both methods are highly tunable (*e.g.*, layer thickness and ligand exchange) and both result in solar cells of comparable performance. The choice of which method to use is largely a

personal preference. Dip coating requires enough total volume to immerse the substrate. Therefore, the QD solution concentration is typically lower when dip coating (e.g., 10-20 mg/mL) than in the case of spin coating (~30 mg/mL). As a result, dip coating is generally a slower deposition method, because each individual cycle deposits fewer QDs, but this may be preferred for finer control when very thin QD films are desired and for the potential to deposit more solar cells from a single QD synthesis. Higher (lower) solution concentrations will yield thicker (thinner) layers per cycle and thus quicker (slower) film fabrication. A disadvantage of spin coating is that some of the material is lost as it is spun off the substrate. Before starting, remember the French culinary phase, "mise en place," which refers to the importance of preparing and arranging all of the components and tools in an organized fashion prior to cooking, or making solar cells. Additionally, we highly recommend the tweezers visible in Figure 2.2 and Figure 2.3 (VWR 100494-780) because the wide tip prevents rotation of the substrate about the hold point. The procedures below apply to lead chalcogenide QDs that have native oleate ligands.

**Spin Coating Protocol**

Prior to spin coating, the QDs are dispersed in octane at a concentration of 30 mg/mL. The solution is filtered through a 0.2 μm Nylon or PTFE filter to remove agglomerates and increase the uniformity of the film.

1. 80 μL of QD solution, enough to cover the middle portion of the substrate containing the six solar cell active areas, is dispensed onto a substrate using a micropipetter. The solution should be spread evenly to cover the entire surface. (If an air bubble forms, it is important to remove the bubble by perturbing the solution via puffs of air using the now empty micropipetter.)

2. The substrate is spun at 2000 RPM for 30 seconds, with a 3 second ramp rate, in order to obtain a glassy film and dry the octane. (If there is any excess liquid on the back of the substrate, this should be dried on a scientific tissue before the ligand treatment.)
3. The QD film is then submerged in the 10 mM $PbI_2$ solution for 3 minutes to ensure complete exchange.
4. When removing the substrate from the DMF solution, the film is tapped against the side of the beaker to let the excess DMF run back into the ligand solution.
5. The film is then submerged multiple times in neat acetonitrile to remove excess DMF and $PbI_2$. It is important to set the film on its edge in the acetonitrile and open the tweezers to release the DMF trapped between the tweezers and the substrate.
6. The film is then dried using a gentle stream of air to push the acetonitrile off the film edge. Steps 1-6 are done a total of four times to build up the $PbI_2$ layer (Figure 2.2a).
7. The MPA treated layer is spun in the same way, but 10 vol.% MPA-in-methanol is used as the ligand-exchange solution. The film is slowly lowered into the MPA solution, held for ~1 s, then steadily removed and rinsed in neat methanol. The film is dried with a gentle stream of air (~4 seconds total exposure time). This procedure is done a total of two times to build up the MPA layer. (If excess MPA solution is not adequately rinsed, the film will develop white cloudy areas when the next QD layer is deposited from octane. Any pixels affected by this cloudiness will be Ohmic (not exhibiting rectifying behavior), so discard the film if too many pixels are affected. To avoid this problem, the film should be rinsed multiple times in the neat methanol. If the film begins peeling during the MPA treatment, as shown in Figure 2.2b, reduce the concentration of the MPA to 1 vol.% in methanol. Peeling during the MPA treatment is a greater issue if ZnO is

used instead of $TiO_2$, in which case we recommend reducing the MPA concentration. We have found that the MPA concentration, within the range of 1 vol.% to 10 vol.%, does not produce statistically significant differences in the solar cell performance.)

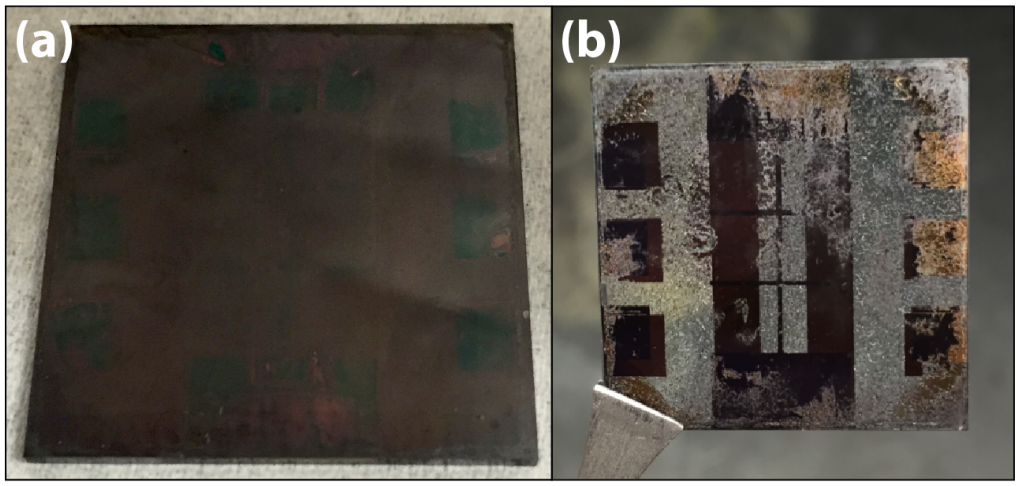


**Figure 2.2.** (a) A typical film after spin coating in contrast to (b) a film that peeled during the MPA treatment.

An alternative spin coating approach involves performing the ligand treatments directly on top of the film while leaving the substrate in the spin coater. Our technique differs because of the long soak time in the $PbI_2$/DMF solution. By dip coating this treatment, it is possible to process four films simultaneously by letting three of the films soak in the ligand treatment while the QD layer is being deposited on the fourth film. (We used a fourslot substrate holder that fits inside the beaker for soaking substrates in the PbI2/DMF solution.) Although the QD layers may be treated by via deposition of ligand solution directly on the film in the spin coater, we prefer the soaking route described above for higher throughput.

**Dip Coating Protocol**

When dip coating, the QDs are dispersed in hexane at a concentration of ~15 mg/mL. Prior to deposition, the QDs are filtered through a 0.2 μm Nylon or PTFE filter to remove agglomerates. Ligand solutions that are reused from prior depositions should be filtered as well. During deposition, any beaker that is not in use is covered with a watch glass to slow evaporation and block dust. A table is drawn on the fume hood window and the dip count is indicated via tick marks to keep track of film thickness. Traditionally, QD solar cells were dip coated with EDT ligand treatment. To dip coat QD layers with EDT, or other similar organic ligands, the following procedures are used.

1. The substrate is lowered gently and vertically into the QD solution and then gently and vertically removed from the solution. When lowering the substrate into the QD solution, stop before any of the solution wets the tweezers. (If any of the QD solution is entrained in the tweezers, then a droplet may flow down the newly formed film and disrupt uniformity upon substrate removal.) The QD layer deposition occurs during the substrate withdrawal so the speed of lowering is not important. A good withdrawal speed is approximately 2 seconds to remove a 1" long substrate (~1.3 cm/s). Removing the substrate quickly yields thicker films, as more solution is trapped on the substrate, but uniformity and homogeneity usually suffer. (If the film is non-uniform the substrate may be re-submerged into the QD solution. It is important to do this before ligand exchange. The substrate should be kept submerged in the QD solution for ~5-15 seconds to allow for dispersion of the non-uniform layer.)
2. When the substrate is clear of the solution, tap the bottom edge of the substrate onto a paper towel/wipe to remove any excess QD solution. (If allowed to dry, the excess QDs

may flake off during the ligand exchange.) The hexane should be completely dry before dipping into the ligand solution.

3. Next, the QD-coated-substrate is dipped into the ligand solution, which in this case is 1 mM EDT in acetonitrile. Similar dipping speeds are used for the ligand exchange, but a 1 second soak while the film is submerged is included prior to removal.
4. After removal from the EDT solution, the film should be allowed to dry. (If any droplets of solution are entrained on the film upon removal, they should be blown off with compressed nitrogen gas.)
5. Once dry, the film is turned 90° and then it is dipped into the QD solution again and the process is repeated. Turning the substrate 90° helps to even out directional non-uniformities.
6. We recommend using a profilometer to calibrate the QD thickness per dip cycle to determine when to finish the total QD film deposition.

We also use dip coating to fabricated QD solar cells using the combination of $PbI_2$ and MPA ligands treatments described in the spin coating section; the procedure is slightly modified:

1. The substrate is dipped into the $PbI_2$/DMF solution at the same rate as in the case of EDT but with a 10 second soak before removal from the ligand exchange solution.
2. Immediately following removal of the substrate from the $PbI_2$ solution, the substrate is dunked into neat acetonitrile to remove excess DMF and excess $PbI_2$. Still submerged in acetonitrile, the tweezers are opened and closed a couple times to also remove excess $PbI_2$/DMF from the tweezers.

3. The substrate is then removed from the acetonitrile rinse and dried immediately using compressed nitrogen gas or compressed clean air. It is a good idea to put down the substrate and remove the liquid stuck on the tweezers by clamping them onto a tissue.
4. The substrate is then turned 90° and the process is repeated.
5. After ligand exchange with $PbI_2$, the QDs do not adhere well to the glass backside of the substrate. The QD on the backside may be disrupted and flake into the $PbI_2$/DMF and/or acetonitrile rinse solution. The flaked QDs will float on top of the solution(s). An oily residue containing the oleate ligands may also develop in the solutions. The flakes and oils may be removed by carefully scooping with a folded scientific tissue. Alternatively, the $PbI_2$ solution or acetonitrile rinse may be replaced. The flakes should be minimized either way to avoid their entrainment in the QD film. Generally, the QDs will flake at a reduced rate as the film thickness increases on the back of the substrate. Reducing the $PbI_2$ concentration (*e.g.*, 1 mM instead of 10 mM) will reduce the rate of film flaking. If the QD layer thickness per dip is $\leq$ 20 nm, using a $PbI_2$/DMF concentration in the range of 1 mM to 10 mM is acceptable without increasing the dip/soak time. If the QDs are flaking off the front surface of the substrate, then reducing the $PbI_2$ concentration is recommended. The rate of flaking may decrease as the film thickness is increased, but inhomogeneities may be introduced by the initial flakiness.
6. Prior to depositing QDs with the second ligand (e.g., MPA), an average thickness-per-dip is calculated using a profilometer to determine the required number of dips for the desired thickness. This is mainly done to keep absorber layer thickness a constant when the goal is to compare solar cell performance of different QD batches.

7. After the $PbI_2$-treated layers are finished, the MPA ligand treatment is performed in the same way as described in step 7 of the spin coating procedure, except that each fresh layer of QDs is deposited by dip coating.

In the case of solar cells containing QDs with $PbI_2$ and MPA ligands, the the thickness ratio of the total $PbI_2$-treated layer and the total MPA-treated layer is 2:1 (100 nm of MPA-treated QDs and 200 nm of $PbI_2$-treated QDs).

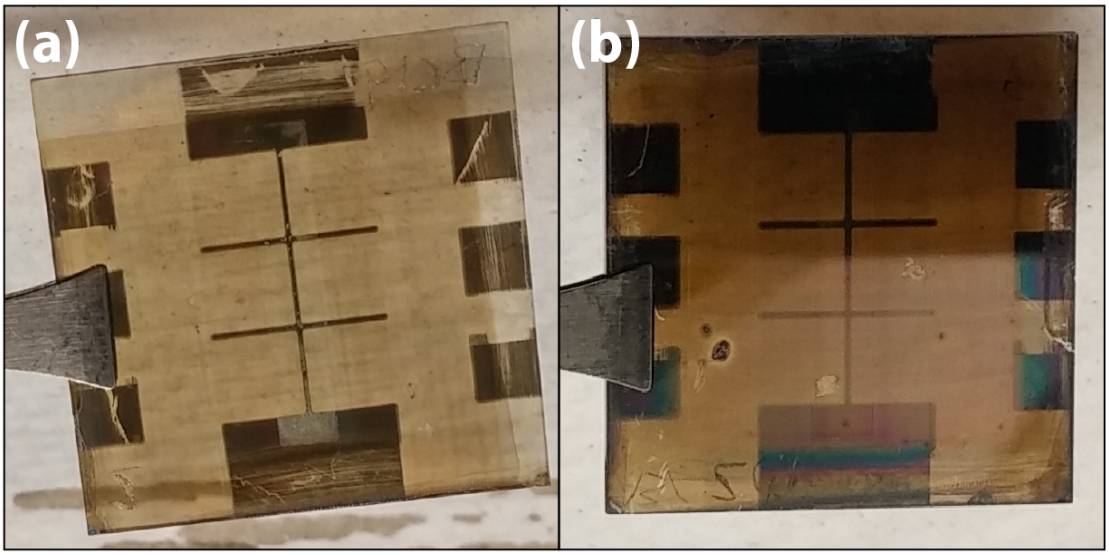


**Figure 2.3.** (a) The film after ~25 nm and (b) ~150 nm of EDT-treated ~0.63 eV PbSe QDs. The glass side of the substrates was cleaned in both cases. Imperfections may develop during the coating process. For example, there is a dark spot in the bottom-left, near the tweezers, which was a result of QD-agglomerates that float in the ligand exchange solution entrained in the film. This dark spot is not in an active solar cell area, however, and did not affect solar cell performance. On the other hand, some imperfections may not have significant impact on pixel performance, such as the light imperfection over the middle-right pixel.

When the QD film deposition is finished, the glass side of the substrate is cleaned with solvent-soaked (*e.g.*, methanol, ethanol, or acetonitrile) cotton swabs. On the active area side, the large upper and lower FTO/metal contact pad regions, as oriented in Figure 2.1e, should be cleaned carefully such that the cotton or solvent does not touch the six pixel areas. The six side finger pads are cleaned as well.

Following cleaning of the FTO pads, the films are annealed in an $N_2$-filled glove box ($O_2$ at <5 ppm, $H_2O$ <1 ppm) at 110° for 20 minutes. Annealing optimization should be performed for different QD and ligand combinations. We refer the reader to Gao, et al.[26] for guidelines on optimizing the annealing step.

**Top Contact Layer and Finishing the Solar Cell**

After annealing, the back contact layers are deposited on the film by thermal evaporation. We deposit 15-20 nm of $MoO_x$ and 100-150 nm of Al or Au. For deposition, films are loaded into an evaporator and the chamber is evacuated to a base pressure of $10^{-7}$ - $10^{-8}$ Torr. The $MoO_x$ layer is evaporated slowly at a rate of 0.02 nm/s. The Al or Au is then deposited at a rate of 1.5 nm/s. These depositions are done in a thermal evaporator with multiple sources to avoid exposing the film to air between $MoO_x$ and Al or Au depositions.

A false color cross-sectional scanning electron microscopy (SEM) image of a completed solar cell (Figure 2.1f) demonstrates highly uniform and smooth QD films that should result from following the protocol developed above. The finished solar cells are stored in a drawer, under ambient conditions, before and after characterization.

**Characterization: Current-Voltage Response**

JV (current density vs. voltage) characterization of the solar cells is performed in an oxygen-free environment using an Oriel Sol3A (94043A) class AAA solar simulator system equipped with a 450 W Xenon arc lamp and an AM1.5G filter. (Measuring the solar cells in air leads to a reduction in fill factor, which recovers when the cell is returned to inert atmosphere.) A metal plate is used to aperture (0.059$cm^2$) each of the six pixels during characterization to prevent illuminating areas outside of the defined active area, which would artificially inflate the PCE[27,28]. It should be noted that during the JV measurement of any single pixel, the other five

pixels are illuminated and held at open circuit. The total pixel area (0.101 $cm^2$) or the aperture area is used to calculate the current density in the dark or under illuminated conditions, respectively. The height of the solar cell stage is adjusted until the illumination intensity is 100 $mW/cm^2$, as determined by the current output of the calibrated Hamamatsu (S1787-04) silicon reference photodiode. A mismatch factor may be applied to correct the short circuit current ($J_{sc}$) value as appropriate depending on the QD size and cell responsivity[27]. Figure 2.4 shows example JV curves for solar cells with PbSe (blue) or PbS (red) QDs. Although QD solar cells do not exhibit the hysteretic behavior observed in perovskite solar cells,[11] measurement stress effects have been observed, such as a decrease in Voc due to light soaking under open circuit conditions. We observe an efficiency standard deviation of ±10% about the average. Deviations arise due to nonuniformities across the substrate area, as well as the measurement stress effects

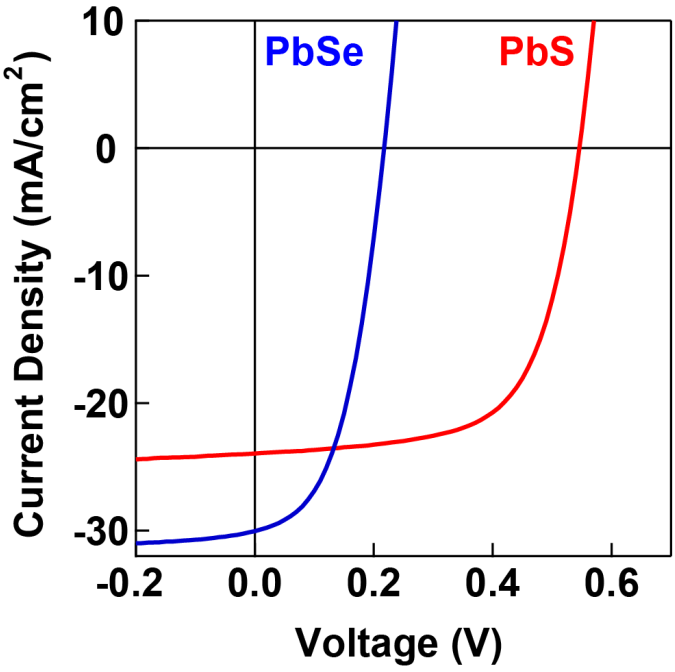


**Figure 2.4.** Example JV response of PbSe (0.78 eV) and PbS (1.2 eV) QD devices. The efficiency, fill factor, Voc, and Jsc of the PbSe solar cell are 3.15%, 48.2%, 0.217 V, and 30.0 $mA/cm^2$, respectively. The efficiency, fill factor, Voc, and Jsc of the PbS solar cell are 8.36%, 64.0%, 0.546 V, and 23.9 $mA/cm^2$, respectively. The architecture of these cells was as shown in Figure 2.1.

**Characterization: Spectral Response / Quantum Efficiency**

The external quantum efficiency (EQE) measurement is used to characterize current losses in the solar cell as a function of photon energy or wavelength. It is a measurement of the flux of electrons, measured as current density, in a solar cell with respect to the flux of photons incident on the solar cell. The EQE is also called the IPCE, or incident-photon-to-current-efficiency. Losses in the EQE may include: parasitic UV and IR absorbance in the hole or electron extracting layers (*e.g.*, FTO, $TiO_2$, or $MoO_x$), reflections at interfaces, inadequate absorber thickness leading to loss in the IR, and short carrier diffusion lengths in the QD layer or electron (hole) extracting layers. The measurement instrumentation involves a light source, monochromator, chopper, light filters, light guide, probe setup to measure current, a pre-amplifier, and a lock-in amplifier. More details on the instrumentation, measurement, and calculation may be found elsewhere[27,29–31].

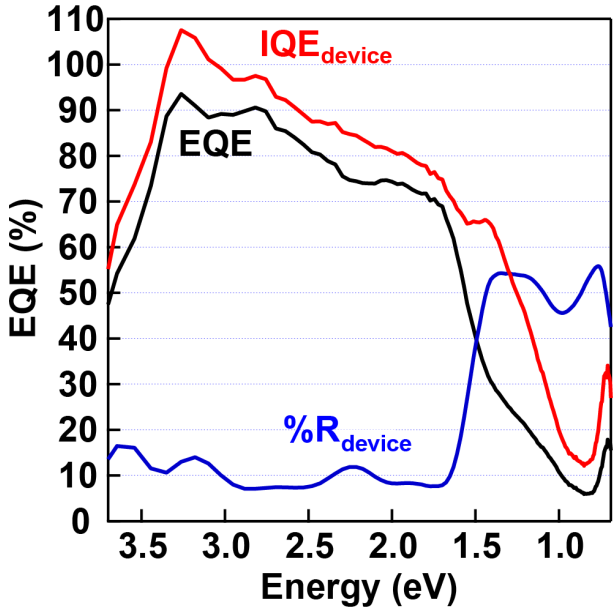


**Figure 2.5.** Example EQE, reflectance, and $IQE_{device}$ spectra of PbSe QD solar cells (0.72 eV). An $IQE_{device}$ above 100% indicates that MEG is contributing to the collected current[16]. The architecture of this cell was as shown in Figure 2.1.

Another important spectral response measurement is the internal quantum efficiency (IQE). One of the losses in solar cells arises from reflections, which are accounted for in the IQE measurement. Reflections prevent a fraction of light from reaching the QDs and therefore those incident photons are lost and not converted to current. The IQE may be calculated in two different ways: IQE of the device or IQE of the absorber material. In the former case, the $IQE_{device}$ is QE after accounting for reflective losses off the entire device stack. Thus, the $IQE_{device}$ is the measured electron flux divided by the photon flux absorbed by the entire dielectric stack that makes up the solar cell. For example, Figure 2.5 shows an EQE and $IQE_{device}$ for a PbSe QD solar cell. In the example solar cell, the $IQE_{device}$ is greater than 100% in the UV region, indicating that MEG is contributing to the solar cell performance[16]. In the other case, the $IQE_{absorber}$ is the QE after accounting for reflective losses at all interfaces and absorptive losses in all materials except for the QD absorber layer. In other words, $IQE_{absorber}$ is the measured electron flux divided by the photon flux absorbed only by the active layer (*i.e.*, the QDs). Thus $IQE_{absorber}$ is always larger than $IQE_{device}$. Some instrumental setups allow for measuring the reflectance spectrum (specular ± diffuse reflectance) simultaneously with the EQE measurement. Alternatively, the reflectance spectrum may be obtained using a UV-Vis-NIR spectrophotometer equipped with an integrating sphere. To do so we make a twin (witness) QD solar cell on an unpatterned substrate in the same session as the patterned solar cells. The back contacts are deposited onto the entirety of the twin substrate. The reflectance spectrum of the device is then obtained by measuring the reflectance of the twin film in a Shimadzu UV-Vis-NIR-3600 spectrophotometer equipped with a 60 mm integrating sphere ($8^o$ incidence angle) and a NIST-calibrated specular reflectance standard (STAN-SSH, Ocean Optics). The $IQE_{device}$, for example, is then calculated as $EQE/(1-R_{device})$, where $R_{device}$ is the reflectance spectrum of the twin cell. To

measure the $IQE_{absorber}$, one needs to calculate the reflectance at each interface and the absorbance in each material. More details specific to QD solar cells are available in Semonin et al. and Law et al.[16,29] Additional information regarding accounting for losses in the spectral responsivity of solar cells may be found elsewhere[27,30,31].

### 2.4 Quantum Dot Synthesis Protocol

#### Preparation

All reagents are purchased from Sigma Aldrich and are used as received. 1-octadecene (ODE, technical grade), oleylamine (OLA, technical grade), oleic acid (OA, technical grade), $PbCl_2$ (99.999% trace metals basis), CdO (≥99.99% trace metals basis), $S(NH_4)_2$ (40-48 wt. % in $H_2O$), selenium (powder ~100 mesh, 99.99% trace metals basis), trioctylphosphine (TOP), hexane (reagent grade), and ethanol (200 proof, reagent grade).

#### General Synthetic Notes

1. The synthesis of CdS QDs is modified from that published by Robinson et al.[32], but without drying the sulfur precursor, and Zhang et al.[22] The synthesis of CdSe QDs is modified from that published by Peng et al.[33] and Zhang et al.[23] The syntheses of PbS and PbSe QDs by cation exchange reactions from CdS and CdSe, respectively, are modified from that published in Zhang et al.[22,23]
2. At the beginning of a synthesis, reagents are degassed before heating. This is done by evacuating the flask atmosphere using the Schlenk line for 1-2 minutes, or until bubbling has ceased, then flushing with $N_2$ and repeating for a total of 3 cycles before the heating mantle is turned on.
3. The vacuum base pressure should be 20 – 100 mTorr.

4. When an injection is used to initiate a reaction, 16 gauge needles and 20 mL syringes are used regardless of the amount of liquid being injected. This ensures a quick injection, which will improve the size distribution of the product.

**Synthesis of CdS QDs**

1. The precursor solution is prepared with 0.66 g CdO, 4 g OA, and 18 g ODE in a 100 mL round bottom flask.
2. The reagents are stirred and heated to 260 °C. The solution is further degassed by alternating between vacuum and $N_2$ while the solution temperature is <80 °C. At >80 °C the atmosphere in the flask is switched to $N_2$. (To minimize air leakage into the flask atmosphere, the $N_2$ pressure in the Schlenk line should be high enough such that excess $N_2$ escapes through the bubbler, which is part of the Schlenk line.)
3. Meanwhile, 180 μL of $(NH_4)_2S$ is added to 15 mL OLA and stirred vigorously. This mixture outgasses aggressively and should not be capped. The ammonium sulfide will form a gel when added into the OLA and should be allowed to completely dissolve before injection into the Cd-oleate solution. (The vial may be capped temporarily while briefly shaking the solution to aid dissolution, but the cap must then be loosened completely.)
4. The reaction is left at 260 °C until all of the burgundy color has disappeared and the solution turns clear, indicating that the CdO has converted to Cd-oleate. It is important for all of the CdO to be reacted before the next step. (Gently shaking or rocking the flask helps to remove unconverted CdO from the flask walls.)
5. The flask is removed from the heating mantle and allowed to cool to just above room temperature (32 °C).

6. The heating mantle is replaced and the temperature control is set to 32 °C.
7. The ammonium sulfide / OLA solution is then injected into the flask and allowed to react for 1 hour. (If the reaction is stopped sooner, yields will be low.)
8. After 1 hour, the heating mantle is removed and the reaction liquor is distributed into centrifuge tubes each with 5-10 mL of reaction liquor. Then, hexane is added until each tube contains 20-25 mL total solution. This step is important because trying to precipitate the QDs directly from the reaction liquor will result in oil instead of a solid precipitate after centrifugation. Ethanol is then added until the transparent yellow solution is opaque (25 mL). The mixture is centrifuged at 7500 RPM for 5 min. The exact time and speed of centrifugation is not critical, as long as the result is a solid precipitate and a (mostly) colorless supernatant. (If a solid precipitate is not obtained, we recommend using a higher hexane:liquor ratio and/or using a lower solvent:antisolvent volume ratio.
9. The CdS QDs are dispersed in ~9 mL of toluene. It is important to wash (precipitate) the product only a single time, otherwise the QDs in toluene may form a gel that cannot be extracted into a syringe for injection. This reaction consistently produces QDs with a first exciton peak at 366 nm.

**Synthesis of CdSe QDs**

1. The precursor solution is prepared by mixing 0.512 g CdO, 6.28 g OA, and 25 g ODE and heating in the same way as in the CdS synthesis steps 1 and 2.
2. While heating the reagents, 0.063 g (0.8 mmol) Se powder is added to 5 mL ODE and sonicated for 10 min. Also, 3 mL of 1 M TOPSe is mixed with 7 mL ODE and loaded into a syringe pump.

a. The timing of the sonication is not critical, except that the mixture should be actively sonicated immediately before loading a syringe for injection. The Se powder will settle out of the ODE if left for more than a few minutes. We recommend at least 10 minutes of sonication in order to disperse the Se powder well, but it can certainly be sonicated much longer so that it does not settle before injection.

b. The TOPSe solution is made by stirring 0.1 mol Se powder in 100 mL TOP in the glove box for at least 3 hours. All of the Se powder should be dissolved to form a transparent, yellow-tinted solution before use in the synthesis. If kept in the glove box the TOPSe can be used over a long period of time. A strong yellow color or precipitate at the bottom of the bottle is an indication that the TOPSe has oxidized and should not be used.

3. The Se/ODE mixture is injected at 260 °C and the temperature controller is set to 240 °C.
4. After 1 minute from injection, the TOPSe/ODE solution is added dropwise at ~1 drop/second. This is set by eye using the syringe pump. (It is also possible to do this step by hand, although we see better consistency with a mechanical syringe pump. If injecting the TOPSe/ODE solution by hand, it is important to be as steady as possible to improve the size distribution of the final CdSe.)
5. During the TOPSe/ODE addition, monitor the reaction by UV-Vis absorbance until the desired size is achieved. This step is most easily done by drawing small aliquots (~0.1 mL) that are quenched in a cuvette filled with hexane (~ 2 mL). Aliquots should be taken every 5-10 minutes to track the growth of the QDs.

6. When the first exciton of the CdSe QD peak has reached 600 nm, the addition of the TOPSe/ODE mixture is stopped and 2 minutes later the heating mantle is turned off and removed, allowing the QDs to cool to room temperature. On average, there is ~3 mL of the TOPSe/ODE mixture leftover and the total reaction time is ~30 minutes. This will vary depending on the dripping speed, in general the slower additions of TOPSe/ODE result in greater monodispersity in the final sample.
7. The reaction liquor is split into enough 50 mL centrifuge tubes such that there is ~5 mL of liquor in each tube. Approximately 20 mL of hexane is added to each tube and each tube is then capped and shaken well. 25 mL of ethanol is added to each tube and the tubes are centrifuged at 7500 RPM for 5 minutes. Often, this first precipitation results in a slightly colored supernatant and it is discarded while keeping the precipitated QDs.
8. The QD product is washed twice more by dispersing each QD precipitate in 10 mL of hexane, and then precipitating with an equal volume of ethanol. After the final wash, the QD product is dispersed in 9 mL ODE. Dipsersing the QDs will require the aid of a vortex mixer. If the CdSe QDs will be stored a long time, it is advised to bring them into a glove box before finally dispersing in ODE.
9. A CdSe QD product with good size distribution will have a sharp first exciton peak and a clear second excitonic feature, as seen in Figure 2.6.

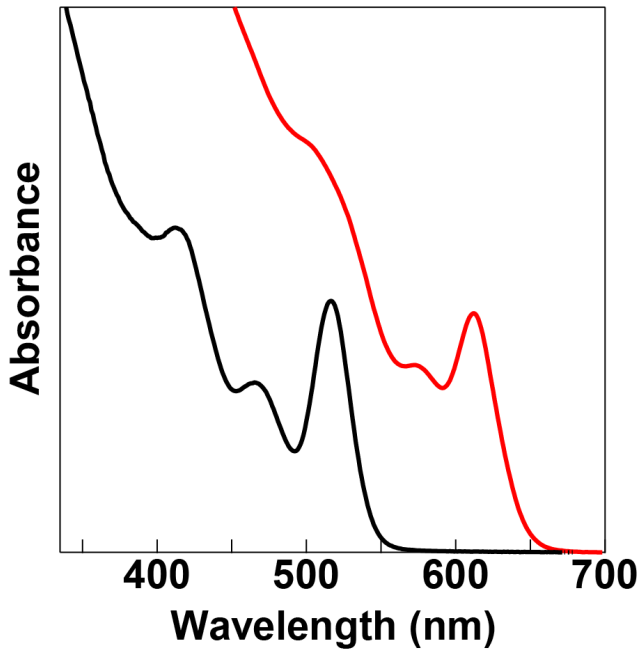


**Figure 2.6**. Example absorbance spectra of CdSe QDs with the peak of the first exciton at 515 nm (black) and 610 nm (red).

**Cation Exchange Reaction from CdS (CdSe) to PbS (PbSe)**

PbSe (PbS) QDs are synthesized by a cation exchange reaction from CdSe (CdS) QDs.

1. The precursor solution is prepared by mixing 0.834 g (3 mmol) $PbCl_2$ and 10 mL (3 mmol) OLA in a 100 mL round bottom flask.
2. The mixture is heated to 100 °C while stirring and degassing with alternating between vacuum and $N_2$. At 100°C, a needle is inserted into one septum, as shown in Figure 2.7a, to flow $N_2$ over the reagents for ~5 minutes and further remove any water not removed during degassing.
3. The mixture is heated to 140 °C and the vent needle is removed. As the suspension is heated, $PbCl_2$ and OLA form a complex and the solution begins to turn clear and colorless (Figure 2.7a). At temperatures ≥140 °C, the solution will turn turbid and white again (Figure 2.7b). The solution temperature is maintained at 140 °C for 10 minutes.

The 10 minute hold is not critical as long as the milky white solution is obtained before the CdSe (CdS) QDs are injected.

   a. As the $PbCl_2$/OLA complex is formed we have observed some differences in color at this stage of the reaction. Occasionally, the solution will stay clear until heated to a higher temperature (>145 °C) or the solution will have a pink hue after the complex forms. Neither case has had a detrimental effect on the synthesis.

4. The reaction bath is heated or cooled to the injection temperature (90°C to synthesize 1.3 eV PbS QDs, and 195°C to synthesize 0.7 eV PbSe QDs) and 2-3 mL of CdSe (CdS) QDs (capped with Cd-oleate, 50-100 mg/mL in ODE) are injected using a 20 mL syringe and 16-gauge needle. Approximately 200 mg total of CdSe (CdS) QDs should be injected. There is an immediate color change to dark brown upon injection as the cation exchange reaction proceeds. The large diameter syringe and needle are important to ensure a swift injection of the CdSe (CdS) NCs. The resulting lead QDs will have a broad size distribution if the CdSe (CdS) QDs are not injected quickly enough.
5. The reaction is allowed to run for 30 – 60 seconds (depending on the desired size) before removing the mantle and immediately quenching by submerging the flask in a water bath. (If the reaction temperature is too low and/or the reaction time is too short, a mixture of CdS(e) and PbS(e) QDs will be obtained, including Janus particles, as discussed in earlier manuscripts[22,23].)
6. At 70°C, 10 mL hexane is injected to assist cooling. At 30°C, 8 mL OA is injected to replace the weakly bound OLA ligands on the surface of the PbSe (PbS) QDs. The OA injection will raise the temperature of the reaction solution to ~45°C and the reaction should be allowed to cool below 30°C again before exposing the solution to air.

7. The cooled product is poured into 2, 50 mL centrifuge tubes, split evenly such that each tube contains 15 mL reaction product. Extra hexane (5 mL) is used to rinse the round-bottom flask and this is also added to the centrifuge tubes. Then, 20 mL of ethanol is added to each tube in order to precipitate the QDs.
8. The mixture is centrifuged for 5 minutes at 7500 RPM.
9. The resulting supernatant should be (mostly) colorless and is discarded (Figure 2.8a). If the supernatant has a darker color, extra ethanol is added (2 - 4 mL) and the tubes are centrifuged again.
10. The solid QD precipitate in each tube is dispersed using 10 mL of hexane, the solutions are combined into one centrifuge tube, and the tube is centrifuged without addition of an antisolvent. This step precipitates the excess chlorides from the solution, which will result in a white precipitate (Figure 2.8d).
11. The QD solution is extracted into a syringe and then filtered through a 0.2 μm filter into a clean centrifuge tube. The latter step further removes excess chloride salts.
12. A final wash is done by precipitating with ~20 mL ethanol (or until the solution is cloudy brown) and centrifuged as above.
13. For dip-coating, QDs are dispersed in hexane at 10-20 mg/mL. For spin-coating, QDs are dispersed in octane at 30 mg/mL.

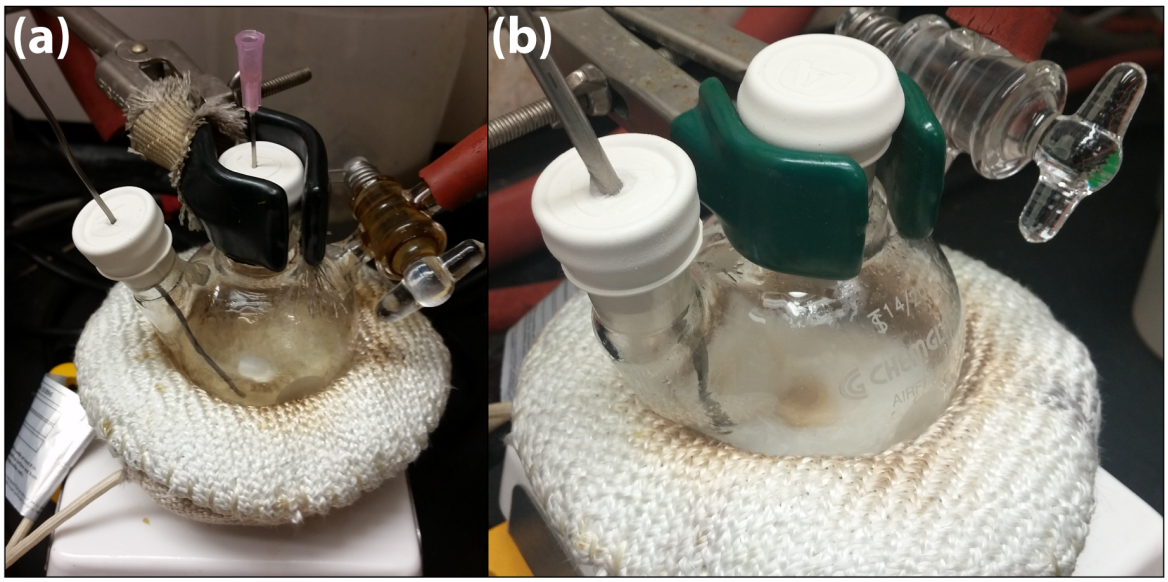


**Figure 2.7.** (a) As the $PbCl_2$/OLA mixture is heated, it goes through a clear phase. (b) A milky white solution forms after heating the $PbCl_2$/OLA mixture to ≥ 140°C.

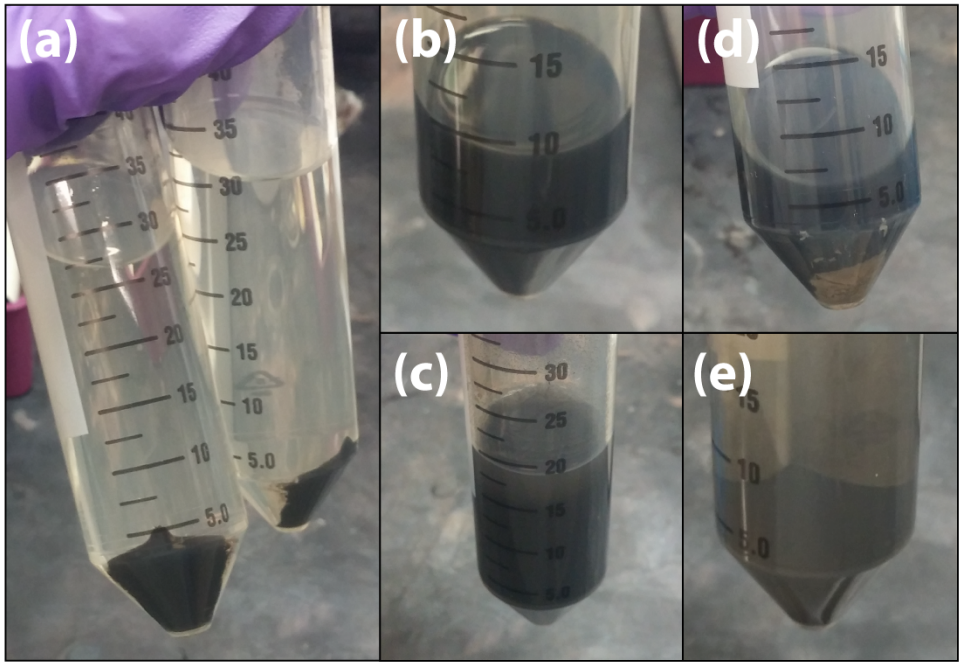


**Figure 2.8.** The washing procedure for cation exchanged QDs: (a) the precipitate formed at the bottom of the centrifuge tube after precipitation and centrifugation; (b) QDs fully dispersed in hexane; (c) gray, cloudy solution that results from the precipitation with ethanol; (d) white precipitate of excess chlorides after centrifugation in neat hexane; and (e) final precipitation and centrifugation. Notice that the tube walls have some QDs stuck to them above the main solid QD precipitate, which is a sign that the QDs are well washed.

**QD Characterization**

After every synthesis, the QDs are characterized by UV-Vis-NIR absorbance spectroscopy. The absorbance spectra are used to determine the QD size, polydispersity, and concentration. Polydispersity is gauged via the width of the first exciton peak. Figure 2.9 shows example of acceptable and unacceptable polydispersity of (9a) PbS and (999b) PbSe QDs. The polydisperse QD batch should not be used or size selective precipitation should be performed to isolate more monodisperse QDs.

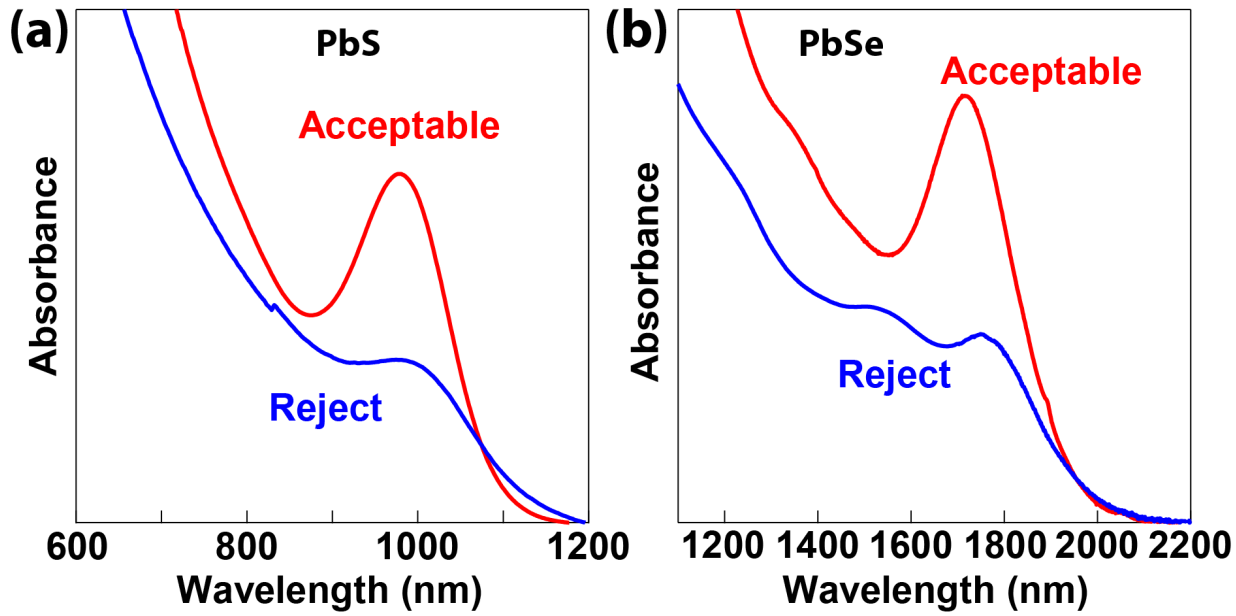


**Figure 2.9.** Examples of (red) acceptable and (blue) unacceptable absorbance spectra of (a) PbS and (b) PbSe QDs.

**2.5 Discussion and Conclusions**

The efficiency of QD solar cells has increased from 2.1% in 2008[34] to 11.3% in 2016[35]. This accelerated progress was accomplished through a combination of advances in the field revolving around the solar cell architecture and control of the QD surface, including band energetics and defect passivation. The solar cell architecture was improved by moving from a Schottky junction[34] to a heterojunction with selective contacts for hole and electron extraction

from the QD absorber layer[36]. Further architecture optimizations were made aimed at improving charge carrier collection efficiency through modification of the electric field at the junctions[37,38], for example, by using highly doped n-type $MoO_x$ as the hole extracting contact layer[39]. In 2011, Semonin et al. showed that the use of two different ligand treatments during the deposition of the QD absorber layer (i.e., EDT-treated QDs followed by hydrazine-treated QDs) led to significant improvements in QD solar cell performance[40]. Since then, QD solar cells have been made with two ligand treatments, such as tetrabutylammonium iodide (TBAI) followed by EDT[41]. Brown et al. then further opened the door to band alignment engineering within the QD absorber film by demonstrating control over conduction and valence band energy levels through varying the ligand molecules on the QD surface through solid state ligand exchange[1]. Likewise, the tunability of the QD Fermi level was demonstrated by control of the QD surface stoichiometry through solid state ligand exchange[42]. The range of beneficial ligand treatments in solar cells was later expanded with inorganic molecules, such as $PbI_2$, which also allowed QD solar cells to be made thicker than before, thereby absorbing a higher fraction of incident light[43,44]. Beyond tuning the QD energetic alignment, control of the QD surface further encompassed surface trap passivation through both solid state ligand exchanges[45,46] and synthetic protocols[47,48]. For example, Ip et al. showed that in-situ addition of $CdCl_2$ at the last stage of synthesis resulted in the reduction of mid-gap trap state density[47]. The trap reduction was attributed to partial passivation of the QD surface by halide anions. Other synthetic advances, such as the cation exchange reactions described here, have similarly demonstrated reduced trap densities[48] and prolonged air stability[49] in lead-chalcogenide QDs. It is important to note that different synthetic procedures influence the QD surface termination. Traditional, lead(II) oxide-based, syntheses for lead-chalcogenide QDs leave Pb-oleate ligands on the QD surface[50]. In contrast, the cation

exchange reactions described here produce lead-chalcogenide QD surfaces terminated with a combination of Cd-oleate, Pb-oleate, and Cl-ions[23,43,51]. Therefore, the QD surface termination, the QD energetic alignment, trap density, and Fermi level, may vary even in the case of identical solid ligand exchanges performed on QDs synthesized by different methods. For example, solid-state ligand exchange may not remove the surface-bound Cl-ions. These nuances influence solar cell performance differences among different research groups, and represent an array of both challenges and opportunities to continued advances in the field.

Further improvements in QD solar cells will be achieved through continued investigation of the solar cell architecture, control of QD surface through novel ligand exchanges, new or improved syntheses, and novel materials such as heterostructures[6,22,52,53]. These advances can be accelerated through the ability to make in-house state-of-the-art prototype QD solar cells to serve as test beds for these investigations and for realizing the full potential of QD solar cells beyond the Shockley–Queisser limit[54–56].

**2.6 Acknowledgements**

We acknowledge support from the Center for Advanced Solar Photophysics (CASP), an Energy Frontier Research Center funded by the US Department of Energy, Office of Science, Office of Basic Energy Sciences for quantum dot coupling and solar cell structures. G.P. acknowledges the support from the Global Frontier R&D program (1415134409) funded by KIAT, MOTIE. All work is supported by the Department of Energy under contract No. DE-AC36-08GO28308 to NREL.

## 2.7 References


1. Brown, P. R.; Kim, D.; Lunt, R. R.; Zhao, N.; Bawendi, M. G.; Grossman, J. C.; Bulovi, V. Energy Level Modification in Lead Sulfide Quantum Dot Thin Films through Ligand Exchange. *ACS Nano* **2014**, *8*, 5863–5872.

2. Goodwin, E. D.; Straus, D. B.; Gaulding, E. A.; Murray, C. B.; Kagan, C. R. The Effects of Inorganic Surface Treatments on Photogenerated Carrier Mobility and Lifetime in PbSe Quantum Dot Thin Films. *Chem. Phys.* **2015**, *471*, 32–36.

3. Klimov, V. I.; Baker, T. A.; Lim, J.; Velizhanin, K. A.; McDaniel, H. Quality Factor of Luminescent Solar Concentrators and Practical Concentration Limits Attainable with Semiconductor Quantum Dots. *ACS Photonics* **2016**, *3*, 1138–1148.

4. Ellingson, R. J.; Beard, M. C.; Johnson, J. C.; Yu, P.; Micic, O. I.; Nozik, A. J.; Shabaev, A.; Efros, A. L. Highly Efficient Multiple Exciton Generation in Colloidal PbSe and PbS Quantum Dots. *Nano Lett.* **2005**, *5*, 865–871.

5. Lee, D. C.; Robel, I.; Pietryga, J. M.; Klimov, V. I. Infrared-Active Heterostructured Nanocrystals with Ultralong Carrier Lifetimes. *J. Am. Chem. Soc.* **2010**, *132*, 9960–9962.

6. Cirloganu, C. M.; Padilha, L. a; Lin, Q.; Makarov, N. S.; Velizhanin, K. a; Luo, H.; Robel, I.; Pietryga, J. M.; Klimov, V. I. Enhanced Carrier Multiplication in Engineered Quasi-Type-II Quantum Dots. *Nat. Commun.* **2014**, *5*, 4148.

7. Brown, P. R.; Kim, D.; Lunt, R. R.; Zhao, N.; Bawendi, M. G.; Grossman, J. C.; Bulovic, V. Energy Level Modification in Lead Sulfide Quantum Dot Thin Films Through Ligand Exchange. *ACS Nano* **2014**, *8*, 5863–5872.

8. Supran, G. J.; Shirasaki, Y.; Song, K. W.; Caruge, J.-M.; Kazlas, P. T.; Coe-Sullivan, S.; Andrew, T. L.; Bawendi, M. G.; Bulović, V. QLEDs for Displays and Solid-State Lighting. *MRS Bull.* **2013**, *38*, 703–711.

9. Konstantatos, G.; Badioli, M.; Gaudreau, L.; Osmond, J.; Bernechea, M.; de Arquer, F. P. G.; Gatti, F.; Koppens, F. H. L. Hybrid graphene–Quantum Dot Phototransistors with Ultrahigh Gain. *Nat. Nanotechnol.* **2012**, *7*, 363–368.

10. Kim, S.; Lim, Y. T.; Soltesz, E. G.; De Grand, A. M.; Lee, J.; Nakayama, A.; Parker, J. A.; Mihaljevic, T.; Laurence, R. G.; Dor, D. M.; et al. Near-Infrared Fluorescent Type II Quantum Dots for Sentinel Lymph Node Mapping. *Nat. Biotechnol.* **2004**, *22*, 93–97.

11. Lan, X.; Voznyy, O.; García de Arquer, F. P.; Liu, M.; Xu, J.; Proppe, A. H.; Walters, G.; Fan, F.; Tan, H.; Liu, M.; et al. 10.6% Certified Colloidal Quantum Dot Solar Cells via Solvent-Polarity-Engineered Halide Passivation. *Nano Lett.* **2016**, *16*, 4630–4634.

12. Wang, H.; Pei, Y.; Lalonde, A. D.; Snyder, G. J. Heavily Doped P-Type PbSe with High Thermoelectric Performance: An Alternative for PbTe. *Adv. Mater.* **2011**, *23*, 1366–1370.

13. Supran, G. J.; Song, K. W.; Hwang, G. W.; Correa, R. E.; Scherer, J.; Dauler, E. a; Shirasaki, Y.; Bawendi, M. G.; Bulović, V. High-Performance Shortwave-Infrared Light-Emitting Devices Using Core–Shell (PbS–CdS) Colloidal Quantum Dots. *Adv. Mater.* **2015**, 1437–1442.

14. Mashford, B.; Stevenson, M.; Popovic, Z. High-Efficiency Quantum-Dot Light-Emitting Devices with Enhanced Charge Injection. *Nat. Photonics* **2013**, *7*, 407–412.

15. Hanna, M. C.; Nozik, a. J. Solar Conversion Efficiency of Photovoltaic and Photoelectrolysis Cells with Carrier Multiplication Absorbers. *J. Appl. Phys.* **2006**, *100*, 074510.

16. Semonin, O. E.; Luther, J. M.; Choi, S.; Chen, H.-Y.; Gao, J.; Nozik, a. J.; Beard, M. C. Peak External Photocurrent Quantum Efficiency Exceeding 100% via MEG in a Quantum Dot Solar Cell. *Science* **2011**, *334*, 1530–1533.

17. Davis, N. J. L. K.; Böhm, M. L.; Tabachnyk, M.; Wisnivesky-Rocca-Rivarola, F.; Jellicoe, T. C.; Ducati, C.; Ehrler, B.; Greenham, N. C. Multiple-Exciton Generation in Lead Selenide Nanorod Solar Cells with External Quantum Efficiencies Exceeding 120%. *Nat. Commun.* **2015**, *6*, 8259.

18. Böhm, M. L.; Jellicoe, T. C.; Tabachnyk, M.; Davis, N. J. L. K.; Wisnivesky Rocca Rivarola, F.; Ducati, C.; Ehrler, B.; Bakulin, A. a.; Greenham, N. C. Lead Telluride Quantum Dot Solar Cells Displaying External Quantum Efficiencies Exceeding 120%. *Nano Lett.* **2015**, *15*, 7987–7993.

19. Cunningham, P. D.; Boercker, J. E.; Foos, E. E.; Lumb, M. P.; Smith, A. R.; Tischler, J. G.; Melinger, J. S. Enhanced Multiple Exciton Generation in Quasi-One-Dimensional Semiconductors. *Nano Lett.* **2011**, *11*, 3476–3481.

20. Yang, Y.; Ostrowski, D. P.; France, R. M.; Zhu, K.; van de Lagemaat, J.; Luther, J. M.; Beard, M. C. Observation of a Hot-Phonon Bottleneck in Lead-Iodide Perovskites. *Nat. Photonics* **2016**, *10*, 53–59.

21. Du, J.; Du, Z.; Hu, J.-S.; Pan, Z.; Shen, Q.; Sun, J.; Long, D.; Dong, H.; Sun, L.; Zhong, X.; et al. Zn-Cu-In-Se Quantum Dot Solar Cells with a Certified Power Conversion Efficiency of 11.6. *J. Am. Chem. Soc.* **2016**, *138*, 4201–4209.

22. Zhang, J.; Chernomordik, B. D.; Crisp, R. W.; Kroupa, D. M.; Luther, J. M.; Miller, E. M.; Gao, J.; Beard, M. C. Preparation of Cd/Pb Chalcogenide Heterostructured Janus Particles via Controllable Cation Exchange. *ACS Nano* **2015**, *9*, 7151–7163.

23. Zhang, J.; Gao, J.; Church, C. P.; Miller, E. M.; Luther, J. M.; Klimov, V. I.; Beard, M. C. PbSe Quantum Dot Solar Cells with More than 6% Efficiency Fabricated in Ambient Atmosphere. *Nano Lett.* **2014**, *14*, 6010–6015.

24. Hu, Y.; Diao, X.; Wang, C.; Hao, W.; Wang, T. Effects of Heat Treatment on Properties of ITO Films Prepared by Rf Magnetron Sputtering. *Vacuum* **2004**, *75*, 183–188.

25. Church, C. P.; Muthuswamy, E.; Zhai, G.; Kauzlarich, S. M.; Carter, S. A. Quantum Dot Ge/TiO2 Heterojunction Photoconductor Fabrication and Performance. *Appl. Phys. Lett.* **2013**, *103*, 223506.

26. Gao, J.; Jeong, S.; Lin, F.; Erslev, P. T.; Semonin, O. E.; Luther, J. M.; Beard, M. C. Improvement in Carrier Transport Properties by Mild Thermal Annealing of PbS Quantum Dot Solar Cells. *Appl. Phys. Lett.* **2013**, *102*, 043506.

27. Emery, K. Measurement and Characterization of Solar Cells and Modules. In *Handbook of Photovoltaic Science and Engineering*; 2011; pp 797–840.

28. Snaith, H. J. How Should You Measure Your Excitonic Solar Cells? *Energy Environ. Sci.* **2012**, *5*, 6513–6520.

29. Law, M.; Beard, M. C.; Choi, S.; Luther, J. M.; Hanna, M. C.; Nozik, A. J. Determining the Internal Quantum Efficiency of PbSe Nanocrystal Solar Cells with the Aid of an Optical Model. *Nano Lett.* **2008**, *8*, 3904–3910.

30. Sites, J. R.; Tavakolian, H.; Sasala, R. A. Analysis of Apparent Quantum Efficiency. *Sol. Cells* **1990**, *29*, 39–48.

31. Hegedus, S. S.; Shafarman, W. N. Thin-Film Solar Cells: Device Measurements and Analysis. *Prog. Photovoltaics Res. Appl.* **2004**, *12*, 155–176.

32. Zhang, H.; Hyun, B. R.; Wise, F. W.; Robinson, R. D. A Generic Method for Rational Scalable Synthesis of Monodisperse Metal Sulfide Nanocrystals. *Nano Lett.* **2012**, *12*, 5856–5860.

33. Pu, C.; Zhou, J.; Lai, R.; Niu, Y.; Nan, W.; Peng, X. Highly Reactive, Flexible yet Green Se Precursor for Metal Selenide Nanocrystals: Se-Octadecene Suspension (Se-SUS). *Nano Res.* **2013**, *6*, 652–670.

34. Luther, J. M.; Law, M.; Beard, M. C.; Song, Q.; Reese, M. O.; Ellingson, R. J.; Nozik, A. J. Schottky Solar Cells Based on Colloidal Nanocrystal Films. *Nano Lett.* **2008**, *8*, 3488–3492.

35. NREL. Best Research-Cell Efficiencies http://www.nrel.gov/ncpv/images/efficiency_chart.jpg (accessed Jul 17, 2016).

36. Leschkies, K. S.; Beatty, T. J.; Kang, M. S.; Norris, D. J.; Aydil, E. S. Solar Cells Based on Junctions between Colloidal PbSe Nanocrystals and Thin ZnO Films. *ACS Nano* **2009**, *3*, 3638–3648.

37. Pattantyus-Abraham, A. G.; Kramer, I. J.; Barkhouse, A. R.; Wang, X.; Konstantatos, G.; Debnath, R.; Levina, L.; Raabe, I.; Nazeeruddin, M. K.; Grätzel, M.; et al. Depleted-Heterojunction Colloidal Quantum Dot Solar Cells. *ACS Nano* **2010**, *4*, 3374–3380.

38. Gao, J.; Luther, J. M.; Semonin, O. E.; Ellingson, R. J.; Nozik, A. J.; Beard, M. C. Quantum Dot Size Dependent J-V Characteristics in Heterojunction ZnO/PbS Quantum Dot Solar Cells. *Nano Lett.* **2011**, *11*, 1002–1008.

39. Gao, J.; Perkins, C. L.; Luther, J.; Hanna, M.; Chen, H.; Semonin, O.; Nozik, A.; Ellingson, R. J.; Beard, M. N-Type Transition Metal Oxide as a Hole Extraction Layer in PbS Quantum Dot Solar Cells. *Nano Lett.* **2011**, *11*, 3263–3266.

40. Semonin, O. E.; Luther, J. M.; Choi, S.; Chen, H.-Y.; Gao, J.; Nozik, a. J.; Beard, M. C. Peak External Photocurrent Quantum Efficiency Exceeding 100% via MEG in a Quantum Dot Solar Cell. *Science* **2011**, *334*, 1530–1533.

41. Chuang, C.-H. M.; Brown, P. R.; Bulović, V.; Bawendi, M. G. Improved Performance and Stability in Quantum Dot Solar Cells through Band Alignment Engineering. *Nat. Mater.* **2014**, *13*, 796–801.

42. Oh, S. J.; Berry, N. E.; Choi, J. H.; Gaulding, E. A.; Paik, T.; Hong, S. H.; Murray, C. B.; Kagan, C. R. Stoichiometric Control of Lead Chalcogenide Nanocrystal Solids to Enhance Their Electronic and Optoelectronic Device Performance. *ACS Nano* **2013**, *7*, 2413–2421.

43. Crisp, R. W.; Kroupa, D. M.; Marshall, A. R.; Miller, E. M.; Zhang, J.; Beard, M. C.; Luther, J. M. Metal Halide Solid-State Surface Treatment for High Efficiency PbS and PbSe QD Solar Cells. *Sci. Rep.* **2015**, *5*, 9945.

44. Marshall, A. R.; Young, M. R.; Nozik, A. J.; Beard, M. C.; Luther, J. M. Exploration of Metal Chloride Uptake for Improved Performance Characteristics of PbSe Quantum Dot Solar Cells. *J. Phys. Chem. Lett.* **2015**, *6*, 2892–2899.

45. Gao, J.; Johnson, J. C. Charge Trapping in Bright and Dark States of Coupled PbS Quantum Dot Films. *ACS Nano* **2012**, *6*, 3292–3303.

46. Tang, J.; Kemp, K. W.; Hoogland, S.; Jeong, K. S.; Liu, H.; Levina, L.; Furukawa, M.; Wang, X.; Debnath, R.; Cha, D.; et al. Colloidal-Quantum-Dot Photovoltaics Using Atomic-Ligand Passivation. *Nat. Mater.* **2011**, *10*, 765–771.

47. Ip, A. H.; Thon, S. M.; Hoogland, S.; Voznyy, O.; Zhitomirsky, D.; Debnath, R.; Levina, L.; Rollny, L. R.; Carey, G. H.; Fischer, A.; et al. Hybrid Passivated Colloidal Quantum Dot Solids. *Nat. Nanotechnol.* **2012**, *7*, 577–582.

48. Marshall, A. R.; Beard, M. C.; Johnson, J. C. Nongeminate Radiative Recombination of Free Charges in Cation-Exchanged PbS Quantum Dot Films. *Chem. Phys.* **2016**, *471*, 75–80.

49. Kim, S.; Marshall, A. R.; Kroupa, D. M.; Miller, E. M.; Luther, J. M.; Jeong, S.; Beard, M. C. Air-Stable and Efficient PbSe Quantum-Dot Solar Cells Based upon Quantum Dots. *ACS Nano* **2015**, *9*, 8157–8164.

50. Moreels, I.; Fritzinger, B.; Martins, J. C.; Hens, Z. Surface Chemistry of Colloidal PbSe Nanocrystals. *J. Am. Chem. Soc.* **2008**, *130*, 15081–15086.

51. Zhang, J.; Gao, J.; Miller, E. M.; Luther, J. M.; Beard, M. C. Diffusion-Controlled Synthesis of PbS and PbSe Quantum Dots with in Situ Halide Passivation for Quantum Dot Solar Cells. *ACS Nano* **2014**, *8*, 614–622.

52. Selinsky, R. S.; Ding, Q.; Faber, M. S.; Wright, J. C.; Jin, S. Quantum Dot Nanoscale Heterostructures for Solar Energy Conversion. *Chem. Soc. Rev.* **2013**, *42*, 2963–2985.

53. Sitt, A.; Hadar, I.; Banin, U. Band-Gap Engineering, Optoelectronic Properties and Applications of Colloidal Heterostructured Semiconductor Nanorods. *Nano Today* **2013**, *8*, 494–513.

54. Hanna, M. C.; Beard, M. C.; Nozik, A. J. Effect of Solar Concentration on the Thermodynamic Power Conversion Efficiency of Quantum-Dot Solar Cells Exhibiting Multiple Exciton Generation. *J. Phys. Chem. Lett.* **2012**, *3*, 2857–2862.

55. Schaller, R. D.; Klimov, V. I. High Efficiency Carrier Multiplication in PbSe Nanocrystals: Implications for Solar Energy Conversion. *Phys. Rev. Lett.* **2004**, *92*, 186601.

56. Nozik, A. J. Multiple Exciton Generation in Semiconductor Quantum Dots. *Chem. Phys. Lett.* **2008**, *457*, 3–11.

CHAPTER III

# Tandem Solar Cells From Solution-Processed CdTe and PbS Quantum Dots Using A ZnTe/ZnO Tunnel Junction

Adapted from:

Ryan W. Crisp, Gregory F. Pach, J. Matthew Kurley, Ryan M. France, Matthew O. Reese, Sanjini U. Nanayakkara, Bradley A. MacLeod, Dmitri V. Talapin, Matthew C. Beard, and Joseph M. Luther. "Tandem Solar Cells from Solution-Processed CdTe and PbS Quantum Dots Using a ZnTe–ZnO Tunnel Junction." *Nano Letters* **17** (2), 1020-1027 (2017).

## 3.1 Abstract

We developed a monolithic CdTe/PbS tandem solar cell architecture where both the CdTe and PbS absorber layers are solution-processed from nanocrystal inks. Due to their tunable nature, PbS quantum dots (QDs), with a controllable bandgap between 0.4 and ~1.6 eV, are a promising candidate for a bottom absorber layer in tandem photovoltaics. In the detailed balance limit, the ideal configuration of a CdTe ($E_g$ = 1.5 eV)/PbS tandem structure assumes infinite thickness of the absorber layers and requires the PbS bandgap to be 0.75 eV to theoretically achieve a power conversion efficiency (PCE) of 45%. However, modeling shows that by allowing the thickness of the CdTe layer to vary, a tandem with efficiency over 40% is achievable using bottom cell bandgaps ranging from 0.68 and 1.16 eV. In a first step towards developing this technology, we explore CdTe/PbS tandem devices by developing a ZnTe/ZnO tunnel junction, which appropriately combines the two subcells in series. We examine the basic characteristics of the solar cells as a function of layer thickness and bottom cell bandgap and

demonstrate open circuit voltages in excess of 1.1 V with matched short circuit current density of 10 mA/cm$^2$ in prototype devices.

### 3.2 Introduction

Since solar energy capture and conversion involves the coverage of large land areas, increasing efficiency while maintaining low manufacturing costs is key for continued cost reductions in solar cell technologies.[1] Multiple solar cell technologies with different spectral response connected in tandem present one pathway toward greatly enhancing the power conversion efficiencies (PCE) in photovoltaics. CdTe thin-film solar cells hold the greatest market share in photovoltaics next to Si and have recently exceeded multicrystalline Si in performance and costs.[2] While generally underexplored, combining CdTe in a tandem configuration could retain the low cost structure of CdTe devices; yet greatly improve the amount of power extracted from the panels. Likewise, the overall energy yield in certain tandem configurations with CdTe motivates the exploration of tandem possibilities.[3]

The detailed-balanced approach used by Shockley and Queisser (SQ) concludes that under common assumptions, the maximum achievable PCE of a single junction solar cell is 33%, but by combining multiple absorbers in tandem, PCEs of up to 45% could be achieved.[4] Figure 3.1a shows the standard detailed balance analysis for maximum performance in a monolithically connected tandem junction solar cell as a function of the bandgap ($E_g$) of the two subcells composing the tandem. In a typical detailed balance analysis of multi-junction solar cells the following conditions are assumed; (1) illumination from the AM1.5G solar spectrum; (2) that both cells absorb all photons above the $E_g$; and (3) that both are operating at the radiative limit. In the following we explore conditions that relax assumption 2 and 3.

In the 2-terminal series connected tandem configuration, depending on the chosen top cell, there is a specific corresponding bottom cell $E_g$ required to achieve optimal performance. However, as is shown in Figure 3.1b if we enable the thickness of the top cell to vary,[5] a controlled number of photons normally absorbed in the top cell could be transmitted to the bottom cell to aid in matching the current produced by each subcell since the overall current of the system is limited by the lowest producing subcell. Allowing the thickness of the top cell to vary facilitates the use of a wider range of $E_g$ combinations, which still achieve near-peak efficiency. Figure 3.1c, shows the analysis for a two-terminal, two-junction tandem solar cell with the top cell bandgap fixed ($E_g$ = 1.5 eV) for CdTe. The ability to tune the thickness of the CdTe shows a widening of the range of bottom cells that could be paired with CdTe to still achieve high efficiencies. For example, a low bandgap absorber ranging between 0.68 and 1.16 eV could achieve a PCE above 40%. This ability to tailor the thickness of the CdTe is critical to enable a bottom cell with bandgap above 0.8 eV (the infinite thickness limit is shown as the dashed trace).

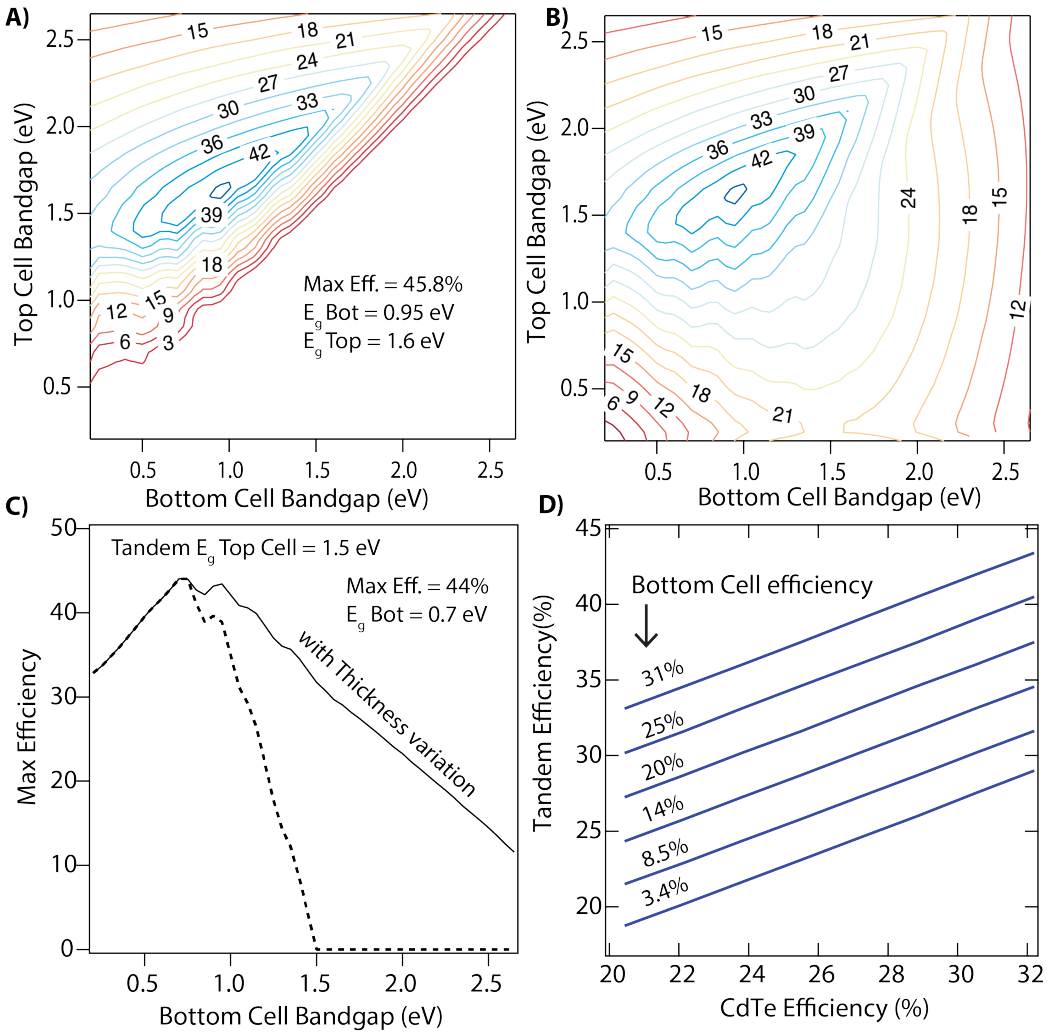


**Figure 3.1.** (a) Detailed balance efficiency limits for a dual-junction tandem solar cell assuming monolithic integration (i.e. two-terminal), AM1.5G spectrum, and that each cell absorbs all available photons with energy greater than the bandgap. (b) Same assumptions as in panel a) with the exception that the top cell thickness can be adjusted to permit some photons to be transmitted to the bottom cell. *Note: the thickness of the top cell for each optimized point in the contour may be different*. (c) Assuming the top cell has a bandgap of 1.5 eV (as does CdTe), the maximum efficiency of the tandem device is plotted as a function of the bottom cell bandgap under two conditions: infinite thickness approximation (dashed trace) and allowing the top cell thickness to vary (solid line). In both cases the most optimal condition yields a tandem cell with 44% efficiency with bottom cell bandgap of 0.7 eV. However, the solid trace shows near-optimal performance for a much wider range of bottom cell conditions. (d) Real world simulations of tandem cell efficiencies including non-radiative recombination losses. Lines show how the tandem cell efficiency would improve as a function of CdTe efficiency given a bottom cell efficiency with bandgap of 0.95 eV.

Next, in our simulations we take into consideration that the present-day CdTe system does not operate at the radiative limit[6] We include non-radiative recombination through the external radiative efficiency (ERE), defined by Rau[7] and tabulated by Green[8] for a variety of technologies. If the ERE is limited to $10^{-4}$% to reflect present-day CdTe technologies, then the maximum efficiency attainable by a single junction CdTe cell ($E_g$ = 1.5 eV) is 22% (as has been experimentally demonstrated)[9]. Pairing this quality of CdTe absorber with a 0.95 eV bottom cell that exhibits a single junction PCE of 14% (same ERE value as CdTe) could achieve a tandem cell efficiency of ~26%. We should note that in order to achieve higher efficiencies in these non-ideal cases where non-radiative recombination reduces the open circuit voltage the top cell must be thinned in order to utilize a bottom cell with a higher voltage but that is still current matched. Both top and bottom cell efficiencies will improve over time as the technologies mature. We show how the tandem cell efficiency varies with the CdTe efficiency and bottom cell efficiency ($E_{g,Bottom}$ = 0.95 eV) in Figure 3.1d. When the bottom cell has efficiency less than 9%, a tandem with CdTe of efficiency > 20% will not increase the overall efficiency. However, no matter how the efficiency of the CdTe subcell improves over time a tandem cell with a bottom cell efficiency of 14% would add about 4% absolute (22% CdTe to 26% tandem, an 18% relative improvement) to the overall cell efficiency. If the bottom cell efficiency also improves then this number grows from 4% to ~12% absolute improvement (40% relative improvement), for the ideal case the single CdTe cell efficiency is 32% and the tandem cell efficiency would be 44%.

Recent studies show the ability to process CdTe films using nanocrystal inks followed by low temperature sintering, and to date, these approaches have achieved PCEs of 12.3%.[10-13] One advantage of using nanocrystals is that smoother and much thinner, more transparent layers, which are better suited for tandem devices, can be easily deposited. Alternatively, physical vapor

deposition routes such as close-space sublimation or vapor transport deposition used in commercial CdTe solar cells typically produce thicker (~3-5 μm) layers with high roughness (~0.5 μm).[6] For example, solar cells fabricated using sintered CdTe nanocrystals have demonstrated efficiencies of 10% for film thicknesses on the order of only 300 nm.[14-15]

PbS quantum dots (QDs) present a unique and attractive option for use in multi-junction solar energy conversion architectures due to their easily tunable bandgap (by varying the average QD size) across a wide range of energies. Furthermore, QD layers can be deposited in ambient conditions using low-cost, solution-processing methods. Low bandgap Pb-chalcogenide QDs and other materials also offer the advantage of producing multiple excitons per absorbed high-energy photon in solar cells.[16-18] The multiple exciton generation (MEG) effect has been considered in a multijunction solar cell with the infinite thickness approximation but shows no real advantage,[19] however when considered in the context of a cell with tunable thickness of the front cell, MEG enables a PCE advantage of about 4% absolute.

Currently there is considerable interest in developing single-junction PbS QD solar cells and those efforts have resulted in a certified PCE as high as 11.3% to date with $E_g$ between 1.2 and 1.3 eV.[9, 20] However, there are only three studies that report PbS QDs as active layers in multijunction configurations. Two reports have shown tandem configurations where both absorber layers consist of PbS QDs but of different bandgaps (1.6 and 1.0 eV).[21-22] One challenge in achieving a functioning tandem is to appropriately recombine opposing charge carriers from the subcells at the connecting junction while still allowing the lower energy photons to pass to the bottom cell. This junction is conventionally referred to as a tunnel junction in III-V multijunctions, but also called a recombination layer more generally. Choi *et al.*[21] used a recombination layer scheme consisting of ZnO/Au/PEDOT:PSS (a conductive *p*-type polymer)

and found that Au nanocrystals placed between the PEDOT:PSS and ZnO layers enhances recombination of opposing charges. Wang *et al*.[22] employed what they termed as a graded recombination layer utilizing multiple sputtered metal oxide layers of varying compositions (ITO, Al-doped ZnO, and $TiO_2$) to demonstrate a PCE of up to 4.2%. In another approach, Kim *et al*.[23] paired a polymer bulk heterojunction using PTB7:$PC_{71}BM$ for the high bandgap absorber layer and used a recombination scheme of $MoO_x$/ZnO/PFN (the latter being a solution-deposited conjugated polyelectrolyte).

In our study, we seek to construct a monolithic CdTe/PbS QD tandem solar cell combining these two nanocrystal-based absorbers in series using CdTe as the top cell. We evaluate a variety of device structures for CdTe nanocrystal-based solar cells and adopted the structure that yields the highest $V_{OC}$ and had the optimal polarity configuration to match the PbS solar cells.[14, 24] We developed a recombination layer of ZnTe/ZnO and reliably obtain a $V_{OC}$ in excess of 1 V indicating proper addition of the $V_{OC}$ of the subcells with short-circuit current density ($J_{sc}$) of 10 mA/cm$^2$ with overall power conversion efficiency of 5%.

**3.3 Results**

PbS has a bulk bandgap of 0.41 eV, however well-controlled syntheses of QDs allow for a tunable bandgap from the bulk value up to ~1.6 eV. To explore the tunable bandgap nature of the bottom cell in a tandem architecture, we first synthesized QD samples of varying bandgap (absorption spectra shown in Figure 3.2a) following a previously reported procedure by Zhang *et al.*[25] We then fabricated single-junction PbS QD devices following Crisp *et al*.[26] and tested their performance with the incident illumination of AM1.5G filtered through CdTe films of varying thickness. This allows evaluation of the bottom cell in the configuration free from complications associated with building the full tandem structure.

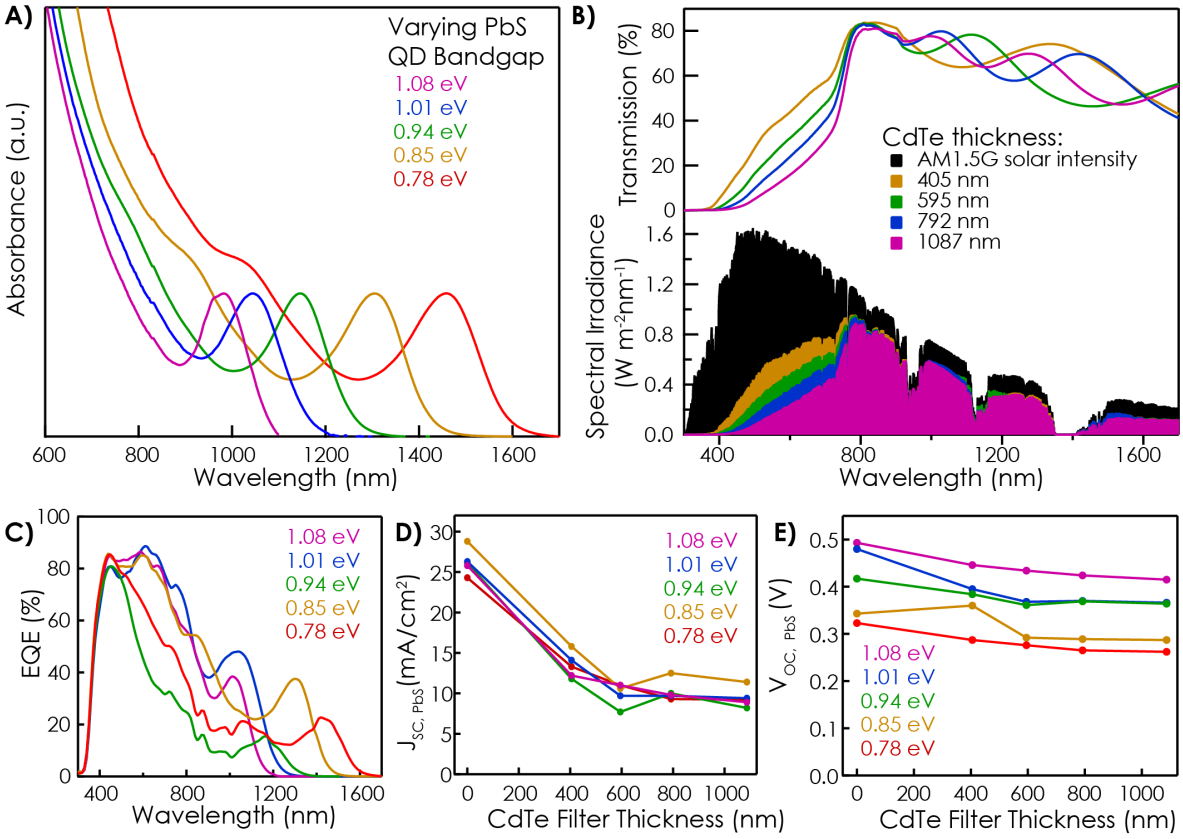


**Figure 3.2.** (a) Measured absorbance spectrum of PbS QDs with varying bandgap. (b) (Top) Transmission spectra of CdTe filters with CdTe layer thickness ranging from 405 nm to 1087 nm. (Bottom) Fraction of AM1.5 solar spectrum transmitted through CdTe-based optical filters. (c) External quantum efficiency measurements for PbS solar cells made with QDs shown in a). (d) Short-circuit current density and (e) open-circuit voltage of PbS QD solar cells with varying bandgap as a function of CdTe-filtered AM1.5G illumination.

A series of CdTe-based optical filters with film thickness varying between 400 and 1100 nm were prepared on ITO-coated glass following Jasieniak *et al.*[11] (see methods), and the transmission properties of the CdTe films are shown Figure 3.2b. The thickness of the CdTe film determines the amount of optical transmission in the spectral region between 400 and 800 nm light, and the transmission for all four CdTe films peaks just above 80% between 800 and 900 nm. Beyond 900 nm, optical interference and free carrier absorption in the transparent conductive layers begin to reduce the amount of transmitted light.

Reducing the bandgap of the bottom cell, in principle, allows more light absorption by that layer and thus ideally leads to better current-matching conditions. The increased current from a lower bandgap bottom cell must be evaluated with the fact that less voltage will be produced (and typically a lower fill factor). Studying the PbS QD cells with an illumination source filtered through CdTe films shows that the PbS cells with lower bandgaps yield only a minimal increase in photocurrent for all CdTe filter thicknesses (Figure 3.2d). We find that any loss in current suffered in using higher bandgap QDs is outweighed by the substantial gain in $V_{oc}$ (Figure 3.2e). Thus for optimized performance in this work we presently use PbS QDs with a bandgap of 1.0-1.1 eV. This finding is in agreement with analysis on CdTe tandems performed by Mailoa *et al.* which found that 0.73 eV GaSb did not provide as much benefit as 1 eV bottom cells of CIGS.[3]

Connecting the CdTe and PbS cells monolithically in series requires an appropriate interfacial carrier recombination layer as described above. For suitable carrier recombination to occur, the tandem subcells must have the same polarity of carrier extraction. Since the best performing PbS[26-27] and ink-based CdTe[14, 24] device architectures previously described have opposite polarities, it is necessary to invert the polarity of one of the structures for construction of a monolithic tandem. Figure 3.3 shows potential tandem structures for inverting either the CdTe (Figure 3.3a) or PbS (Figure 3.3b) polarity with electron and hole collectors denoted as cathode and anode, respectively.

Tandem devices of both architectures shown in Figure 3.3a-b were fabricated and cross-sectional scanning Kelvin probe microscopy (SKPM) was used to study the surface potential through each of the completed solar cells. Surface potential images can reveal how an applied bias is distributed among the layers of a solar cell as well as help visualize where resistive layers

and interfaces are located. Finished tandem devices were cleaved in order to expose the complete device for SKPM, and the cells were characterized under AM1.5G illumination before and after cleaving to ensure the cleaving process did not alter the cell performance. Figure 3.3c shows SKPM measurements on the cross-sections of both tandem architectures and the most prominent difference between the two measurements is observed in the vicinity of the recombination layer (shaded yellow). The tandem cell that consisted of ZnTe/ZnO as the recombination layer (top, Figure 3.3c) shows a smooth transition between the subcells with minimal voltage loss. This observation is consistent with a functioning recombination layer that acts as a tunneling junction between the top and bottom subcells. However, in the tandem cell that consisted of the ZnO/NiO as a recombination layer, there is a disruption between the two solar cells where a significant applied voltage is lost in the recombination layer, possibly due to the higher resistivity.

Based on initial device characterization and SKPM analysis, we find that the structure shown in Figure 3.3a offers more robust devices. Furthermore using ZnTe/ZnO has three immediate advantages: (1) process parameters and contacting CdTe with ZnTe is better understood,[28-29] (2) accordingly, processing and contacting ZnO and PbS is well understood,[30-32] and (3) using materials with the same metal cation prevents impurity diffusion (because the would-be-impurity is the same element) across the junction leading to a more abrupt interface. Anion diffusion is limited in such materials analogous to the rigidity of the anionic framework in metathesis reactions.[33-34] Further explorations in this report are therefore carried out using the inverted CdTe structure with a ZnTe/ZnO recombination layer (Figure 3.3a).

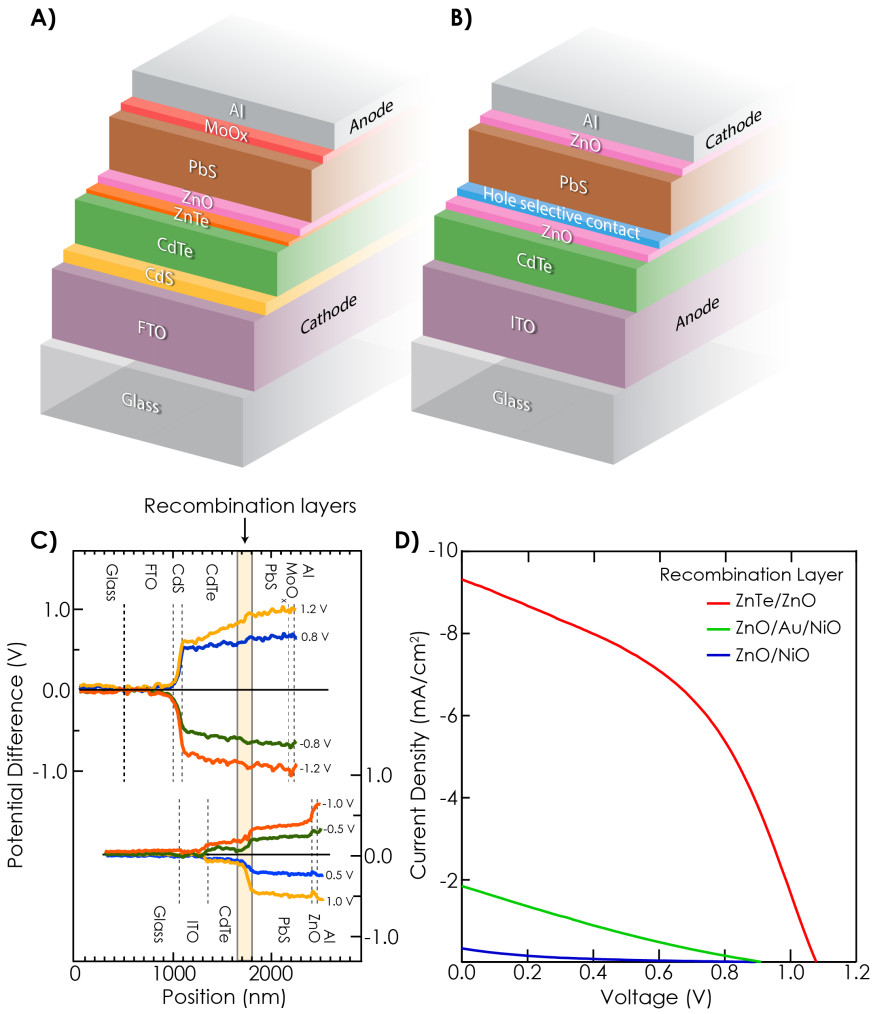


**Figure 3.3.** Device architecture schematics for tandem CdTe/PbS QD solar cells. Structure (a) uses the substrate TCO as the cathode and the top metal contact as the anode while structure (b) is the opposite. In structure a), the recombination layers are ZnTe and ZnO, while in structure b) a hole conducting or *p*-type material is required on top of the ZnO; in this work, we explored NiO. However as shown in (c), cross-sectional SKPM displays a large potential drop in the lower curves through the highlighted recombination layer indicating poor recombination of opposing charges. *Note: the devices have opposite polarity thus the forward (reverse) bias condition is plotted above (below) the abscissa.* Panel (d) shows *JV*-scans of the two structures along with structure b) with an added thin Au layer between ZnO and NiO to promote better recombination.

In order to explore the optimal current-matched condition between the CdTe and PbS layers, we modeled the optical properties of the device stack to determine photocurrent produced as a function of each absorber layer thickness. (As shown previously,[26] PbS devices thicker than about 700 nm suffer significant transport losses). For practical PbS QD thicknesses, we find

optimal current produced with the CdTe layer under 300 nm and the PbS QD film 500 nm. In order to test our model, devices were fabricated varying the thicknesses of both the CdTe and PbS subcells. Figure 3.4a shows *JV* curves under AM1.5G illumination for a series of tandem solar cells with varying thicknesses of CdTe (from 150 to 400 nm) with a constant PbS QD film thickness of 300 nm. In addition to the *JV*, we acquired external quantum efficiency (EQE) data for each device in this series (Figure 3.4b). The EQE for tandem devices is collected in two separate scans (see methods for details), which allows independent measurement of each subcell. As the CdTe thickness varies, the $J_{sc}$ is seen to vary between 7 and 8 mA/cm$^2$, however, the integration of the EQE shape against the solar spectrum (Figure 3.4b, and legend) shows that the PbS layer in each device limits the current. The EQE from the PbS QD cell, in general, decreases with thicker CdTe in the 400-800 nm range in line with the decreased transmittance and increased CdTe EQE. However, an important consequence related to the optical interference is heavily dependent on the CdTe thickness. The lowest energy exciton peak for the PbS QDs is around 1100 nm, but constructive interference patterns modulate the EQE signal between 850 and 1000 nm. The 250 nm thick CdTe film induces extra absorption in the PbS layer at 950 nm, enabling the highest $J_{sc}$ from the PbS subcell. We also find significant variation in the $V_{oc}$. The $V_{oc}$ of CdTe layers <200 nm thick is less consistent than the thicker films likely due to increased pinholes in the thin films. The highest $V_{oc}$ achieved was 1.18 V with a CdTe thickness of ~250 nm, which is also the CdTe thickness where the tandem cell was found to exhibit the best overall performance.

In order to determine whether current matching conditions could be enhanced, a series of devices was then constructed with increasing PbS QD film thicknesses from 300 nm to 500 nm (Figure 3.4c-d). With increasing PbS thickness, the tandem $J_{sc}$ increases as expected, yet in this

case there is little to no variation in the $V_{oc}$, which was 1.1 V for all cases. In Figure 3.4d, the EQE is displayed for a series of devices with 250 nm thick CdTe and varying PbS QD film thickness. In this series, the EQE of the CdTe is nearly identical for each device, as well as the EQE of the PbS between 400 nm and 700 nm. However between 700 nm and 1200 nm, the PbS EQE varies widely, again heavily influenced by optical interference, with 500 nm thick PbS generating the most total photocurrent of the series, yet still limiting the overall current of the cell.

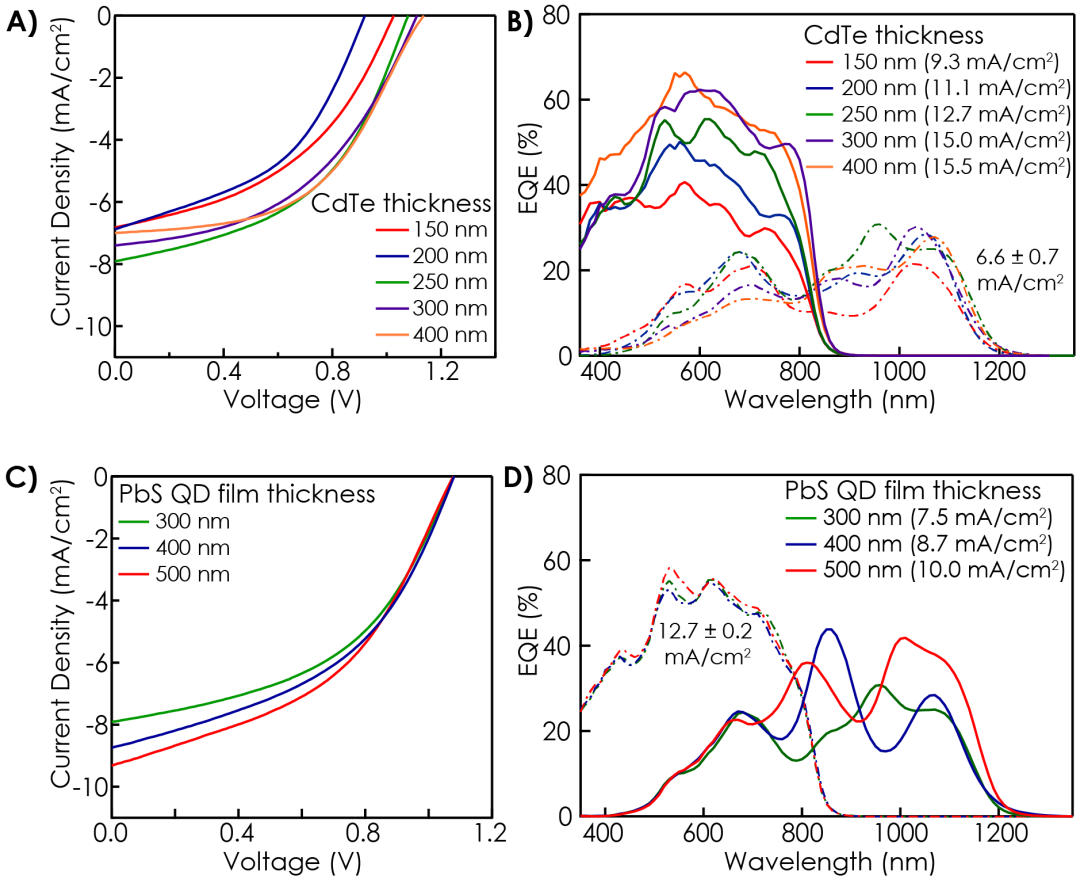


**Figure 3.4.** (a) JV plots of tandem devices with equal thicknesses of PbS (~300 nm) and varying amounts of CdTe. (b) EQE of devices shown in a). Solid lines represent the CdTe subcell EQE taken under 980 nm LED light bias while the dashed lines represent the corresponding PbS subcell EQE taken under 470 nm light bias. The integrated current density from each subcell is shown. (c) JV plots of tandem devices with equivalent CdTe thickness (~250 nm) and varying thicknesses of the PbS QD film. (d) EQE of devices shown in c). Solid lines represent the PbS subcell EQE while the dashed lines represent the corresponding CdTe subcell EQE. The integrated current density from the EQE is shown in the legend.

Figure 3.5 shows *JV* data as well as a colored cross-sectional SEM image of a PbS/CdTe tandem solar cell with ~250 nm CdTe layer and ~500 nm PbS layer. Figure 3.5a shows *JV* curves from PbS and CdTe single-junction devices as well as the monolithic tandem. The CdTe single-junction device is fabricated the same as the tandem device to the ZnTe layer and a 100 nm Au back contact is thermally evaporated. We find that the ZnTe/ZnO layers adequately sum the voltage of the subcells in this tandem configuration. In fact the voltage of the CdTe/PbS tandem is slightly higher than the sum of the control single junction devices.

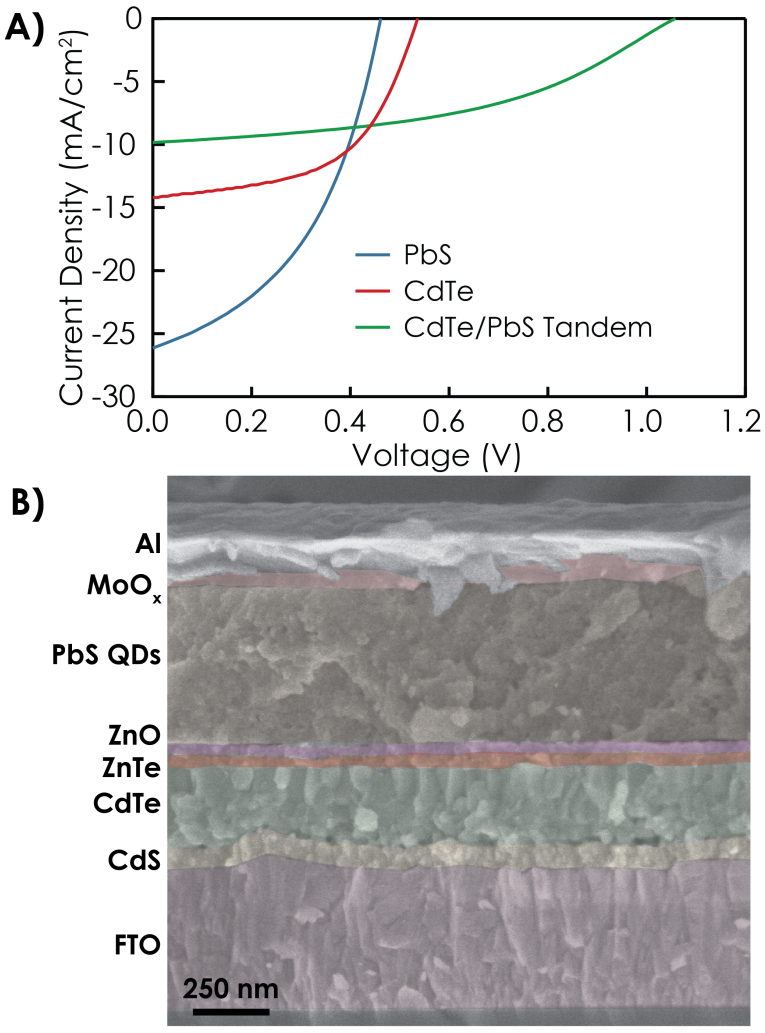


**Figure 3.5.** (a) JV measurements are shown for a PbS single junction device (blue), a CdTe single junction device (red), and the tandem device (green). (b) False-color cross section SEM image of the tandem solar cell.

### 3.5 Discussion and Conclusion

This work shows the potential to integrate multiple solution-processed photovoltaic materials to produce tandem devices with wide spectral response and large voltages. We explore the effects of tuning the thickness of the top cell in a tandem configuration, whereby thinner films of the top cell affect the range at which near optimal performance can be achieved. In the specific case explored here, we find that the ZnTe/ZnO layers adequately sum the voltage of ink-based CdTe and PbS QD subcells in a tandem configuration. The tandem modeling presented accounts for realistic non-radiative recombination processes in solar absorbers. We show that with present day quality of CdTe, a PbS QD bottom cell ($E_g$ = 0.95) with overall efficiency greater than 9% can add substantial efficiency gains to the tandem. This work thus highlights the need for continual advancement on the device structures and contact layers used in future generation PV technologies and shows the potential to develop efficient, lightweight and low cost solar cells.

### 3.5 Acknowledgements

The authors thank Bobby To for SEM imaging, Al Hicks for aid with graphics, and Reuben Collins and Ashley Marshall for valuable discussions. The solution processed CdTe technology and recombination layers were supported by the Department of Energy (DOE) SunShot program under Award Number DE-EE0005312. The PbS QD devices, characterization and modeling were supported by the Center for Advanced Solar Photophysics, an Energy Frontier Research Center funded by the U.S. Department of Energy, Office of Science, Office of Basic Energy Sciences. J.M.K. and D.V.T. also acknowledge the Department of Defense (DOD) Office of Naval Research under grant number N00014-13-1-0490, and by II-VI Foundation. G.F.P. and M.C.B. acknowledge support from Global R&D program (1415134409) funded by KIAT,

MOTIE. The work used facilities supported by the NSF MRSEC Program under Award No. DMR-14-20703.

### 3.6 References

1. Beard, M. C.; Luther, J. M.; Nozik, A. J., The promise and challenge of nanostructured solar cells. *Nature nanotechnology* **2014,** *9* (12), 951-954.

2. Green, M. A., Commercial progress and challenges for photovoltaics. *Nature Energy* **2016,** *1*, 15015.

3. Mailoa, J. P.; Lee, M.; Peters, I. M.; Buonassisi, T.; Panchula, A.; Weiss, D. N., Energy-yield prediction for II–VI-based thin-film tandem solar cells. *Energy & Environmental Science* **2016,** *9* (8), 2644-2653.

4. Semonin, O. E.; Luther, J. M.; Beard, M. C., Quantum dots for next-generation photovoltaics. *Materials Today* **2012,** *15* (11), 508-515.

5. Kurtz, S. R.; Faine, P.; Olson, J., Modeling of two‐junction, series‐connected tandem solar cells using top‐cell thickness as an adjustable parameter. *Journal of Applied Physics* **1990,** *68* (4), 1890-1895.

6. Burst, J. M.; Duenow, J. N.; Albin, D. S.; Colegrove, E.; Reese, M. O.; Aguiar, J. A.; Jiang, C.-S.; Patel, M.; Al-Jassim, M. M.; Kuciauskas, D., CdTe solar cells with open-circuit voltage breaking the 1 V barrier. *Nature Energy* **2016,** *1*, 16015.

7. Rau, U., Reciprocity relation between photovoltaic quantum efficiency and electroluminescent emission of solar cells. *Physical Review B* **2007,** *76* (8), 085303.

8. Green, M. A., Radiative efficiency of state-of-the-art photovoltaic cells. *Progress in Photovoltaics: Research and Applications* **2012,** *20* (4), 472-476.

9. Buffat, P.; Borel, J. P., Size effect on the melting temperature of gold particles. *Physical Review A* **1976,** *13* (6), 2287-2298.

10. Panthani, M. G.; Kurley, J. M.; Crisp, R. W.; Dietz, T. C.; Ezzyat, T.; Luther, J. M.; Talapin, D. V., High Efficiency Solution Processed Sintered CdTe Nanocrystal Solar Cells: The Role of Interfaces. *Nano Letters* **2014,** *14* (2), 670-675.

11. Jasieniak, J.; MacDonald, B. I.; Watkins, S. E.; Mulvaney, P., Solution-Processed Sintered Nanocrystal Solar Cells via Layer-by-Layer Assembly. *Nano Letters* **2011,** *11* (7), 2856-2864.

12. Gur, I.; Fromer, N. A.; Geier, M. L.; Alivisatos, A. P., Air-Stable All-Inorganic Nanocrystal Solar Cells Processed from Solution. *Science* **2005,** *310* (5747), 462-465.

13. Xue, H.; Wu, R.; Xie, Y.; Tan, Q.; Qin, D.; Wu, H.; Huang, W., Recent Progress on Solution-Processed CdTe Nanocrystals Solar Cells. *Applied Sciences* **2016,** *6* (7), 197.

14. Crisp, R. W.; Panthani, M. G.; Rance, W. L.; Duenow, J. N.; Parilla, P. A.; Callahan, R.; Dabney, M. S.; Berry, J. J.; Talapin, D. V.; Luther, J. M., Nanocrystal Grain Growth and Device Architectures for High-Efficiency CdTe Ink-Based Photovoltaics. *ACS Nano* **2014,** *8* (9), 9063-9072.

15. Zhang, H.; Kurley, J. M.; Russell, J. C.; Jang, J.; Talapin, D. V., Solution-Processed, Ultrathin Solar Cells from CdCl3--capped CdTe Nanocrystals: The Multiple Roles of CdCl3-Ligands. *Journal of the American Chemical Society* **2016**.

16. Böhm, M. L.; Jellicoe, T. C.; Tabachnyk, M.; Davis, N. J. L. K.; Wisnivesky-Rocca-Rivarola, F.; Ducati, C.; Ehrler, B.; Bakulin, A. A.; Greenham, N. C., Lead Telluride Quantum Dot Solar Cells Displaying External Quantum Efficiencies Exceeding 120%. *Nano Letters* **2015,** *15* (12), 7987-7993.

17. Davis, N. J. L. K.; Böhm, M. L.; Tabachnyk, M.; Wisnivesky-Rocca-Rivarola, F.; Jellicoe, T. C.; Ducati, C.; Ehrler, B.; Greenham, N. C., Multiple-exciton generation in lead selenide nanorod solar cells with external quantum efficiencies exceeding 120%. *Nature Communications* **2015,** *6*, 8259.

18. Semonin, O. E.; Luther, J. M.; Choi, S.; Chen, H.-Y.; Gao, J.; Nozik, A. J.; Beard, M. C., Peak External Photocurrent Quantum Efficiency Exceeding 100% via MEG in a Quantum Dot Solar Cell. *Science* **2011,** *334* (6062), 1530-1533.

19. Hanna, M.; Nozik, A., Solar conversion efficiency of photovoltaic and photoelectrolysis cells with carrier multiplication absorbers. *Journal of Applied Physics* **2006,** *100* (7), 074510.

20. Liu, M.; de Arquer, F. P. G.; Li, Y.; Lan, X.; Kim, G.-H.; Voznyy, O.; Jagadamma, L. K.; Abbas, A. S.; Hoogland, S.; Lu, Z.; Kim, J. Y.; Amassian, A.; Sargent, E. H., Double-Sided Junctions Enable High-Performance Colloidal-Quantum-Dot Photovoltaics. *Advanced Materials* **2016,** *28* (21), 4142-4148.

21. Choi, J. J.; Wenger, W. N.; Hoffman, R. S.; Lim, Y.-F.; Luria, J.; Jasieniak, J.; Marohn, J. A.; Hanrath, T., Solution-Processed Nanocrystal Quantum Dot Tandem Solar Cells. *Advanced Materials* **2011,** *23* (28), 3144-3148.

22. Wang, X.; Koleilat, G. I.; Tang, J.; Liu, H.; Kramer, I. J.; Debnath, R.; Brzozowski, L.; Barkhouse, D. A. R.; Levina, L.; Hoogland, S.; Sargent, E. H., Tandem colloidal quantum dot solar cells employing a graded recombination layer. *Nature Photonics* **2011,** *5* (8), 480-484.

23. Kim, T.; Gao, Y.; Hu, H.; Yan, B.; Ning, Z.; Jagadamma, L. K.; Zhao, K.; Kirmani, A. R.; Eid, J.; Adachi, M. M.; Sargent, E. H.; Beaujuge, P. M.; Amassian, A., Hybrid tandem solar cells with depleted-heterojunction quantum dot and polymer bulk heterojunction subcells. *Nano Energy* **2015,** *17*, 196-205.

24. Panthani, M. G.; Kurley, J. M.; Crisp, R. W.; Dietz, T. C.; Ezzyat, T.; Luther, J. M.; Talapin, D. V., High Efficiency Solution Processed Sintered CdTe Nanocrystal Solar Cells: The Role of Interfaces. *Nano Letters* **2013,** *14* (2), 670-675.

25. Zhang, J.; Gao, J.; Church, C. P.; Miller, E. M.; Luther, J. M.; Klimov, V. I.; Beard, M. C., PbSe Quantum Dot Solar Cells with More than 6% Efficiency Fabricated in Ambient Atmosphere. *Nano Letters* **2014,** *14* (10), 6010-6015.

26. Crisp, R. W.; Kroupa, D. M.; Marshall, A. R.; Miller, E. M.; Zhang, J.; Beard, M. C.; Luther, J. M., Metal Halide Solid-State Surface Treatment for High Efficiency PbS and PbSe QD Solar Cells. *Scientific reports* **2015,** *5*, 9945.

27. Lan, X.; Voznyy, O.; García de Arquer, F. P.; Liu, M.; Xu, J.; Proppe, A. H.; Walters, G.; Fan, F.; Tan, H.; Liu, M.; Yang, Z.; Hoogland, S.; Sargent, E. H., 10.6% Certified Colloidal Quantum Dot Solar Cells via Solvent-Polarity-Engineered Halide Passivation. *Nano Letters* **2016,** *16* (7), 4630-4634.

28. Rance, W. L.; Burst, J. M.; Meysing, D. M.; Wolden, C. A.; Reese, M. O.; Gessert, T. A.; Metzger, W. K.; Garner, S.; Cimo, P.; Barnes, T. M., 14%-efficient flexible CdTe solar cells on ultra-thin glass substrates. *Applied Physics Letters* **2014,** *104* (14), 143903.

29. Li, J.; Diercks, D. R.; Ohno, T. R.; Warren, C. W.; Lonergan, M. C.; Beach, J. D.; Wolden, C. A., Controlled activation of ZnTe:Cu contacted CdTe solar cells using rapid thermal processing. *Solar Energy Materials and Solar Cells* **2015,** *133*, 208-215.

30. Hoye, R. L. Z.; Ehrler, B.; Böhm, M. L.; Muñoz-Rojas, D.; Altamimi, R. M.; Alyamani, A. Y.; Vaynzof, Y.; Sadhanala, A.; Ercolano, G.; Greenham, N. C.; Friend, R. H.; MacManus-Driscoll, J. L.; Musselman, K. P., Improved Open- Circuit Voltage in ZnO–PbSe Quantum Dot Solar Cells by Understanding and Reducing Losses Arising from the ZnO Conduction Band Tail. *Advanced Energy Materials* **2014,** *4* (8).

31. Luther, J. M.; Gao, J.; Lloyd, M. T.; Semonin, O. E.; Beard, M. C.; Nozik, A. J., Stability Assessment on a 3% Bilayer PbS/ZnO Quantum Dot Heterojunction Solar Cell. *Advanced Materials* **2010,** *22* (33), 3704-3707.

32. Leschkies, K. S.; Beatty, T. J.; Kang, M. S.; Norris, D. J.; Aydil, E. S., Solar Cells Based on Junctions between Colloidal PbSe Nanocrystals and Thin ZnO Films. *ACS Nano* **2009,** *3* (11), 3638-3648.

33. Zhang, J.; Chernomordik, B. D.; Crisp, R. W.; Kroupa, D. M.; Luther, J. M.; Miller, E. M.; Gao, J.; Beard, M. C., Preparation of Cd/Pb Chalcogenide Heterostructured Janus Particles via Controllable Cation Exchange. *ACS Nano* **2015,** *9* (7), 7151-63.

34. De Trizio, L.; Manna, L., Forging Colloidal Nanostructures via Cation Exchange Reactions. *Chemical Reviews* **2016**.

CHAPTER IV

# Photoluminescent Properties of Janus-Like PbS/CdS Heterostructures Used For Enhanced Multiple Exciton Generation

## 4.1 Abstract

PbS/CdS heterostructured nanocrystals (NCs) are synthesized via cation exchange reaction of CdS quantum dots to produce quasi-spherical NCs containing two distinct domains of PbS and CdS. These structures are termed "Janus particles" since the PbS and CdS domains form on separate sides of the NC as opposed to a core/shell or other architectures. PbS/CdS heterostructures suspended in solution are analyzed using transient absorption spectroscopy and show exciton-to-photon quantum yields above unity at near $2E_g$ in samples with 50:50 Pb:Cd ratios determined by X-ray fluorescence. The exotic photoluminescent behavior of these Janus-like samples is also studied in order to develop a relative energy band structure between the two distinct crystalline domains in the NCs, which we propose as a type-I alignment. Furthermore, time-resolved photoluminescence studies reveal a slowed cooling mechanism in Janus-like heterostructures that can be linked to the enhanced MEG rate observed spectroscopically. As a proof of principle, Janus-like NCs are used as the active absorber layer in solar cells and demonstrate efficiencies of 2.1%.

## 4.2 Introduction

Quantum dot solar cells have the potential to surpass the standard Shockley-Queisser limit for single junction solar cells via multiple exciton generation (MEG), in which multiple electron-hole pairs are produced from a single high-energy photon.[1] Often described as an inverse Auger effect, MEG occurs when a hot exciton relaxes to the band edge by transferring its energy into the generation of another electron-hole pair. Quantum dots (QDs) are more likely to facilitate MEG than bulk semiconductors due to an increased separation of energy levels within the band structure induced by quantum confinement. This means that hot, photogenerated carriers are forced to scatter a greater number of phonons simultaneously in order to relax to the band edge. Due to the discretization of energy states in QDs, phonon emission occurs at a much slower rate than in bulk materials leading to longer hot carrier lifetimes—an effect deemed the "phonon bottleneck".[1-2] The cooling rate of photogenerated carriers in a given material directly relates to the MEG efficiency in that the MEG rate and cooling rate via phonon emission are in direct competition with one another.[3] Therefore, extending hot carrier lifetimes is a potential route toward enhancing MEG within quantum dot devices.

Currently, quantum dot solar cell efficiencies have been certified at 13.4%, yet top-performing quantum dot devices are not optimized to take advantage of MEG.[4-5] Still, studies have demonstrated external quantum efficiencies greater than 100% in quantum dot solar cells, which is attributed to MEG.[6-7] To present day, MEG studies have been carried out on a variety of systems[8-15] but many only exhibit MEG quantum yields (defined as the ratio of the number of excitons produced to incident photons) above unity at photon energies above the thermodynamic limit of $2E_g$. Recently, studies involving heterostructured nanocrystals (NCs) have shown promise for enhanced MEG.[16-17] Eshet *et al.* showed that a built-in field resulting from the band

offset in heterostructured type-II nanorods could provide a mechanism for enhanced MEG, while Cirloganu *et al.* used "wavefunction engineering" in PbSe/CdSe core/shell QDs to show MEG quantum yields above unity at energies of 1.94 – 2.18$E_g$. In this work we seek to expand upon a prior study detailing the synthesis of PbS/CdS heterostructured NCs called "Janus particles".[18] Using transient absorption spectroscopy we show MEG quantum yields above unity very near 2$E_g$ and through steady-state and time-resolved photoluminescence measurements we seek to explain a mechanism for the observed enhanced MEG in these Janus-like NCs.

**4.3 Results and Discussion**

Janus-like PbS/CdS heterostructured NCs are synthesized following a similar cation exchange procedure described in Chapter II in which $Cd^{2+}$ in CdS quantum dots is exchanged for $Pb^{2+}$ using $PbCl_2$ in oleylamine.[18-20] By controlling the reaction temperature, molar ratio of Pb and Cd precursors, and the length of reaction, NCs can be synthesized with differing extents of cation exchange as well as varying degrees of quantum confinement in both PbS and CdS domains. The resulting NCs are capped with Pb and Cd-oleate species affording them colloidal stability in a variety of nonpolar solvents. Figure 4.1a shows absorption spectra for precursor CdS quantum dots (yellow trace) and two separate syntheses of Janus-like PbS/CdS heterostructures with differing PbS:CdS ratios (green and red traces). Both Janus-like samples are compared to complete exchange PbS QDs (black trace) synthesized using the same reaction procedures. As the Pb-to-Cd ratio decreases in Janus-like NCs, the excitonic feature in the near-infrared (NIR) corresponding to absorption in the PbS-domain is seen to wash out. In both Janus-like NC samples, a sharp kink in the absorption profile is observed at ~500 nm corresponding to the CdS absorption onset. This feature is noticeably more distinct in the 20:80 Pb:CdS Janus sample.

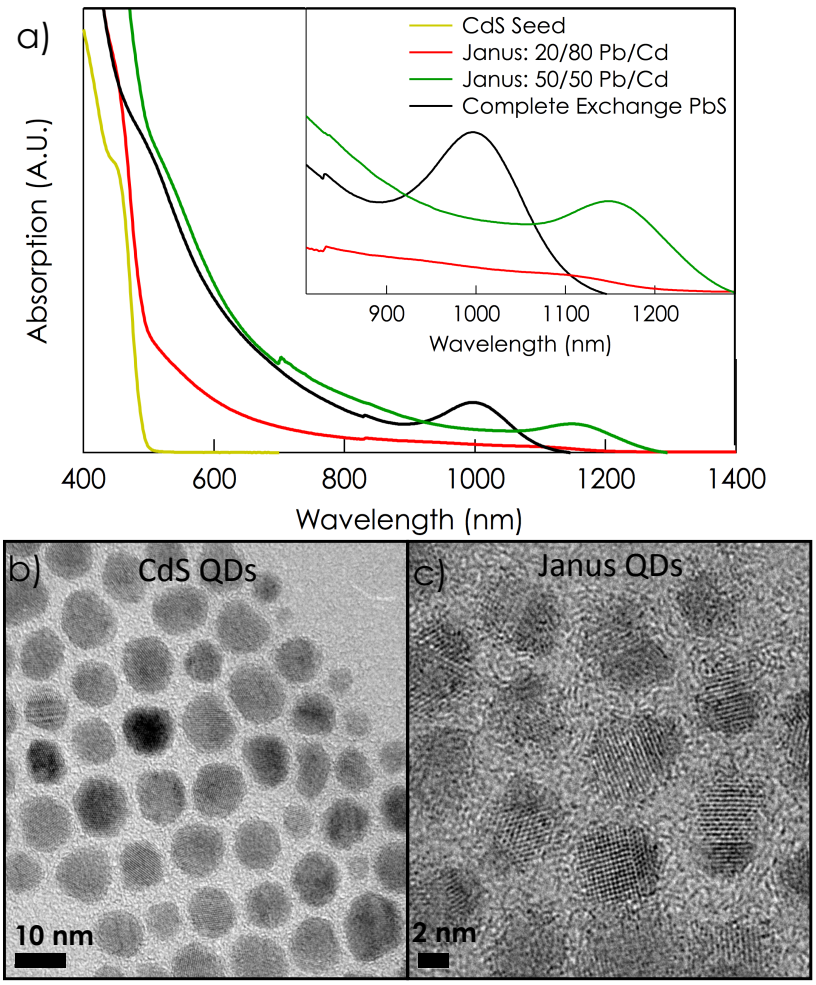


**Figure 4.1.** (a) Absorption spectra shown for CdS quantum dot precursor (yellow), 20:80 PbS:CdS Janus-like NCs, 50:50 PbS:CdS Janus-like nanoparticles, and completely exchanged PbS quantum dots (black). TEM images are shown of (b) precursor CdS quantum dots and (c) 50:50 PbS:CdS Janus-like nanocrystals.

Janus-like NCs are compositionally analyzed to determine PbS:CdS ratios using a combination of X-ray fluorescence (XRF), X-ray diffraction (XRD), and transmission electron microscopy (TEM). Figure 4.1b-c shows a TEM image of precursor CdS quantum dots and resulting PbS/CdS heterostructures. CdS QDs with a diameter of ~10 nm are used to produce quasi-spherical Janus-like NCs of ~5 nm in diameter indicating that CdS QDs disassemble during the exchange reaction. Additionally, a sharp interface can be observed at the lattice boundary in Janus-like NCs signifying two distinct pure-phase regions of PbS and CdS.

Transient absorption spectroscopy was used to examine MEG in PbS/CdS heterostructures by observing the interband bleach that arises upon photoexcitation and its subsequent decay. The bleach decay is mediated by a fast biexciton decay as well as a slower single exciton decay. By controlling the pump fluence in TA measurements, biexciton excitations can be eliminated by ensuring at most a single photon is absorbed per NC. We analyzed a variety of Janus-like NC composition ratios and found that 50:50 PbS:CdS heterostructures show the sharpest turn-on at $2E_g$. Figure 4.2 shows MEG QY of 50:50 PbS:CdS Janus-like NCs compared to other NCs from literature.[13, 17]

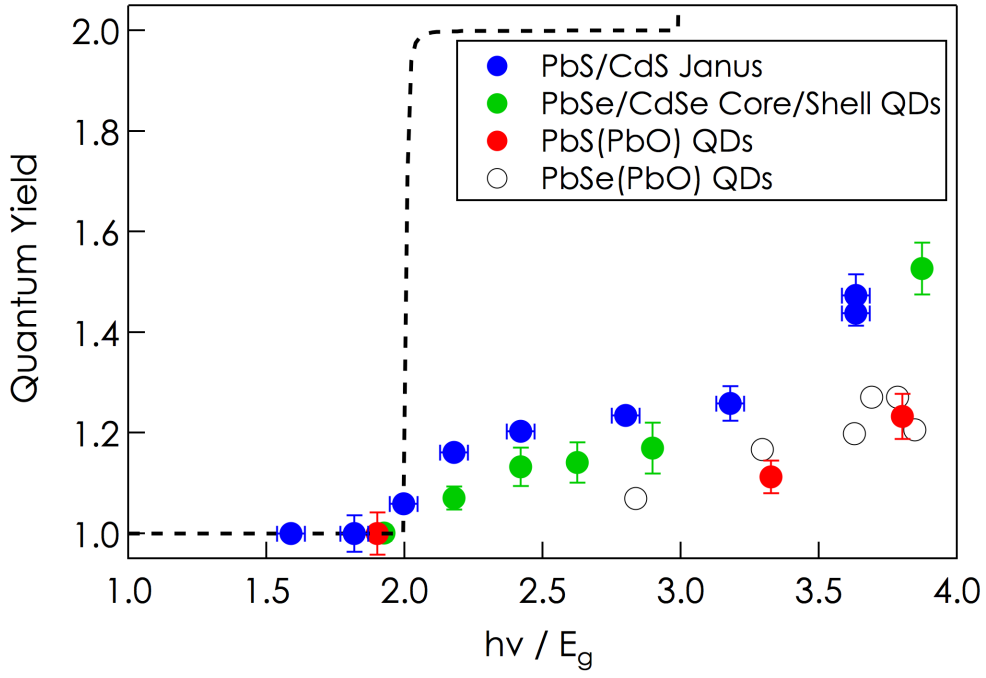


**Figure 4.2.** MEG quantum yield (QY) is plotted as a function of photon energy scaled by band gap energy for various nanostructures. PbS, PbSe and PbSe/CdSe core/shell QD QYs are all plotted from literature[13, 17] while 50:50 PbS:CdS Janus MEG QYs were determined by transient absorption spectroscopy.

Due to their anisotropic nature, Janus-like heterostructures exhibit two distinct photoluminescence (PL) spectra at visible and NIR energies corresponding to both the CdS and PbS domains, respectively. Figure 4.3 shows the absorption profile for CdS QD seeds, 50:50

PbS:CdS Janus-like NCs, and complete exchange PbS QDs as well as their respective normalized PL spectra. CdS QDs show a sharp PL peak attributed to band edge emission as well as a broader emission profile at lower energies corresponding to prevalent trap-state emission. This trap-mediated emission observed in CdS QDs has been well characterized and documented in previous literature.[21-22] Janus-like NCs display a similar broad visible PL spectrum as pure-phase CdS QDs indicating CdS trap-state emission is still a prevalent radiative recombination pathway, yet, they do not exhibit the same sharp emission profile that can be assigned to CdS band-to-band recombination. Janus-like NCs also display PL at NIR energies that can be attributed to band-to-band recombination in the PbS domain.

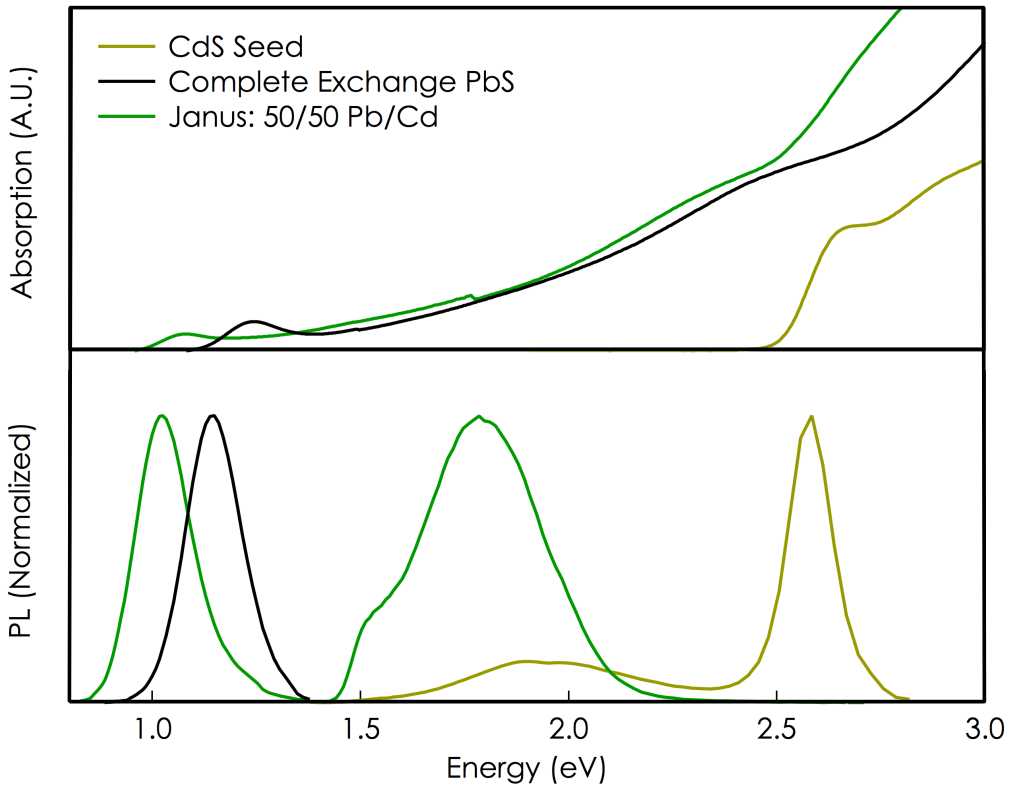


**Figure 4.3.** (top) Absorption spectra of seed CdS QDs (yellow), a 50/50 Pb/Cd Janus sample (green), and complete exchange PbS QDs (black). (bottom) Normalized photoluminescence spectra of the same samples.

Furthermore, the PL spectrum of Janus-like 50:50 PbS:CdS NCs display an excitation energy-dependent profile that changes if the excitation energy is above or below the CdS band gap. Figure 4.4a shows the PL profile of the visible emission from Janus-like NCs when excited above and below the CdS-domain band gap of ~2.58 eV (480 nm). When both the PbS and CdS domains of the heterostructured NCs are excited, the visible PL spectrum shows a broad emission profile, which, as previously described, can be attributed to the extended trap state manifold in CdS, yet a distinct shoulder is present at lower energy. When the same sample is excited at energy below the CdS-domain band gap, visible emission is still present, however the relative peak-to-shoulder intensity has changed. Additionally, the main PL peak is red-shifted while the shoulder position remains constant. It should be noted that Figure 4.4a shows PL spectra in which the peak intensities are normalized to one another. When the excitation energy is below the CdS-domain band gap, the overall PL intensity decreases significantly (Appendix A).

The fact that Janus-like NCs still display visible PL at excitation energies below the CdS band gap represents a strong interaction between the PbS and CdS domains in the NC. The extended trap state manifold in the CdS domain could provide a radiative cooling pathway for hot holes generated within the PbS domain. Figure 4.4c shows a similar phenomenon occurring with the IR PL spectrum as the emission profile begins to extend further into higher energies when both domains of Janus-like NCs are excited.

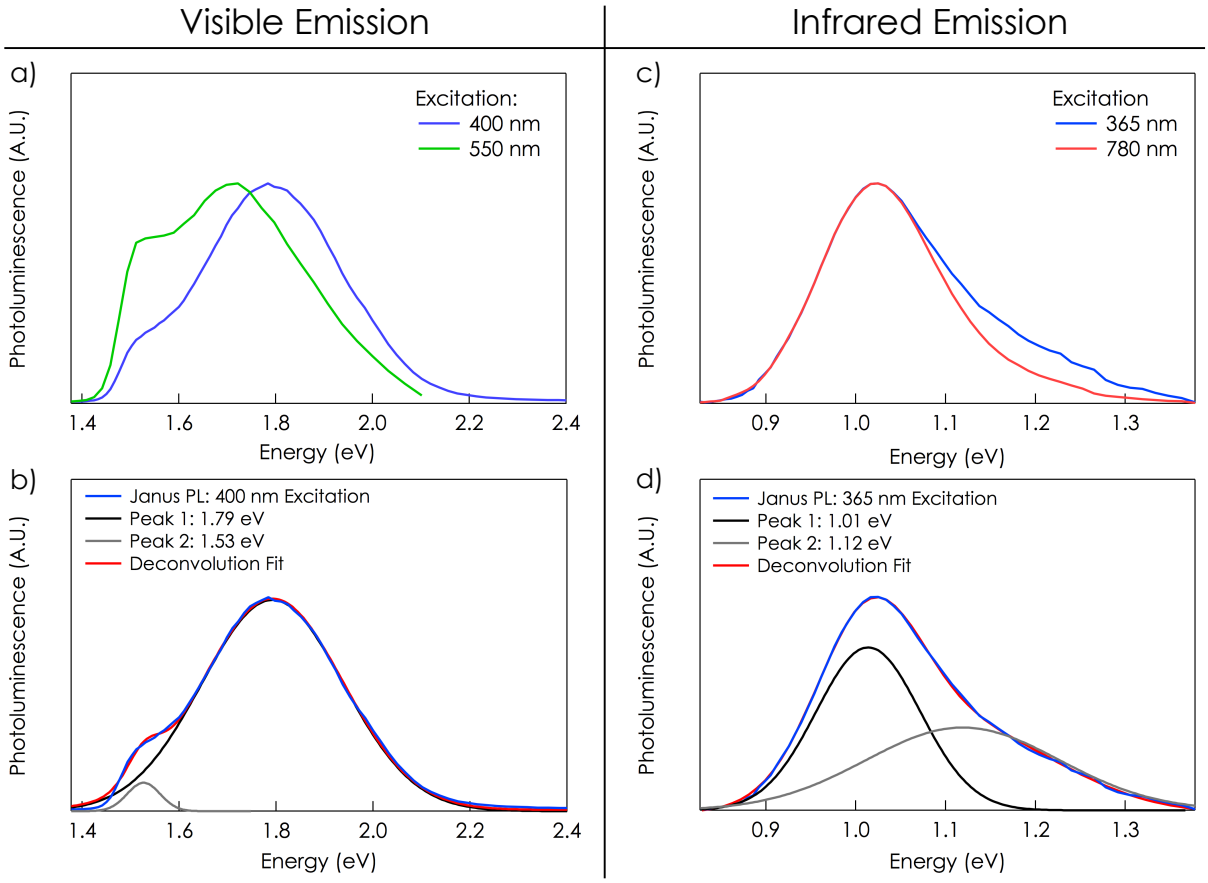


**Figure 4.4.** (a) Normalized visible PL spectra of a 50:50 PbS:CdS Janus-like sample excited at 400 nm (above the CdS band gap) and at 550 nm (below the CdS band gap). (b) Gaussian deconvolution of the PL spectrum shown in (a) with 400 nm excitation. (c) Normalized infrared PL spectra of the same 50:50 PbS:CdS Janus-like sample excited at 365 nm (above the CdS band gap) and at 780 nm (below the CdS band gap). (d) Gaussian deconvolution of the PL spectrum shown in (c) with 365 nm excitation.

In order to further explore this behavior, the PL profiles of both the visible and NIR emission were deconvoluted to reveal four Gaussian profiles representing four distinct radiative recombination pathways. These four deconvoluted profiles have peaks at 1.01 eV, 1.12 eV, 1.53 eV, and 1.79 eV. The highest and lowest energy peaks represent trap state emission from the CdS and band-edge emission from the PbS, respectively, while the two middle energy peaks are attributed to cross-band emission. Using these PL profiles, the relative band alignment between the PbS and CdS domains in Janus-like NCs can be determined and is shown in Figure 4.5 as a

type-I alignment. A type-I alignment between the two domains is further supported through TA studies previously discussed. When only the PbS is excited using low energy pump wavelengths, an interband bleach corresponding to the CdS is not observed. A type-II alignment would give photogenerated electrons in the PbS an energetically favorable cooling pathway into the CdS conduction band, however this transition is not spectroscopically observed.

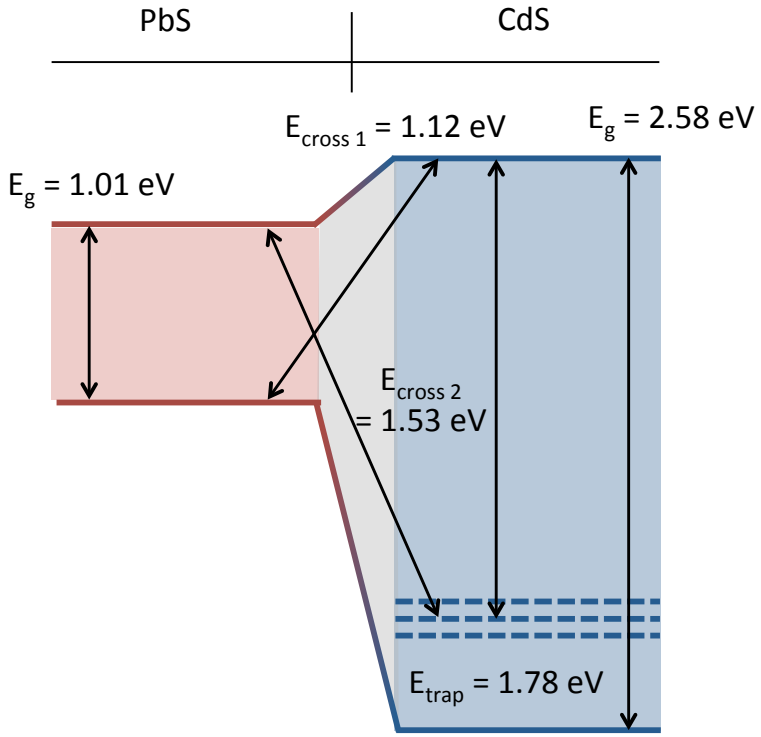


**Figure 4.5.** Schematic representation of the proposed type-I band alignment in Janus-like PbS/CdS heterostructures. The radiative emission pathways are illustrated and their corresponding energy peaks are shown.

The cooling rates in Janus-like NCs were studied through time-resolved photoluminescence (TRPL). PL lifetimes from Janus-like NCs were obtained for both visible and IR emission and were compared to lifetimes of pure-phase CdS and PbS QDs. Figure 4.6a shows PL intensity as a function of time for CdS QD seeds. The CdS PL intensity profile is a result of a convolution of two distinct radiative recombination mechanisms: a fast cooling band-to-band pathway with a lifetime of $\tau$ = 13.3 ns and a longer lived trap-state pathway with a lifetime of

$\tau$ ~ 120 ns. TRPL lifetimes of visible emission from PbS/CdS Janus-like NCs are nearly an order of magnitude longer—regardless of whether the excitation energy is above or below the CdS band gap (Figure 4.6b). Examining the NIR PL intensity reveals a lifetime for PbS QDs of $\tau$ = 2.17 µs while the 50:50 PbS:CdS Janus-like samples show similar lifetimes. TRPL lifetimes are summarized in a table at the bottom of Figure 4.6.

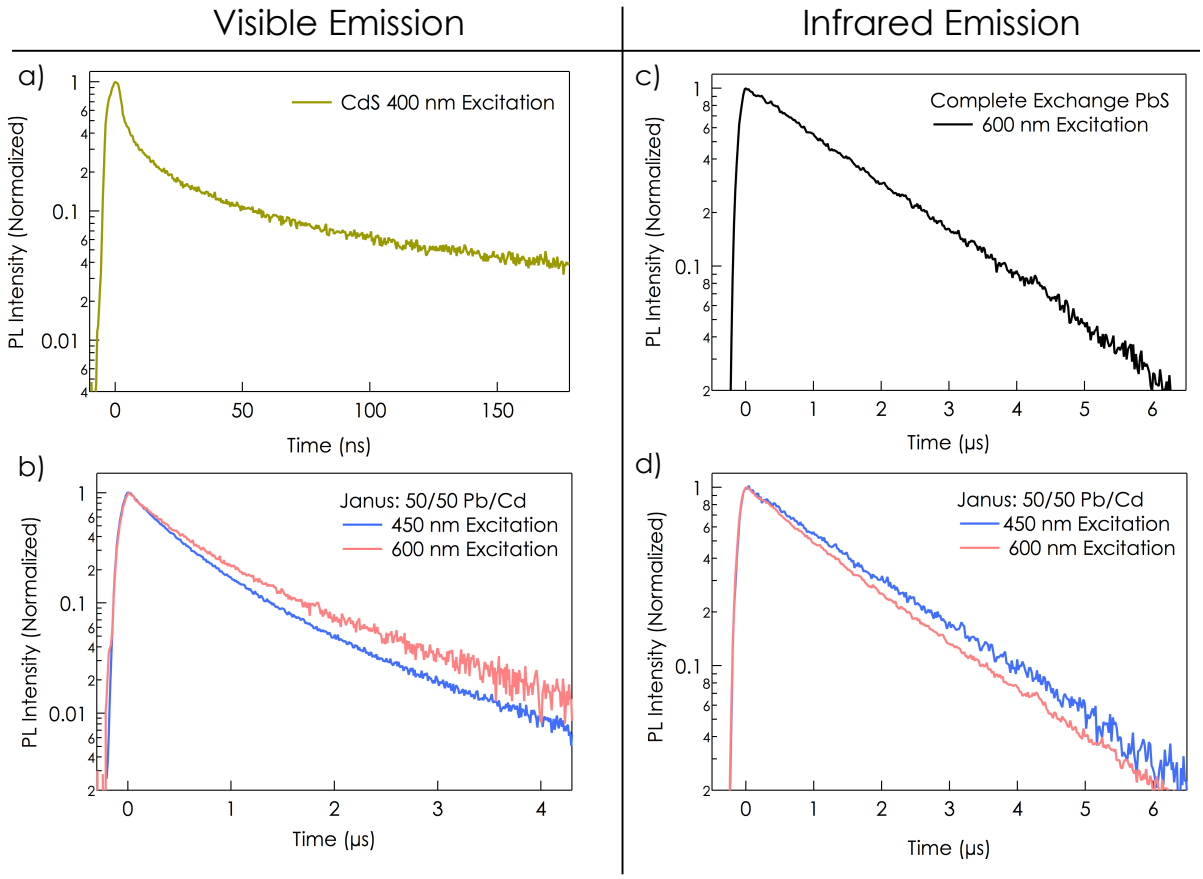


| | Lifetime 1 | Lifetime 2 |
|---|---|---|
| **PbS QDs - IR** | 2.17 µs | N/A |
| **CdS QDs - Visible** | 13.3 ns | ~120 ns |
| | **Into PbS** | **Into PbS + CdS** |
| **Janus - IR** | 2.0 µs | 1.7 µs |
| **Janus - Visible** | 1.07 µs | 0.96 µs |

**Figure 4.6**: Time-resolved photoluminescence (TRPL) lifetimes for visible emission from (a) CdS QDs and (b) PbS/CdS Janus-like heterostructures and for infrared emission from (c) complete exchange PbS QDs and (d) PbS/CdS Janus-like heterostructures. Calculated TRPL lifetimes are summarized below.

The slowed cooling observed with TRPL can help explain the enhanced MEG QY seen through TA spectroscopy described earlier. The MEG QY is expressed as

$$MEG\ QY = 1 + \frac{k_{MEG}^{(1)}}{k_{MEG}^{(1)} + k_{cool}} + \frac{k_{MEG}^{(1)} k_{MEG}^{(2)}}{\left(k_{MEG}^{(1)} + k_{cool}\right)\left(k_{MEG}^{(2)} + k_{cool}\right)} + \cdots$$

where $k_{MEG}^{(1)}$ is the MEG rate constant for producing $i$ + 1 hot excitons from $i$ high-energy photons and $k_{cool}$ is the hot exciton cooling rate. These two rates are in direct competition with each other and slowing the hot exciton cooling rate can promote the MEG rate. As mentioned above, a recent report by Cirloganu *et al.* showed an MEG QY above unity very near the fundamental thermodynamic limit of $2E_g$ using PbSe/CdSe core/shell QDs.[17] This enhanced MEG QY was partially attributed to the slowed cooling of hot holes by controlled energy level spacing between the core and shell valence band states. Similarly, the trap state manifold in CdS QDs when interfaced with PbS could provide a slow cooling pathway for hot holes in Janus-like PbS/CdS NCs and in turn provide a mechanism for enhanced MEG QY.

Perhaps the most important characteristic of Janus-like PbS/CdS heterostructured NCs is that photogenerated charges can be extracted in solar cells. This is contrary to other nanocrystalline heterostructures such as previously discussed PbSe/CdSe core/shell QDs in which photogenerated holes are confined within the PbSe core and are therefore not available for extraction.[17] As a final study and proof of principle, a series of solar cells were fabricated using Janus-like heterostructures as the active layer. In these devices, films of PbS/CdS NCs are formed in a layer-by-layer fashion by spincoating solutions of Janus-like NCs dispersed in octane onto $TiO_2$-coated FTO/glass substrates. Films are subsequently treated with $PbI_2$/DMF and MPA/methanol solutions to remove native, aliphatic ligands following similar procedures described in Chapter II and originally detailed by Crisp *et al*.[23] To complete devices, ~40 nm of

$MoO_x$ and 150 nm of Al are deposited by thermal evaporation. Figure 4.7a shows current-voltage (J-V) measurements for a Janus-like NC device resulting in an efficiency of 2.1% and Figure 4.7b shows the corresponding external quantum efficiency (EQE). While MEG may be occurring in this device, other limitations to carrier collection result in a peak EQE of only 65%. Nonetheless, through optimization of device structure and NC surface treatments, EQEs exceeding 100% could be attainable.

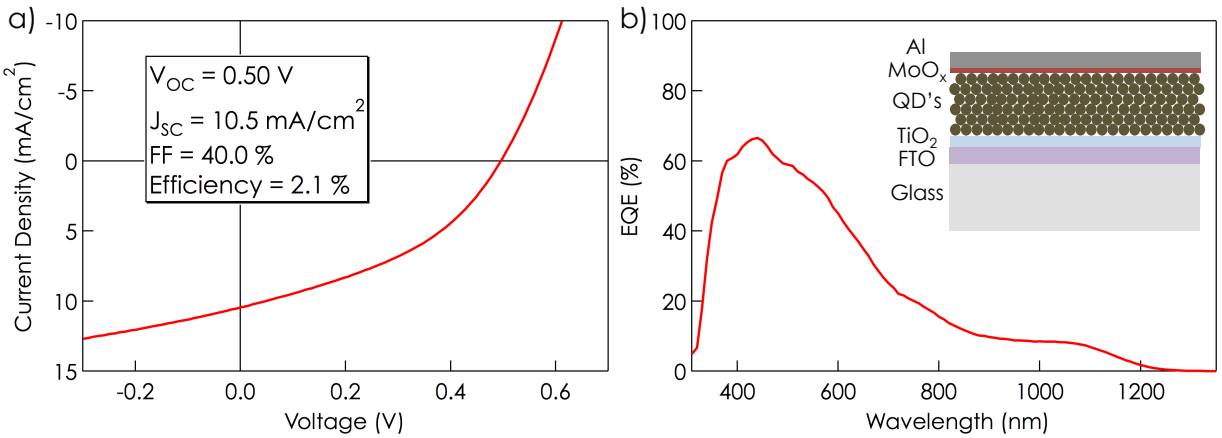


**Figure 4.7**. (a) J-V measurements from a solar cell using 50/50 PbS/CdS Janus-like heterostructures as the active absorber layer. (b) Corresponding external quantum efficiency (EQE) measurements from the same device. Insert shows the device structure.

### 4.4 Conclusion

We show that PbS/CdS Janus-like heterostructures, synthesized from the exchange of $Cd^{2+}$ from CdS QDs for $Pb^{2+}$ from $PbCl_2$ in oleylamine, show promise for enhancing MEG yields in quantum dot solar cells. These NCs have a highly tunable nature in which the size and composition of the NC can be altered while exhibiting two distinct pure-phase domains of PbS and CdS separated by a sharp lattice boundary. As a result of this structure, both photogenerated electrons and holes can be extracted in devices, unlike PbE/CdE (E = Se, S) core/shell structures in which photogenerated holes are confined within the core. TA spectroscopy reveals that Janus-like NCs show MEG QY above unity very near the thermodynamic limit of $2E_g$, with the

sharpest turn on for 50:50 PbS:CdS compositions. Steady-state PL as well as spectroscopic studies show that the band alignment between the two domains is most likely a type-I alignment. Furthermore, TRPL analyses display a slowed cooling in the visible emission decay from Janus-like NCs. This increased lifetime is an order of magnitude greater than carrier lifetimes within pure CdS QDs. We show functioning solar cells with Janus-like NCs used as the active layer, however continued optimization is needed in order to fully take advantage of the enchanced MEG potential in these NCs.

**4.5 References**:


1. Nozik, A. J., Quantum dot solar cells. *Physica E: Low-dimensional Systems and Nanostructures* **2002,** *14* (1–2), 115-120.

2. Bockelmann, U.; Bastard, G., Phonon scattering and energy relaxation in two-, one-, and zero-dimensional electron gases. *Physical Review B* **1990,** *42* (14), 8947-8951.

3. Stewart, J. T.; Padilha, L. A.; Bae, W. K.; Koh, W.-K.; Pietryga, J. M.; Klimov, V. I., Carrier Multiplication in Quantum Dots within the Framework of Two Competing Energy Relaxation Mechanisms. *The Journal of Physical Chemistry Letters* **2013,** *4* (12), 2061-2068.

4. Swarnkar, A.; Marshall, A. R.; Sanehira, E. M.; Chernomordik, B. D.; Moore, D. T.; Christians, J. A.; Chakrabarti, T.; Luther, J. M., Quantum dot–induced phase stabilization of α-CsPbI3 perovskite for high-efficiency photovoltaics. *Science* **2016,** *354* (6308), 92.

5. Liu, M.; Voznyy, O.; Sabatini, R.; Garcia de Arquer, F. P.; Munir, R.; Balawi, A. H.; Lan, X.; Fan, F.; Walters, G.; Kirmani, A. R.; Hoogland, S.; Laquai, F.; Amassian, A.; Sargent, E. H., Hybrid organic-inorganic inks flatten the energy landscape in colloidal quantum dot solids. *Nat Mater* **2017,** *16* (2), 258-263.

6. Semonin, O. E.; Luther, J. M.; Choi, S.; Chen, H.-Y.; Gao, J.; Nozik, A. J.; Beard, M. C., Peak External Photocurrent Quantum Efficiency Exceeding 100% via MEG in a Quantum Dot Solar Cell. *Science* **2011,** *334* (6062), 1530-1533.

7. Böhm, M. L.; Jellicoe, T. C.; Tabachnyk, M.; Davis, N. J. L. K.; Wisnivesky-Rocca-Rivarola, F.; Ducati, C.; Ehrler, B.; Bakulin, A. A.; Greenham, N. C., Lead Telluride Quantum Dot Solar Cells Displaying External Quantum Efficiencies Exceeding 120%. *Nano Letters* **2015,** *15* (12), 7987-7993.

8. Gabor, N. M.; Zhong, Z.; Bosnick, K.; Park, J.; McEuen, P. L., Extremely Efficient Multiple Electron-Hole Pair Generation in Carbon Nanotube Photodiodes. *Science* **2009,** *325* (5946), 1367.

9. Sambur, J. B.; Novet, T.; Parkinson, B. A., Multiple Exciton Collection in a Sensitized Photovoltaic System. *Science* **2010,** *330* (6000), 63.

10. Beard, M. C.; Midgett, A. G.; Law, M.; Semonin, O. E.; Ellingson, R. J.; Nozik, A. J., Variations in the Quantum Efficiency of Multiple Exciton Generation for a Series of Chemically Treated PbSe Nanocrystal Films. *Nano Letters* **2009,** *9* (2), 836-845.

11. Luther, J. M.; Beard, M. C.; Song, Q.; Law, M.; Ellingson, R. J.; Nozik, A. J., Multiple Exciton Generation in Films of Electronically Coupled PbSe Quantum Dots. *Nano Letters* **2007,** *7* (6), 1779-1784.

12. Murphy, J. E.; Beard, M. C.; Norman, A. G.; Ahrenkiel, S. P.; Johnson, J. C.; Yu, P.; Mićić, O. I.; Ellingson, R. J.; Nozik, A. J., PbTe Colloidal Nanocrystals: Synthesis, Characterization, and Multiple Exciton Generation. *Journal of the American Chemical Society* **2006,** *128* (10), 3241-3247.

13. Midgett, A. G.; Luther, J. M.; Stewart, J. T.; Smith, D. K.; Padilha, L. A.; Klimov, V. I.; Nozik, A. J.; Beard, M. C., Size and Composition Dependent Multiple Exciton Generation Efficiency in PbS, PbSe, and PbSxSe1–x Alloyed Quantum Dots. *Nano Letters* **2013,** *13* (7), 3078-3085.

14. Midgett, A. G.; Hillhouse, H. W.; Hughes, B. K.; Nozik, A. J.; Beard, M. C., Flowing versus Static Conditions for Measuring Multiple Exciton Generation in PbSe Quantum Dots. *The Journal of Physical Chemistry C* **2010,** *114* (41), 17486-17500.

15. Schaller, R. D.; Klimov, V. I., High Efficiency Carrier Multiplication in PbSe Nanocrystals: Implications for Solar Energy Conversion. *Physical Review Letters* **2004,** *92* (18), 186601.

16. Eshet, H.; Baer, R.; Neuhauser, D.; Rabani, E., Theory of highly efficient multiexciton generation in type-II nanorods. *Nature Communications* **2016,** *7*, 13178.

17. Cirloganu, C. M.; Padilha, L. A.; Lin, Q.; Makarov, N. S.; Velizhanin, K. A.; Luo, H.; Robel, I.; Pietryga, J. M.; Klimov, V. I., Enhanced carrier multiplication in engineered quasi-type-II quantum dots. *Nature Communications* **2014,** *5*, 4148.

18. Zhang, J.; Chernomordik, B. D.; Crisp, R. W.; Kroupa, D. M.; Luther, J. M.; Miller, E. M.; Gao, J.; Beard, M. C., Preparation of Cd/Pb Chalcogenide Heterostructured Janus Particles via Controllable Cation Exchange. *ACS Nano* **2015,** *9* (7), 7151-63.

19. Zhang, J.; Gao, J.; Church, C. P.; Miller, E. M.; Luther, J. M.; Klimov, V. I.; Beard, M. C., PbSe Quantum Dot Solar Cells with More than 6% Efficiency Fabricated in Ambient Atmosphere. *Nano Letters* **2014,** *14* (10), 6010-6015.

20. Chernomordik, B. D.; Marshall, A. R.; Pach, G. F.; Luther, J. M.; Beard, M. C., Quantum Dot Solar Cell Fabrication Protocols. *Chemistry of Materials* **2017,** *29* (1), 189-198.

21. Utterback, J. K.; Grennell, A. N.; Wilker, M. B.; Pearce, O. M.; Eaves, J. D.; Dukovic, G., Observation of trapped-hole diffusion on the surfaces of CdS nanorods. *Nat Chem* **2016,** *8* (11), 1061-1066.

22. Saunders, A. E.; Ghezelbash, A.; Sood, P.; Korgel, B. A., Synthesis of High Aspect Ratio Quantum-Size CdS Nanorods and Their Surface-Dependent Photoluminescence. *Langmuir* **2008,** *24* (16), 9043-9049.

23. Crisp, R. W.; Kroupa, D. M.; Marshall, A. R.; Miller, E. M.; Zhang, J.; Beard, M. C.; Luther, J. M., Metal Halide Solid-State Surface Treatment for High Efficiency PbS and PbSe QD Solar Cells. *Scientific reports* **2015,** *5*, 9945.

CHAPTER V

# Conclusion

Nanoscience research is a rapidly expanding field and new applications continue to develop for nanostructured materials. This thesis has discussed one application in particular—photovoltaics. With global energy demand continuing to rise, it is important to study novel materials that could boost efficiency limits and lower manufacturing costs of photovoltaic systems. One promising candidate to achieve these goals for future photovoltaic application is colloidal quantum dots. Colloidal quantum dot research has become a fast advancing and diverse field of research within the past twenty years and new synthetic techniques and device architectures are being developed at an increasing rate. Chapter II of this thesis was aimed as a way of providing a clear, standardized methodology for producing high-efficiency lead-chalcogenide colloidal quantum dot solar cells. This section provided details beyond the scope of what is reported in a typical scientific paper in hopes of providing a starting point for emerging QD research groups.

The promise of future generation PV, however, lies in breaking the standard Shockley-Queisser limit for a single-junction solar cell. The ability to tune the band gap of lead-chalcogenide QDs over a wide range of energy lends these structures well toward use in tandem and higher-order multi-junction solar cells. Chapter III of this thesis showed the potential of combining PbS QDs with solution-processed CdTe nanocrystals in a tandem solar cell. This

result showed promise toward constructing a fully solution-processed tandem solar cell, which not only achieves high theoretical efficiencies, but could also greatly benefit cost of fabrication.

Chapter IV explored the prospect of engineering the nanocrystal itself for more efficiently harnessing MEG, which could also lead toward increased efficiencies in QDSCs. PbS/CdS Janus-like heterostructures were shown to demonstrate MEG quantum yields above unity very near $2E_g$. Time-resolved PL revealed slowed cooling of the visible PL intensity, which could help explain the observed enhanced MEG. Furthermore, we showed that PbS/CdS Janus-like heterostructures could be incorporated into conventional solar cell architectures to construct fully functioning devices.

Overall, QDSCs show great promise for future generation photovoltaic technology. Certified efficiencies are climbing rapidly, and as a result, a great amount of attention has been given to the field. Undoubtedly though, there are still many challenges to overcome before QDSCs reach industrial processing. However, through continued exploration of these nanostructured systems we can achieve a greater understanding of the mechanisms at play and therefore unlock the full potential of QDSCs.

COMPREHENSIVE BIBLIOGRAPHY

## Chapter 1


1. Bruchez, M.; Moronne, M.; Gin, P.; Weiss, S.; Alivisatos, A. P., Semiconductor Nanocrystals as Fluorescent Biological Labels. *Science* **1998,** *281* (5385), 2013.

2. Konstantatos, G.; Howard, I.; Fischer, A.; Hoogland, S.; Clifford, J.; Klem, E.; Levina, L.; Sargent, E. H., Ultrasensitive solution-cast quantum dot photodetectors. *Nature* **2006,** *442* (7099), 180-183.

3. Qian, L.; Zheng, Y.; Xue, J.; Holloway, P. H., Stable and efficient quantum-dot light-emitting diodes based on solution-processed multilayer structures. *Nat Photon* **2011,** *5* (9), 543-548.

4. Nozik, A. J., Quantum dot solar cells. *Physica E: Low-dimensional Systems and Nanostructures* **2002,** *14* (1–2), 115-120.

5. Hanna, M.; Nozik, A., Solar conversion efficiency of photovoltaic and photoelectrolysis cells with carrier multiplication absorbers. *Journal of Applied Physics* **2006,** *100* (7), 074510.

6. Zhang, J.; Gao, J.; Church, C. P.; Miller, E. M.; Luther, J. M.; Klimov, V. I.; Beard, M. C., PbSe Quantum Dot Solar Cells with More than 6% Efficiency Fabricated in Ambient Atmosphere. *Nano Letters* **2014**.

7. Zhang, J.; Gao, J.; Miller, E. M.; Luther, J. M.; Beard, M. C., Diffusion-Controlled Synthesis of PbS and PbSe Quantum Dots with in Situ Halide Passivation for Quantum Dot Solar Cells. *ACS Nano* **2013,** *8* (1), 614-622.

8. Hines, M. A.; Scholes, G. D., Colloidal PbS Nanocrystals with Size-Tunable Near-Infrared Emission: Observation of Post-Synthesis Self-Narrowing of the Particle Size Distribution. *Advanced Materials* **2003,** *15* (21), 1844-1849.

9. Weidman, M. C.; Beck, M. E.; Hoffman, R. S.; Prins, F.; Tisdale, W. A., Monodisperse, Air-Stable PbS Nanocrystals via Precursor Stoichiometry Control. *ACS Nano* **2014,** *8* (6), 6363-6371.

10. Hendricks, M. P.; Campos, M. P.; Cleveland, G. T.; Jen-La Plante, I.; Owen, J. S., A tunable library of substituted thiourea precursors to metal sulfide nanocrystals. *Science* **2015,** *348* (6240), 1226.

11. Anderson, N. C.; Hendricks, M. P.; Choi, J. J.; Owen, J. S., Ligand Exchange and the Stoichiometry of Metal Chalcogenide Nanocrystals: Spectroscopic Observation of Facile Metal-Carboxylate Displacement and Binding. *Journal of the American Chemical Society 135* (49), 18536-18548.

12. Kagan, C. R.; Murray, C. B.; Nirmal, M.; Bawendi, M. G., Electronic Energy Transfer in CdSe Quantum Dot Solids. *Physical Review Letters* **1996,** *76* (9), 1517-1520.

13. Talapin, D. V.; Lee, J.-S.; Kovalenko, M. V.; Shevchenko, E. V., Prospects of Colloidal Nanocrystals for Electronic and Optoelectronic Applications. *Chemical Reviews* **2010,** *110* (1), 389-458.

14. Crisp, R. W.; Kroupa, D. M.; Marshall, A. R.; Miller, E. M.; Zhang, J.; Beard, M. C.; Luther, J. M., Metal Halide Solid-State SurfaceTreatment for High Efficiency PbS and PbSe QD Solar Cells. *Scientific Reports* **2015,** *5*.

15. Marshall, A. R.; Young, M. R.; Nozik, A. J.; Beard, M. C.; Luther, J. M., Exploration of Metal Chloride Uptake for Improved Performance Characteristics of PbSe Quantum Dot Solar Cells. *The Journal of Physical Chemistry Letters* **2015,** *6* (15), 2892-2899.

16. Liu, M.; de Arquer, F. P. G.; Li, Y.; Lan, X.; Kim, G.-H.; Voznyy, O.; Jagadamma, L. K.; Abbas, A. S.; Hoogland, S.; Lu, Z.; Kim, J. Y.; Amassian, A.; Sargent, E. H., Double-Sided Junctions Enable High-Performance Colloidal-Quantum-Dot Photovoltaics. *Advanced Materials* **2016,** *28* (21), 4142-4148.

17. Lan, X.; Voznyy, O.; García de Arquer, F. P.; Liu, M.; Xu, J.; Proppe, A. H.; Walters, G.; Fan, F.; Tan, H.; Liu, M.; Yang, Z.; Hoogland, S.; Sargent, E. H., 10.6% Certified Colloidal Quantum Dot Solar Cells via Solvent-Polarity-Engineered Halide Passivation. *Nano Letters* **2016,** *16* (7), 4630-4634.

18. Swarnkar, A.; Marshall, A. R.; Sanehira, E. M.; Chernomordik, B. D.; Moore, D. T.; Christians, J. A.; Chakrabarti, T.; Luther, J. M., Quantum dot–induced phase stabilization of α-CsPbI3 perovskite for high-efficiency photovoltaics. *Science* **2016,** *354* (6308), 92.

19. Kim, S.; Noh, J.; Choi, H.; Ha, H.; Song, J. H.; Shim, H. C.; Jang, J.; Beard, M. C.; Jeong, S., One-Step Deposition of Photovoltaic Layers Using Iodide Terminated PbS Quantum Dots. *The Journal of Physical Chemistry Letters* **2014,** *5* (22), 4002-4007.

20. Liu, M.; Voznyy, O.; Sabatini, R.; Garcia de Arquer, F. P.; Munir, R.; Balawi, A. H.; Lan, X.; Fan, F.; Walters, G.; Kirmani, A. R.; Hoogland, S.; Laquai, F.; Amassian, A.; Sargent, E. H., Hybrid organic-inorganic inks flatten the energy landscape in colloidal quantum dot solids. *Nat Mater* **2017,** *16* (2), 258-263.

21. Ning, Z.; Dong, H.; Zhang, Q.; Voznyy, O.; Sargent, E. H., Solar Cells Based on Inks of n-Type Colloidal Quantum Dots. *ACS Nano* **2014**.

22. Aqoma, H.; Al Mubarok, M.; Hadmojo, W. T.; Lee, E.-H.; Kim, T.-W.; Ahn, T. K.; Oh, S.-H.; Jang, S.-Y., High-Efficiency Photovoltaic Devices using Trap-Controlled Quantum-Dot Ink prepared via Phase-Transfer Exchange. *Advanced Materials* **2017**, 1605756-n/a.

23. Carey, G. H.; Abdelhady, A. L.; Ning, Z.; Thon, S. M.; Bakr, O. M.; Sargent, E. H., Colloidal Quantum Dot Solar Cells. *Chemical Reviews* **2015,** *115* (23), 12732-12763.

24. Carey, G. H.; Levina, L.; Comin, R.; Voznyy, O.; Sargent, E. H., Record Charge Carrier Diffusion Length in Colloidal Quantum Dot Solids via Mutual Dot-To-Dot Surface Passivation. *Advanced Materials* **2015,** *27* (21), 3325-3330.

25. Yoshikawa, K.; Kawasaki, H.; Yoshida, W.; Irie, T.; Konishi, K.; Nakano, K.; Uto, T.; Adachi, D.; Kanematsu, M.; Uzu, H.; Yamamoto, K., Silicon heterojunction solar cell with interdigitated back contacts for a photoconversion efficiency over 26%. *Nature Energy* **2017,** *2*, 17032.

26. Crisp, R. W.; Pach, G. F.; Kurley, J. M.; France, R. M.; Reese, M. O.; Nanayakkara, S. U.; MacLeod, B. A.; Talapin, D. V.; Beard, M. C.; Luther, J. M., Tandem Solar Cells from Solution-Processed CdTe and PbS Quantum Dots Using a ZnTe–ZnO Tunnel Junction. *Nano Letters* **2017**.

27. Rühle, S., The detailed balance limit of perovskite/silicon and perovskite/CdTe tandem solar cells. *physica status solidi (a)* **2017**, 1600955-n/a.

28. Bush, K. A.; Palmstrom, A. F.; Yu, Z. J.; Boccard, M.; Cheacharoen, R.; Mailoa, J. P.; McMeekin, D. P.; Hoye, R. L. Z.; Bailie, C. D.; Leijtens, T.; Peters, I. M.; Minichetti, M. C.; Rolston, N.; Prasanna, R.; Sofia, S.; Harwood, D.; Ma, W.; Moghadam, F.; Snaith, H. J.; Buonassisi, T.; Holman, Z. C.; Bent, S. F.; McGehee, M. D., 23.6%-efficient monolithic perovskite/silicon tandem solar cells with improved stability. *Nature Energy* **2017,** *2*, 17009.

29. Wang, X.; Koleilat, G. I.; Tang, J.; Liu, H.; Kramer, I. J.; Debnath, R.; Brzozowski, L.; Barkhouse, D. A. R.; Levina, L.; Hoogland, S.; Sargent, E. H., Tandem colloidal quantum dot solar cells employing a graded recombination layer. *Nat Photon* **2011,** *5* (8), 480-484.

30. Vos, A. D., Detailed Balance Limit of the Efficiency of Tandem Solar Cells. *J. Phys. D: Appl. Phys.* **1980,** *13* (5), 839-46.

31. Kurtz, S. R.; Faine, P.; Olson, J., Modeling of two‐junction, series‐connected tandem solar cells using top‐cell thickness as an adjustable parameter. *Journal of Applied Physics* **1990,** *68* (4), 1890-1895.

32. Gabor, N. M.; Zhong, Z.; Bosnick, K.; Park, J.; McEuen, P. L., Extremely Efficient Multiple Electron-Hole Pair Generation in Carbon Nanotube Photodiodes. *Science* **2009,** *325* (5946), 1367.

33. Luther, J. M.; Beard, M. C.; Song, Q.; Law, M.; Ellingson, R. J.; Nozik, A. J., Multiple Exciton Generation in Films of Electronically Coupled PbSe Quantum Dots. *Nano Letters* **2007,** *7* (6), 1779-1784.

34. Midgett, A. G.; Luther, J. M.; Stewart, J. T.; Smith, D. K.; Padilha, L. A.; Klimov, V. I.; Nozik, A. J.; Beard, M. C., Size and Composition Dependent Multiple Exciton Generation Efficiency in PbS, PbSe, and PbSxSe1–x Alloyed Quantum Dots. *Nano Letters* **2013,** *13* (7), 3078-3085.

35. Semonin, O. E.; Luther, J. M.; Choi, S.; Chen, H.-Y.; Gao, J.; Nozik, A. J.; Beard, M. C., Peak External Photocurrent Quantum Efficiency Exceeding 100% via MEG in a Quantum Dot Solar Cell. *Science* **2011,** *334* (6062), 1530-1533.

36. Cirloganu, C. M.; Padilha, L. A.; Lin, Q.; Makarov, N. S.; Velizhanin, K. A.; Luo, H.; Robel, I.; Pietryga, J. M.; Klimov, V. I., Enhanced carrier multiplication in engineered quasi-type-II quantum dots. *Nature Communications* **2014,** *5*, 4148.

37. Eshet, H.; Baer, R.; Neuhauser, D.; Rabani, E., Theory of highly efficient multiexciton generation in type-II nanorods. *Nature Communications* **2016,** *7*, 13178.

38. Zhang, J.; Chernomordik, B. D.; Crisp, R. W.; Kroupa, D. M.; Luther, J. M.; Miller, E. M.; Gao, J.; Beard, M. C., Preparation of Cd/Pb Chalcogenide Heterostructured Janus Particles via Controllable Cation Exchange. *ACS Nano* **2015,** *9* (7), 7151-63.

**Chapter 2**

1. Brown, P. R.; Kim, D.; Lunt, R. R.; Zhao, N.; Bawendi, M. G.; Grossman, J. C.; Bulovi, V. Energy Level Modification in Lead Sulfide Quantum Dot Thin Films through Ligand Exchange. *ACS Nano* **2014**, *8*, 5863–5872.

2. Goodwin, E. D.; Straus, D. B.; Gaulding, E. A.; Murray, C. B.; Kagan, C. R. The Effects of Inorganic Surface Treatments on Photogenerated Carrier Mobility and Lifetime in PbSe Quantum Dot Thin Films. *Chem. Phys.* **2015**, *471*, 32–36.

3. Klimov, V. I.; Baker, T. A.; Lim, J.; Velizhanin, K. A.; McDaniel, H. Quality Factor of Luminescent Solar Concentrators and Practical Concentration Limits Attainable with Semiconductor Quantum Dots. *ACS Photonics* **2016**, *3*, 1138–1148.

4. Ellingson, R. J.; Beard, M. C.; Johnson, J. C.; Yu, P.; Micic, O. I.; Nozik, A. J.; Shabaev, A.; Efros, A. L. Highly Efficient Multiple Exciton Generation in Colloidal PbSe and PbS Quantum Dots. *Nano Lett.* **2005**, *5*, 865–871.

5. Lee, D. C.; Robel, I.; Pietryga, J. M.; Klimov, V. I. Infrared-Active Heterostructured Nanocrystals with Ultralong Carrier Lifetimes. *J. Am. Chem. Soc.* **2010**, *132*, 9960–9962.

6. Cirloganu, C. M.; Padilha, L. a; Lin, Q.; Makarov, N. S.; Velizhanin, K. a; Luo, H.; Robel, I.; Pietryga, J. M.; Klimov, V. I. Enhanced Carrier Multiplication in Engineered Quasi-Type-II Quantum Dots. *Nat. Commun.* **2014**, *5*, 4148.

7. Brown, P. R.; Kim, D.; Lunt, R. R.; Zhao, N.; Bawendi, M. G.; Grossman, J. C.; Bulovic, V. Energy Level Modification in Lead Sulfide Quantum Dot Thin Films Through Ligand Exchange. *ACS Nano* **2014**, *8*, 5863–5872.

8. Supran, G. J.; Shirasaki, Y.; Song, K. W.; Caruge, J.-M.; Kazlas, P. T.; Coe-Sullivan, S.; Andrew, T. L.; Bawendi, M. G.; Bulović, V. QLEDs for Displays and Solid-State Lighting. *MRS Bull.* **2013**, *38*, 703–711.

9. Konstantatos, G.; Badioli, M.; Gaudreau, L.; Osmond, J.; Bernechea, M.; de Arquer, F. P. G.; Gatti, F.; Koppens, F. H. L. Hybrid graphene–Quantum Dot Phototransistors with Ultrahigh Gain. *Nat. Nanotechnol.* **2012**, *7*, 363–368.

10. Kim, S.; Lim, Y. T.; Soltesz, E. G.; De Grand, A. M.; Lee, J.; Nakayama, A.; Parker, J. A.; Mihaljevic, T.; Laurence, R. G.; Dor, D. M.; et al. Near-Infrared Fluorescent Type II Quantum Dots for Sentinel Lymph Node Mapping. *Nat. Biotechnol.* **2004**, *22*, 93–97.

11. Lan, X.; Voznyy, O.; García de Arquer, F. P.; Liu, M.; Xu, J.; Proppe, A. H.; Walters, G.; Fan, F.; Tan, H.; Liu, M.; et al. 10.6% Certified Colloidal Quantum Dot Solar Cells via Solvent-Polarity-Engineered Halide Passivation. *Nano Lett.* **2016**, *16*, 4630–4634.

12. Wang, H.; Pei, Y.; Lalonde, A. D.; Snyder, G. J. Heavily Doped P-Type PbSe with High Thermoelectric Performance: An Alternative for PbTe. *Adv. Mater.* **2011**, *23*, 1366–1370.

13. Supran, G. J.; Song, K. W.; Hwang, G. W.; Correa, R. E.; Scherer, J.; Dauler, E. a; Shirasaki, Y.; Bawendi, M. G.; Bulović, V. High-Performance Shortwave-Infrared Light-Emitting Devices Using Core–Shell (PbS–CdS) Colloidal Quantum Dots. *Adv. Mater.* **2015**, 1437–1442.

14. Mashford, B.; Stevenson, M.; Popovic, Z. High-Efficiency Quantum-Dot Light-Emitting Devices with Enhanced Charge Injection. *Nat. Photonics* **2013**, *7*, 407–412.

15. Hanna, M. C.; Nozik, a. J. Solar Conversion Efficiency of Photovoltaic and Photoelectrolysis Cells with Carrier Multiplication Absorbers. *J. Appl. Phys.* **2006**, *100*, 074510.

16. Semonin, O. E.; Luther, J. M.; Choi, S.; Chen, H.-Y.; Gao, J.; Nozik, a. J.; Beard, M. C. Peak External Photocurrent Quantum Efficiency Exceeding 100% via MEG in a Quantum Dot Solar Cell. *Science* **2011**, *334*, 1530–1533.

17. Davis, N. J. L. K.; Böhm, M. L.; Tabachnyk, M.; Wisnivesky-Rocca-Rivarola, F.; Jellicoe, T. C.; Ducati, C.; Ehrler, B.; Greenham, N. C. Multiple-Exciton Generation in Lead Selenide Nanorod Solar Cells with External Quantum Efficiencies Exceeding 120%. *Nat. Commun.* **2015**, *6*, 8259.

18. Böhm, M. L.; Jellicoe, T. C.; Tabachnyk, M.; Davis, N. J. L. K.; Wisnivesky Rocca Rivarola, F.; Ducati, C.; Ehrler, B.; Bakulin, A. a.; Greenham, N. C. Lead Telluride Quantum Dot Solar Cells Displaying External Quantum Efficiencies Exceeding 120%. *Nano Lett.* **2015**, *15*, 7987–7993.

19. Cunningham, P. D.; Boercker, J. E.; Foos, E. E.; Lumb, M. P.; Smith, A. R.; Tischler, J. G.; Melinger, J. S. Enhanced Multiple Exciton Generation in Quasi-One-Dimensional Semiconductors. *Nano Lett.* **2011**, *11*, 3476–3481.

20. Yang, Y.; Ostrowski, D. P.; France, R. M.; Zhu, K.; van de Lagemaat, J.; Luther, J. M.; Beard, M. C. Observation of a Hot-Phonon Bottleneck in Lead-Iodide Perovskites. *Nat. Photonics* **2016**, *10*, 53–59.

21. Du, J.; Du, Z.; Hu, J.-S.; Pan, Z.; Shen, Q.; Sun, J.; Long, D.; Dong, H.; Sun, L.; Zhong, X.; et al. Zn-Cu-In-Se Quantum Dot Solar Cells with a Certified Power Conversion Efficiency of 11.6. *J. Am. Chem. Soc.* **2016**, *138*, 4201–4209.

22. Zhang, J.; Chernomordik, B. D.; Crisp, R. W.; Kroupa, D. M.; Luther, J. M.; Miller, E. M.; Gao, J.; Beard, M. C. Preparation of Cd/Pb Chalcogenide Heterostructured Janus Particles via Controllable Cation Exchange. *ACS Nano* **2015**, *9*, 7151–7163.

23. Zhang, J.; Gao, J.; Church, C. P.; Miller, E. M.; Luther, J. M.; Klimov, V. I.; Beard, M. C. PbSe Quantum Dot Solar Cells with More than 6% Efficiency Fabricated in Ambient Atmosphere. *Nano Lett.* **2014**, *14*, 6010–6015.

24. Hu, Y.; Diao, X.; Wang, C.; Hao, W.; Wang, T. Effects of Heat Treatment on Properties of ITO Films Prepared by Rf Magnetron Sputtering. *Vacuum* **2004**, *75*, 183–188.

25. Church, C. P.; Muthuswamy, E.; Zhai, G.; Kauzlarich, S. M.; Carter, S. A. Quantum Dot Ge/TiO2 Heterojunction Photoconductor Fabrication and Performance. *Appl. Phys. Lett.* **2013**, *103*, 223506.

26. Gao, J.; Jeong, S.; Lin, F.; Erslev, P. T.; Semonin, O. E.; Luther, J. M.; Beard, M. C. Improvement in Carrier Transport Properties by Mild Thermal Annealing of PbS Quantum Dot Solar Cells. *Appl. Phys. Lett.* **2013**, *102*, 043506.

27. Emery, K. Measurement and Characterization of Solar Cells and Modules. In *Handbook of Photovoltaic Science and Engineering*; 2011; pp 797–840.

28. Snaith, H. J. How Should You Measure Your Excitonic Solar Cells? *Energy Environ. Sci.* **2012**, *5*, 6513–6520.

29. Law, M.; Beard, M. C.; Choi, S.; Luther, J. M.; Hanna, M. C.; Nozik, A. J. Determining the Internal Quantum Efficiency of PbSe Nanocrystal Solar Cells with the Aid of an Optical Model. *Nano Lett.* **2008**, *8*, 3904–3910.

30. Sites, J. R.; Tavakolian, H.; Sasala, R. A. Analysis of Apparent Quantum Efficiency. *Sol. Cells* **1990**, *29*, 39–48.

31. Hegedus, S. S.; Shafarman, W. N. Thin-Film Solar Cells: Device Measurements and Analysis. *Prog. Photovoltaics Res. Appl.* **2004**, *12*, 155–176.

32. Zhang, H.; Hyun, B. R.; Wise, F. W.; Robinson, R. D. A Generic Method for Rational Scalable Synthesis of Monodisperse Metal Sulfide Nanocrystals. *Nano Lett.* **2012**, *12*, 5856–5860.

33. Pu, C.; Zhou, J.; Lai, R.; Niu, Y.; Nan, W.; Peng, X. Highly Reactive, Flexible yet Green Se Precursor for Metal Selenide Nanocrystals: Se-Octadecene Suspension (Se-SUS). *Nano Res.* **2013**, *6*, 652–670.

34. Luther, J. M.; Law, M.; Beard, M. C.; Song, Q.; Reese, M. O.; Ellingson, R. J.; Nozik, A. J. Schottky Solar Cells Based on Colloidal Nanocrystal Films. *Nano Lett.* **2008**, *8*, 3488–3492.

35. NREL. Best Research-Cell Efficiencies http://www.nrel.gov/ncpv/images/efficiency_chart.jpg (accessed Jul 17, 2016).

36. Leschkies, K. S.; Beatty, T. J.; Kang, M. S.; Norris, D. J.; Aydil, E. S. Solar Cells Based on Junctions between Colloidal PbSe Nanocrystals and Thin ZnO Films. *ACS Nano* **2009**, *3*, 3638–3648.

37. Pattantyus-Abraham, A. G.; Kramer, I. J.; Barkhouse, A. R.; Wang, X.; Konstantatos, G.; Debnath, R.; Levina, L.; Raabe, I.; Nazeeruddin, M. K.; Grätzel, M.; et al. Depleted-Heterojunction Colloidal Quantum Dot Solar Cells. *ACS Nano* **2010**, *4*, 3374–3380.

38. Gao, J.; Luther, J. M.; Semonin, O. E.; Ellingson, R. J.; Nozik, A. J.; Beard, M. C. Quantum Dot Size Dependent J-V Characteristics in Heterojunction ZnO/PbS Quantum Dot Solar Cells. *Nano Lett.* **2011**, *11*, 1002–1008.

39. Gao, J.; Perkins, C. L.; Luther, J.; Hanna, M.; Chen, H.; Semonin, O.; Nozik, A.; Ellingson, R. J.; Beard, M. N-Type Transition Metal Oxide as a Hole Extraction Layer in PbS Quantum Dot Solar Cells. *Nano Lett.* **2011**, *11*, 3263–3266.

40. Semonin, O. E.; Luther, J. M.; Choi, S.; Chen, H.-Y.; Gao, J.; Nozik, a. J.; Beard, M. C. Peak External Photocurrent Quantum Efficiency Exceeding 100% via MEG in a Quantum Dot Solar Cell. *Science* **2011**, *334*, 1530–1533.

41. Chuang, C.-H. M.; Brown, P. R.; Bulović, V.; Bawendi, M. G. Improved Performance and Stability in Quantum Dot Solar Cells through Band Alignment Engineering. *Nat. Mater.* **2014**, *13*, 796–801.

42. Oh, S. J.; Berry, N. E.; Choi, J. H.; Gaulding, E. A.; Paik, T.; Hong, S. H.; Murray, C. B.; Kagan, C. R. Stoichiometric Control of Lead Chalcogenide Nanocrystal Solids to Enhance Their Electronic and Optoelectronic Device Performance. *ACS Nano* **2013**, *7*, 2413–2421.

43. Crisp, R. W.; Kroupa, D. M.; Marshall, A. R.; Miller, E. M.; Zhang, J.; Beard, M. C.; Luther, J. M. Metal Halide Solid-State Surface Treatment for High Efficiency PbS and PbSe QD Solar Cells. *Sci. Rep.* **2015**, *5*, 9945.

44. Marshall, A. R.; Young, M. R.; Nozik, A. J.; Beard, M. C.; Luther, J. M. Exploration of Metal Chloride Uptake for Improved Performance Characteristics of PbSe Quantum Dot Solar Cells. *J. Phys. Chem. Lett.* **2015**, *6*, 2892–2899.

45. Gao, J.; Johnson, J. C. Charge Trapping in Bright and Dark States of Coupled PbS Quantum Dot Films. *ACS Nano* **2012**, *6*, 3292–3303.

46. Tang, J.; Kemp, K. W.; Hoogland, S.; Jeong, K. S.; Liu, H.; Levina, L.; Furukawa, M.; Wang, X.; Debnath, R.; Cha, D.; et al. Colloidal-Quantum-Dot Photovoltaics Using Atomic-Ligand Passivation. *Nat. Mater.* **2011**, *10*, 765–771.

47. Ip, A. H.; Thon, S. M.; Hoogland, S.; Voznyy, O.; Zhitomirsky, D.; Debnath, R.; Levina, L.; Rollny, L. R.; Carey, G. H.; Fischer, A.; et al. Hybrid Passivated Colloidal Quantum Dot Solids. *Nat. Nanotechnol.* **2012**, *7*, 577–582.

48. Marshall, A. R.; Beard, M. C.; Johnson, J. C. Nongeminate Radiative Recombination of Free Charges in Cation-Exchanged PbS Quantum Dot Films. *Chem. Phys.* **2016**, *471*, 75–80.

49. Kim, S.; Marshall, A. R.; Kroupa, D. M.; Miller, E. M.; Luther, J. M.; Jeong, S.; Beard, M. C. Air-Stable and Efficient PbSe Quantum-Dot Solar Cells Based upon Quantum Dots. *ACS Nano* **2015**, *9*, 8157–8164.

50. Moreels, I.; Fritzinger, B.; Martins, J. C.; Hens, Z. Surface Chemistry of Colloidal PbSe Nanocrystals. *J. Am. Chem. Soc.* **2008**, *130*, 15081–15086.

51. Zhang, J.; Gao, J.; Miller, E. M.; Luther, J. M.; Beard, M. C. Diffusion-Controlled Synthesis of PbS and PbSe Quantum Dots with in Situ Halide Passivation for Quantum Dot Solar Cells. *ACS Nano* **2014**, *8*, 614–622.

52. Selinsky, R. S.; Ding, Q.; Faber, M. S.; Wright, J. C.; Jin, S. Quantum Dot Nanoscale Heterostructures for Solar Energy Conversion. *Chem. Soc. Rev.* **2013**, *42*, 2963–2985.

53. Sitt, A.; Hadar, I.; Banin, U. Band-Gap Engineering, Optoelectronic Properties and Applications of Colloidal Heterostructured Semiconductor Nanorods. *Nano Today* **2013**, *8*, 494–513.

54. Hanna, M. C.; Beard, M. C.; Nozik, A. J. Effect of Solar Concentration on the Thermodynamic Power Conversion Efficiency of Quantum-Dot Solar Cells Exhibiting Multiple Exciton Generation. *J. Phys. Chem. Lett.* **2012**, *3*, 2857–2862.

55. Schaller, R. D.; Klimov, V. I. High Efficiency Carrier Multiplication in PbSe Nanocrystals: Implications for Solar Energy Conversion. *Phys. Rev. Lett.* **2004**, *92*, 186601.

56. Nozik, A. J. Multiple Exciton Generation in Semiconductor Quantum Dots. *Chem. Phys. Lett.* **2008**, *457*, 3–11.

**Chapter 3**

1. Beard, M. C.; Luther, J. M.; Nozik, A. J., The promise and challenge of nanostructured solar cells. *Nature nanotechnology* **2014,** *9* (12), 951-954.

2. Green, M. A., Commercial progress and challenges for photovoltaics. *Nature Energy* **2016,** *1*, 15015.

3. Mailoa, J. P.; Lee, M.; Peters, I. M.; Buonassisi, T.; Panchula, A.; Weiss, D. N., Energy-yield prediction for II–VI-based thin-film tandem solar cells. *Energy & Environmental Science* **2016,** *9* (8), 2644-2653.

4. Semonin, O. E.; Luther, J. M.; Beard, M. C., Quantum dots for next-generation photovoltaics. *Materials Today* **2012,** *15* (11), 508-515.

5. Kurtz, S. R.; Faine, P.; Olson, J., Modeling of two‐junction, series‐connected tandem solar cells using top‐cell thickness as an adjustable parameter. *Journal of Applied Physics* **1990,** *68* (4), 1890-1895.

6. Burst, J. M.; Duenow, J. N.; Albin, D. S.; Colegrove, E.; Reese, M. O.; Aguiar, J. A.; Jiang, C.-S.; Patel, M.; Al-Jassim, M. M.; Kuciauskas, D., CdTe solar cells with open-circuit voltage breaking the 1 V barrier. *Nature Energy* **2016,** *1*, 16015.

7. Rau, U., Reciprocity relation between photovoltaic quantum efficiency and electroluminescent emission of solar cells. *Physical Review B* **2007,** *76* (8), 085303.

8. Green, M. A., Radiative efficiency of state-of-the-art photovoltaic cells. *Progress in Photovoltaics: Research and Applications* **2012,** *20* (4), 472-476.

9. Buffat, P.; Borel, J. P., Size effect on the melting temperature of gold particles. *Physical Review A* **1976,** *13* (6), 2287-2298.

10. Panthani, M. G.; Kurley, J. M.; Crisp, R. W.; Dietz, T. C.; Ezzyat, T.; Luther, J. M.; Talapin, D. V., High Efficiency Solution Processed Sintered CdTe Nanocrystal Solar Cells: The Role of Interfaces. *Nano Letters* **2014,** *14* (2), 670-675.

11. Jasieniak, J.; MacDonald, B. I.; Watkins, S. E.; Mulvaney, P., Solution-Processed Sintered Nanocrystal Solar Cells via Layer-by-Layer Assembly. *Nano Letters* **2011,** *11* (7), 2856-2864.

12. Gur, I.; Fromer, N. A.; Geier, M. L.; Alivisatos, A. P., Air-Stable All-Inorganic Nanocrystal Solar Cells Processed from Solution. *Science* **2005,** *310* (5747), 462-465.

13. Xue, H.; Wu, R.; Xie, Y.; Tan, Q.; Qin, D.; Wu, H.; Huang, W., Recent Progress on Solution-Processed CdTe Nanocrystals Solar Cells. *Applied Sciences* **2016,** *6* (7), 197.

14. Crisp, R. W.; Panthani, M. G.; Rance, W. L.; Duenow, J. N.; Parilla, P. A.; Callahan, R.; Dabney, M. S.; Berry, J. J.; Talapin, D. V.; Luther, J. M., Nanocrystal Grain Growth and Device Architectures for High-Efficiency CdTe Ink-Based Photovoltaics. *ACS Nano* **2014,** *8* (9), 9063-9072.

15. Zhang, H.; Kurley, J. M.; Russell, J. C.; Jang, J.; Talapin, D. V., Solution-Processed, Ultrathin Solar Cells from CdCl3--capped CdTe Nanocrystals: The Multiple Roles of CdCl3-Ligands. *Journal of the American Chemical Society* **2016**.

16. Böhm, M. L.; Jellicoe, T. C.; Tabachnyk, M.; Davis, N. J. L. K.; Wisnivesky-Rocca-Rivarola, F.; Ducati, C.; Ehrler, B.; Bakulin, A. A.; Greenham, N. C., Lead Telluride Quantum Dot Solar Cells Displaying External Quantum Efficiencies Exceeding 120%. *Nano Letters* **2015,** *15* (12), 7987-7993.

17. Davis, N. J. L. K.; Böhm, M. L.; Tabachnyk, M.; Wisnivesky-Rocca-Rivarola, F.; Jellicoe, T. C.; Ducati, C.; Ehrler, B.; Greenham, N. C., Multiple-exciton generation in lead selenide nanorod solar cells with external quantum efficiencies exceeding 120%. *Nature Communications* **2015,** *6*, 8259.

18. Semonin, O. E.; Luther, J. M.; Choi, S.; Chen, H.-Y.; Gao, J.; Nozik, A. J.; Beard, M. C., Peak External Photocurrent Quantum Efficiency Exceeding 100% via MEG in a Quantum Dot Solar Cell. *Science* **2011,** *334* (6062), 1530-1533.

19. Hanna, M.; Nozik, A., Solar conversion efficiency of photovoltaic and photoelectrolysis cells with carrier multiplication absorbers. *Journal of Applied Physics* **2006,** *100* (7), 074510.

20. Liu, M.; de Arquer, F. P. G.; Li, Y.; Lan, X.; Kim, G.-H.; Voznyy, O.; Jagadamma, L. K.; Abbas, A. S.; Hoogland, S.; Lu, Z.; Kim, J. Y.; Amassian, A.; Sargent, E. H., Double-Sided Junctions Enable High-Performance Colloidal-Quantum-Dot Photovoltaics. *Advanced Materials* **2016,** *28* (21), 4142-4148.

21. Choi, J. J.; Wenger, W. N.; Hoffman, R. S.; Lim, Y.-F.; Luria, J.; Jasieniak, J.; Marohn, J. A.; Hanrath, T., Solution-Processed Nanocrystal Quantum Dot Tandem Solar Cells. *Advanced Materials* **2011,** *23* (28), 3144-3148.

22. Wang, X.; Koleilat, G. I.; Tang, J.; Liu, H.; Kramer, I. J.; Debnath, R.; Brzozowski, L.; Barkhouse, D. A. R.; Levina, L.; Hoogland, S.; Sargent, E. H., Tandem colloidal quantum dot solar cells employing a graded recombination layer. *Nature Photonics* **2011,** *5* (8), 480-484.

23. Kim, T.; Gao, Y.; Hu, H.; Yan, B.; Ning, Z.; Jagadamma, L. K.; Zhao, K.; Kirmani, A. R.; Eid, J.; Adachi, M. M.; Sargent, E. H.; Beaujuge, P. M.; Amassian, A., Hybrid tandem solar cells with depleted-heterojunction quantum dot and polymer bulk heterojunction subcells. *Nano Energy* **2015,** *17*, 196-205.

24. Panthani, M. G.; Kurley, J. M.; Crisp, R. W.; Dietz, T. C.; Ezzyat, T.; Luther, J. M.; Talapin, D. V., High Efficiency Solution Processed Sintered CdTe Nanocrystal Solar Cells: The Role of Interfaces. *Nano Letters* **2013,** *14* (2), 670-675.

25. Zhang, J.; Gao, J.; Church, C. P.; Miller, E. M.; Luther, J. M.; Klimov, V. I.; Beard, M. C., PbSe Quantum Dot Solar Cells with More than 6% Efficiency Fabricated in Ambient Atmosphere. *Nano Letters* **2014,** *14* (10), 6010-6015.

26. Crisp, R. W.; Kroupa, D. M.; Marshall, A. R.; Miller, E. M.; Zhang, J.; Beard, M. C.; Luther, J. M., Metal Halide Solid-State Surface Treatment for High Efficiency PbS and PbSe QD Solar Cells. *Scientific reports* **2015,** *5*, 9945.

27. Lan, X.; Voznyy, O.; García de Arquer, F. P.; Liu, M.; Xu, J.; Proppe, A. H.; Walters, G.; Fan, F.; Tan, H.; Liu, M.; Yang, Z.; Hoogland, S.; Sargent, E. H., 10.6% Certified Colloidal Quantum Dot Solar Cells via Solvent-Polarity-Engineered Halide Passivation. *Nano Letters* **2016,** *16* (7), 4630-4634.

28. Rance, W. L.; Burst, J. M.; Meysing, D. M.; Wolden, C. A.; Reese, M. O.; Gessert, T. A.; Metzger, W. K.; Garner, S.; Cimo, P.; Barnes, T. M., 14%-efficient flexible CdTe solar cells on ultra-thin glass substrates. *Applied Physics Letters* **2014,** *104* (14), 143903.

29. Li, J.; Diercks, D. R.; Ohno, T. R.; Warren, C. W.; Lonergan, M. C.; Beach, J. D.; Wolden, C. A., Controlled activation of ZnTe:Cu contacted CdTe solar cells using rapid thermal processing. *Solar Energy Materials and Solar Cells* **2015,** *133*, 208-215.

30. Hoye, R. L. Z.; Ehrler, B.; Böhm, M. L.; Muñoz-Rojas, D.; Altamimi, R. M.; Alyamani, A. Y.; Vaynzof, Y.; Sadhanala, A.; Ercolano, G.; Greenham, N. C.; Friend, R. H.; MacManus-Driscoll, J. L.; Musselman, K. P., Improved Open- Circuit Voltage in ZnO–PbSe Quantum Dot Solar Cells by Understanding and Reducing Losses Arising from the ZnO Conduction Band Tail. *Advanced Energy Materials* **2014,** *4* (8).

31. Luther, J. M.; Gao, J.; Lloyd, M. T.; Semonin, O. E.; Beard, M. C.; Nozik, A. J., Stability Assessment on a 3% Bilayer PbS/ZnO Quantum Dot Heterojunction Solar Cell. *Advanced Materials* **2010,** *22* (33), 3704-3707.

32. Leschkies, K. S.; Beatty, T. J.; Kang, M. S.; Norris, D. J.; Aydil, E. S., Solar Cells Based on Junctions between Colloidal PbSe Nanocrystals and Thin ZnO Films. *ACS Nano* **2009,** *3* (11), 3638-3648.

33. Zhang, J.; Chernomordik, B. D.; Crisp, R. W.; Kroupa, D. M.; Luther, J. M.; Miller, E. M.; Gao, J.; Beard, M. C., Preparation of Cd/Pb Chalcogenide Heterostructured Janus Particles via Controllable Cation Exchange. *ACS Nano* **2015,** *9* (7), 7151-63.

34. De Trizio, L.; Manna, L., Forging Colloidal Nanostructures via Cation Exchange Reactions. *Chemical Reviews* **2016**.

**Chapter 4**

**4.5 References**:

1. Nozik, A. J., Quantum dot solar cells. *Physica E: Low-dimensional Systems and Nanostructures* **2002,** *14* (1–2), 115-120.

2. Bockelmann, U.; Bastard, G., Phonon scattering and energy relaxation in two-, one-, and zero-dimensional electron gases. *Physical Review B* **1990,** *42* (14), 8947-8951.

3. Stewart, J. T.; Padilha, L. A.; Bae, W. K.; Koh, W.-K.; Pietryga, J. M.; Klimov, V. I., Carrier Multiplication in Quantum Dots within the Framework of Two Competing Energy Relaxation Mechanisms. *The Journal of Physical Chemistry Letters* **2013,** *4* (12), 2061-2068.

4. Swarnkar, A.; Marshall, A. R.; Sanehira, E. M.; Chernomordik, B. D.; Moore, D. T.; Christians, J. A.; Chakrabarti, T.; Luther, J. M., Quantum dot–induced phase stabilization of α-CsPbI3 perovskite for high-efficiency photovoltaics. *Science* **2016,** *354* (6308), 92.

5. Liu, M.; Voznyy, O.; Sabatini, R.; Garcia de Arquer, F. P.; Munir, R.; Balawi, A. H.; Lan, X.; Fan, F.; Walters, G.; Kirmani, A. R.; Hoogland, S.; Laquai, F.; Amassian, A.; Sargent, E. H., Hybrid organic-inorganic inks flatten the energy landscape in colloidal quantum dot solids. *Nat Mater* **2017,** *16* (2), 258-263.

6. Semonin, O. E.; Luther, J. M.; Choi, S.; Chen, H.-Y.; Gao, J.; Nozik, A. J.; Beard, M. C., Peak External Photocurrent Quantum Efficiency Exceeding 100% via MEG in a Quantum Dot Solar Cell. *Science* **2011,** *334* (6062), 1530-1533.

7. Böhm, M. L.; Jellicoe, T. C.; Tabachnyk, M.; Davis, N. J. L. K.; Wisnivesky-Rocca-Rivarola, F.; Ducati, C.; Ehrler, B.; Bakulin, A. A.; Greenham, N. C., Lead Telluride Quantum Dot Solar Cells Displaying External Quantum Efficiencies Exceeding 120%. *Nano Letters* **2015,** *15* (12), 7987-7993.

8. Gabor, N. M.; Zhong, Z.; Bosnick, K.; Park, J.; McEuen, P. L., Extremely Efficient Multiple Electron-Hole Pair Generation in Carbon Nanotube Photodiodes. *Science* **2009,** *325* (5946), 1367.

9. Sambur, J. B.; Novet, T.; Parkinson, B. A., Multiple Exciton Collection in a Sensitized Photovoltaic System. *Science* **2010,** *330* (6000), 63.

10. Beard, M. C.; Midgett, A. G.; Law, M.; Semonin, O. E.; Ellingson, R. J.; Nozik, A. J., Variations in the Quantum Efficiency of Multiple Exciton Generation for a Series of Chemically Treated PbSe Nanocrystal Films. *Nano Letters* **2009,** *9* (2), 836-845.

11. Luther, J. M.; Beard, M. C.; Song, Q.; Law, M.; Ellingson, R. J.; Nozik, A. J., Multiple Exciton Generation in Films of Electronically Coupled PbSe Quantum Dots. *Nano Letters* **2007,** *7* (6), 1779-1784.

12. Murphy, J. E.; Beard, M. C.; Norman, A. G.; Ahrenkiel, S. P.; Johnson, J. C.; Yu, P.; Mićić, O. I.; Ellingson, R. J.; Nozik, A. J., PbTe Colloidal Nanocrystals: Synthesis, Characterization, and Multiple Exciton Generation. *Journal of the American Chemical Society* **2006,** *128* (10), 3241-3247.

13. Midgett, A. G.; Luther, J. M.; Stewart, J. T.; Smith, D. K.; Padilha, L. A.; Klimov, V. I.; Nozik, A. J.; Beard, M. C., Size and Composition Dependent Multiple Exciton Generation Efficiency in PbS, PbSe, and PbSxSe1–x Alloyed Quantum Dots. *Nano Letters* **2013,** *13* (7), 3078-3085.

14. Midgett, A. G.; Hillhouse, H. W.; Hughes, B. K.; Nozik, A. J.; Beard, M. C., Flowing versus Static Conditions for Measuring Multiple Exciton Generation in PbSe Quantum Dots. *The Journal of Physical Chemistry C* **2010,** *114* (41), 17486-17500.

15. Schaller, R. D.; Klimov, V. I., High Efficiency Carrier Multiplication in PbSe Nanocrystals: Implications for Solar Energy Conversion. *Physical Review Letters* **2004,** *92* (18), 186601.

16. Eshet, H.; Baer, R.; Neuhauser, D.; Rabani, E., Theory of highly efficient multiexciton generation in type-II nanorods. *Nature Communications* **2016,** *7*, 13178.

17. Cirloganu, C. M.; Padilha, L. A.; Lin, Q.; Makarov, N. S.; Velizhanin, K. A.; Luo, H.; Robel, I.; Pietryga, J. M.; Klimov, V. I., Enhanced carrier multiplication in engineered quasi-type-II quantum dots. *Nature Communications* **2014,** *5*, 4148.

18. Zhang, J.; Chernomordik, B. D.; Crisp, R. W.; Kroupa, D. M.; Luther, J. M.; Miller, E. M.; Gao, J.; Beard, M. C., Preparation of Cd/Pb Chalcogenide Heterostructured Janus Particles via Controllable Cation Exchange. *ACS Nano* **2015,** *9* (7), 7151-63.

19. Zhang, J.; Gao, J.; Church, C. P.; Miller, E. M.; Luther, J. M.; Klimov, V. I.; Beard, M. C., PbSe Quantum Dot Solar Cells with More than 6% Efficiency Fabricated in Ambient Atmosphere. *Nano Letters* **2014,** *14* (10), 6010-6015.

20. Chernomordik, B. D.; Marshall, A. R.; Pach, G. F.; Luther, J. M.; Beard, M. C., Quantum Dot Solar Cell Fabrication Protocols. *Chemistry of Materials* **2017,** *29* (1), 189-198.

21. Utterback, J. K.; Grennell, A. N.; Wilker, M. B.; Pearce, O. M.; Eaves, J. D.; Dukovic, G., Observation of trapped-hole diffusion on the surfaces of CdS nanorods. *Nat Chem* **2016,** *8* (11), 1061-1066.

22. Saunders, A. E.; Ghezelbash, A.; Sood, P.; Korgel, B. A., Synthesis of High Aspect Ratio Quantum-Size CdS Nanorods and Their Surface-Dependent Photoluminescence. *Langmuir* **2008,** *24* (16), 9043-9049.

23. Crisp, R. W.; Kroupa, D. M.; Marshall, A. R.; Miller, E. M.; Zhang, J.; Beard, M. C.; Luther, J. M., Metal Halide Solid-State Surface Treatment for High Efficiency PbS and PbSe QD Solar Cells. *Scientific reports* **2015,** *5*, 9945.

APPENDIX A

**Non-Normalized PbS/CdS Janus Visible PL Spectra**

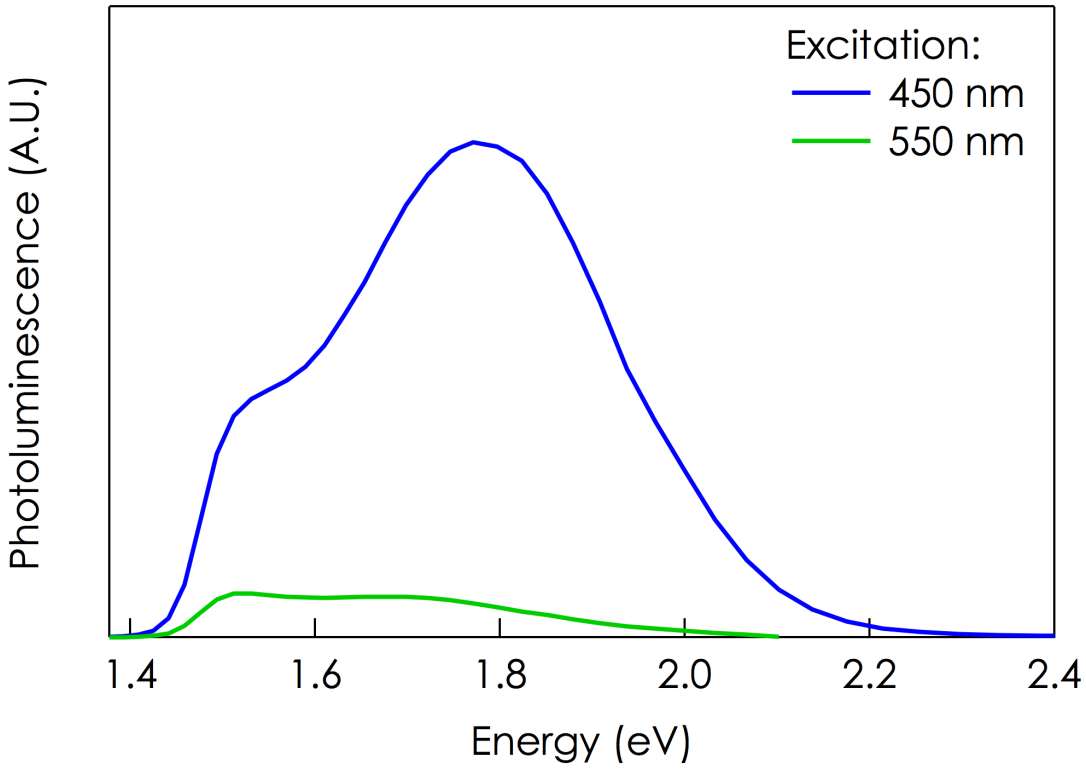


**Figure A.1.** Non-Normalized visible PL spectra of a 50:50 PbS:CdS Janus-like sample excited at 450 nm (above the CdS band gap) and at 550 nm (below the CdS band gap).